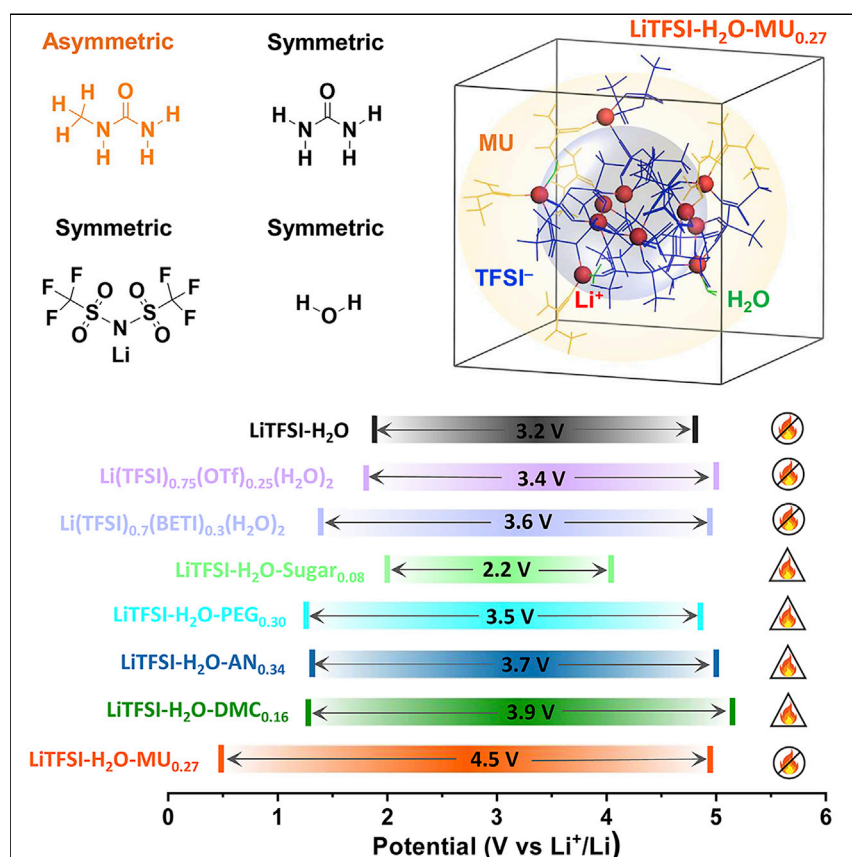


## Article

## Asymmetric donor-acceptor molecule-regulated core-shell-solvation electrolyte for high-voltage aqueous batteries



Asymmetric donor-acceptor molecules such as methylurea can regulate the hydrogen-bonding network of aqueous electrolyte to form a peculiar nanoscale core-shell-like solvation structure, which not only breaks the physical restriction of limited lithium salt solubility in water but also effectively suppresses hydrogen evolution at low potentials toward 0.5 V versus Li<sup>+</sup>/Li. This simple approach truly inherits the high safety of aqueous electrolytes and substantially expands the electrochemical stability window without compromising its cost-effective property.

Rui Lin, Changming Ke, Juner Chen, Shi Liu, Jianhui Wang

liushi@westlake.edu.cn (S.L.)  
wangjianhui@westlake.edu.cn (J.W.)

**Highlights**

Introduce an aqueous electrolyte design using asymmetric donor-acceptor molecule

A new core-shell-solvation aqueous electrolyte with all nonflammable ingredients

A 4.5 V window with *in situ* DEMS identifying HER elimination at 0.5 V versus Li<sup>+</sup>/Li

Stable operations of a NbO<sub>2</sub>|LiMn<sub>2</sub>O<sub>4</sub> full cell (~175 Wh kg<sup>-1</sup>) under a harsh condition

Article

# Asymmetric donor-acceptor molecule-regulated core-shell-solvation electrolyte for high-voltage aqueous batteries

Rui Lin,<sup>1,3,7</sup> Changming Ke,<sup>4,5,7</sup> Juner Chen,<sup>1,2</sup> Shi Liu,<sup>4,5,6,\*</sup> and Jianhui Wang<sup>1,2,3,8,\*</sup>

## SUMMARY

Salt-concentrated aqueous electrolytes show a wider electrochemical window than conventional aqueous electrolytes, yet still suffer from significant hydrogen evolution reaction (HER) at <1.9 V versus Li<sup>+</sup>/Li. Introducing organic compounds was reported to alleviate HER, but all reported organic additives are flammable, inevitably compromising the safety property. Here, we report a new all-nonflammable-ingredient aqueous electrolyte via hybridizing with nonflammable methylurea. The structurally asymmetric methylurea molecules possessing both donor and acceptor functional groups regulate the hydrogen bonding network, resulting in peculiar nano-scale core-shell-like clusters. Such unique solution structure allows localized super-high salt concentration in the electrolyte and suppresses HER at 0.5 V versus Li<sup>+</sup>/Li, achieving a 4.5 V electrochemical window. Under a harsh testing condition with low electrolyte loading, no excess Li resource, no electrode precoating, and conventional aluminum current collectors, this electrolyte realizes a stable cycling of a rocking-chair NbO<sub>2</sub>|LiMn<sub>2</sub>O<sub>4</sub> full cell (~175 Wh kg<sup>-1</sup>) without compromising the safety property.

## INTRODUCTION

Aqueous batteries attract extensive interests because of their striking advantages of high safety, eco-environmental friendliness, facile manufacturing, and high power. However, owing to a narrow electrochemical stability window of water (1.23 V), aqueous batteries generally suffer from a low output voltage (<1.5 V), which excludes the usage of various high-capacity anodes and cathodes that are adopted in commercial nonaqueous batteries. Accordingly, aqueous batteries have an energy density considerably lower than nonaqueous batteries, which severely limits their practical applications.<sup>1–6</sup>

Recently, great progresses have been achieved by applying a salt-concentrated strategy, which breaks the voltage limitation of aqueous electrolyte and potentially leads to a new-generation aqueous battery with an energy density comparable to nonaqueous Li-ion batteries. For the first time, Suo et al. formulated a water-in-salt electrolyte of 21 mol kg<sup>-1</sup> LiTFSI/H<sub>2</sub>O (molar ratio 1:2.6) and realized a 2.3 V Mo<sub>6</sub>S<sub>8</sub>|LiMn<sub>2</sub>O<sub>4</sub> aqueous full cell, benefiting from a low content of free-state water (~15%) in the concentrated electrolyte and the formation of a LiF solid electrolyte interphase (SEI) on the anode that is derived from the lithium bis(trifluoromethane sulfonyl) imide (LiTFSI) salt.<sup>7,8</sup> Subsequently, remarkable improvements were obtained by adopting dual-salt concentrated electrolytes and precoated anodes.<sup>9–15</sup> The former further reduced the content of free water in the electrolyte by increasing

## Context & scale

Aqueous electrolytes are nonflammable and moisture insensitive, which are ideal properties for the development of safe and cheap batteries but are impeded by the narrow electrochemical stability window of water (1.23 V). Despite intensive efforts, aqueous electrolytes remain incompatible with one of the most used anodes, Li<sub>4</sub>Ti<sub>5</sub>O<sub>12</sub> (potential plateau 1.55 V versus Li<sup>+</sup>/Li), under a practical testing condition owing to the cathodic challenge of parasitic HER at <1.9 V versus Li<sup>+</sup>/Li. Here, we report a new class of aqueous electrolyte with a peculiar core-shell-like solvation structure by hybridizing asymmetric donor-acceptor molecules, which effectively eliminates HER even at 0.5 V versus Li<sup>+</sup>/Li and enables a stable operation of NbO<sub>2</sub> anode (a 70% increase of energy density as compared to Li<sub>4</sub>Ti<sub>5</sub>O<sub>12</sub>). This work offers a simple and effective way of manipulating the solvation structure and interphase chemistry for high-voltage aqueous electrolytes without compromising the safety property.

the salt solubility and realized a 3 V  $\text{Li}_4\text{Ti}_5\text{O}_{12}(\text{LTO})|\text{LiNi}_{0.5}\text{Mn}_{1.5}\text{O}_4$  battery;<sup>10</sup> the latter alleviated the hydrogen evolution on the precoated graphite or lithium metal electrodes and enabled a charge-discharge operation of 4 V for cycles.<sup>13,14</sup> However, the usage of a high content of salts (including ionic liquids) will increase the cost of electrolyte, which brings significant hindrances for their practical applications, while precoating an anode that works beyond the electrochemical stability window of electrolyte cannot guarantee a long-term stability because the pretreated surface, once damaged, cannot repair by itself. Nevertheless, even when combining these two approaches, parasitic hydrogen evolution reactions on the anode still exist especially for a charge-discharge operation under low potentials of <1.9 V versus  $\text{Li}^+/\text{Li}$ .<sup>13–15</sup> Thus, a more efficient solution is urgently required, which should be from the improvement of the electrolyte itself.

To circumvent this cathodic challenge above, most recent studies turned to hybridizing the concentrated aqueous electrolytes with various organic materials, such as polyethylene oxide (PEO),<sup>15</sup> dimethyl carbonate (DMC),<sup>16</sup> acetonitrile (AN),<sup>17–19</sup> propylene carbonate,<sup>20</sup> methylsulfonylmethane (MSM),<sup>21</sup> tetraethylene glycol dimethyl ether (TEGDME),<sup>22</sup> dimethyl sulfoxide (DMSO),<sup>23,24</sup> sugar,<sup>25</sup> and poly(ethylene glycol) (PEG).<sup>26</sup> Among them, DMC, AN, MSM, and TEGDME were reported to strengthen the SEI on the anode via altering the electrolyte-electrode interfacial reaction, while PEO, DMSO, sugar, and PEG were reported to reduce the content of free-state water via regulating the hydrogen-bonding structure of electrolyte. Despite the expanded electrochemical window, these reported hybrid aqueous/nonaqueous electrolytes contain organic solvents that are flammable, thus compromising the safety of aqueous electrolytes. It is noteworthy that the property of nonflammability of the electrolyte depends on both self-extinguishing time (SET) and flash point.<sup>27,28</sup> A simple mixture of flammable and nonflammable ingredients cannot guarantee safety even if this blending has zero SET because these components will separate at high temperatures due to their different volatility (see discussions below).

By applying multiple strategies mentioned above, aqueous batteries with output voltage of >2 V have been demonstrated in charge-discharge operations for hundreds of cycles, but they are generally under some prerequisite, such as sophisticated precoating of anode, excessive lithium resource with a surfeit of cathode, flood electrolyte, and specific current collector (Ti or stainless steel) (see [Table S1](#)).<sup>7–26</sup> Hence, it remains a challenge to expand the electrochemical window of aqueous electrolyte without compromising its safety and cost merits.

In this work, we report a simple yet effective approach to a wide-electrochemical-window aqueous electrolytes by hybridizing with nonflammable asymmetric donor-acceptor molecules (see [Figure 1](#)). Methylurea (MU) was selected mainly based on three aspects: (1) MU is a nonflammable, cheap, and low-toxic substance, the introduction of which can inherit the characters of low cost, environmental friendliness, and high safety of the aqueous electrolyte to a maximum degree. (2) MU has functional groups that can serve as both donors and acceptors of hydrogen bonds (see [Figure 2A](#)): the carbonyl donor group can coordinate to  $\text{Li}^+$  cation and/or water while the amide acceptor group may also interact with  $\text{TFSI}^-$  anion and/or water, by which, the solution structure of the electrolyte as well as the electrolyte-electrode interphase chemistry can be regulated. (3) MU has an asymmetric molecular structure, which may further enhance the solubility of  $\text{LiTFSI}$  salt in the electrolyte but without increasing the cost due to its considerably lower price than some asymmetric salts used to increase the  $\text{Li}/\text{H}_2\text{O}$  molar ratio.<sup>12,29,30</sup> By simply mixing MU,  $\text{LiTFSI}$ ,

<sup>1</sup>Key Laboratory of 3D Micro/Nano Fabrication and Characterization of Zhejiang Province, School of Engineering, Westlake University, Hangzhou 310024, China

<sup>2</sup>Institute of Advanced Technology, Westlake Institute for Advanced Study, Hangzhou 310024, China

<sup>3</sup>School of Materials Science & Engineering, Zhejiang University, Hangzhou 310024, China

<sup>4</sup>School of Science, Westlake University, Hangzhou 310024, China

<sup>5</sup>Institute of Natural Sciences, Westlake Institute for Advanced Study, Hangzhou 310024, China

<sup>6</sup>Key Laboratory for Quantum Materials of Zhejiang Province, Hangzhou 310024, China

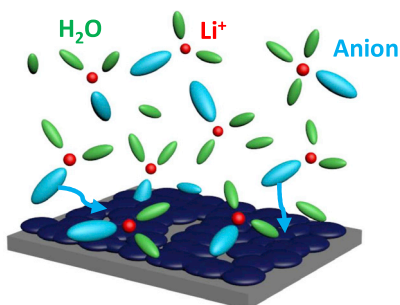
<sup>7</sup>These authors contributed equally

<sup>8</sup>Lead contact

\*Correspondence: [liushi@westlake.edu.cn](mailto:liushi@westlake.edu.cn) (S.L.), [wangjianhui@westlake.edu.cn](mailto:wangjianhui@westlake.edu.cn) (J.W.)

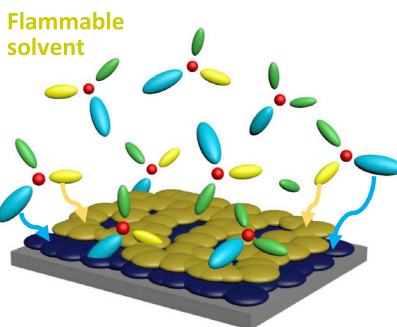
<https://doi.org/10.1016/j.joule.2022.01.002>

- Limited voltage window
- High cost
- High safety



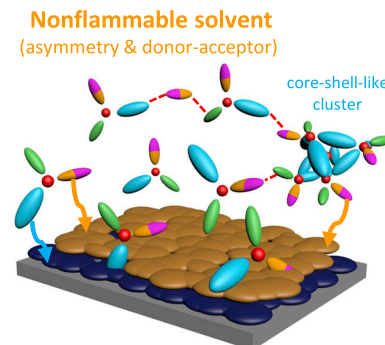
Salt-concentrated aqueous electrolyte 


- Expanded voltage window
- Reduced cost
- Compromised safety



Organic/aqueous hybrid electrolyte 

- Further expanded window
- Reduced cost
- High safety



Nonflammable asymmetric donor-acceptor molecule regulated electrolyte 

**Figure 1. Electrolyte design for safe and high-voltage aqueous battery**

Salt-concentrated aqueous electrolyte shows an improved electrochemical stability window as compared to conventional dilute electrolyte owing to the decrease of free-state water as well as the formation of salt-derived inorganic SEI in the former. However, attempts to further improve the electrochemical window face difficulties of limited solubility of salt in the water and the dramatic increase of cost. Organic/aqueous hybrid electrolyte contributes to new organic components in the SEI and obtains a further wider electrochemical window than salt-concentrated aqueous electrolyte without increasing the cost; however, the introduced flammable organic solvent compromises the safety property of aqueous electrolyte. We propose to develop new all-nonflammable-ingredient hybrid aqueous electrolyte by introducing nonflammable asymmetric donor-acceptor organic solvent. Not only does it truly inherit high safety of aqueous electrolyte but also remarkably widens the electrochemical window by regulating the electrolyte's hydrogen bonding structure and the electrolyte/electrode interphase chemistry.

and H<sub>2</sub>O together, we formulated an all-nonflammable-ingredient organic/aqueous hybrid electrolyte with a peculiar core-shell-like solvation structure that shows a 4.5 V electrochemical stable window. Using this novel electrolyte, a stable charge-discharge cycling of a high-energy-density rocking-chair NbO<sub>2</sub>|LiMn<sub>2</sub>O<sub>4</sub> full cell at both low and high rates were achieved under a harsh testing condition with low electrolyte loading, no excess Li resource (negative/positive capacity ratio [N/P] ≥ 1), no electrode pre-coating, and conventional Al current collectors for both anode and cathode.

## RESULTS AND DISCUSSION

### Asymmetric donor-acceptor molecule regulated aqueous electrolytes

LiTFSI, H<sub>2</sub>O, and MU can be mixed with each other to form a homogeneous solution, implying the existence of strong interactions among them. Ten saturated solutions composed of these three ingredients were prepared by dissolving the LiTFSI salt into H<sub>2</sub>O/MU mixtures of various molar ratios. The as-prepared samples are named as Li-H<sub>2</sub>O-MU<sub>x</sub> for short, in which x corresponds to the mole fraction of MU in the solution, and the sample compositions are listed in the Table S2. As shown in Figures 2A–2C, for the sample of Li-H<sub>2</sub>O-MU<sub>0.00</sub>, i.e., the LiTFSI/H<sub>2</sub>O saturated solution without MU (Li:H<sub>2</sub>O:MU molar ratio 38:100:0), its mole fraction of LiTFSI ( $M_{\text{LiTFSI}}$ ) is 0.28. Introducing asymmetric MU can significantly increase the solubility of LiTFSI in the solution. At  $M_{\text{MU}} = 0.27$ ,  $M_{\text{LiTFSI}}$  increases by 43% and reaches 0.41 (Li:H<sub>2</sub>O:MU molar ratio 70:54:46), which is the highest molar fraction of LiTFSI for single-salt (LiTFSI) aqueous solutions reported so far. By contrast, introducing symmetric molecule of urea (U) cannot increase the solubility of LiTFSI. In a H<sub>2</sub>O/U (54: 46) mixture,

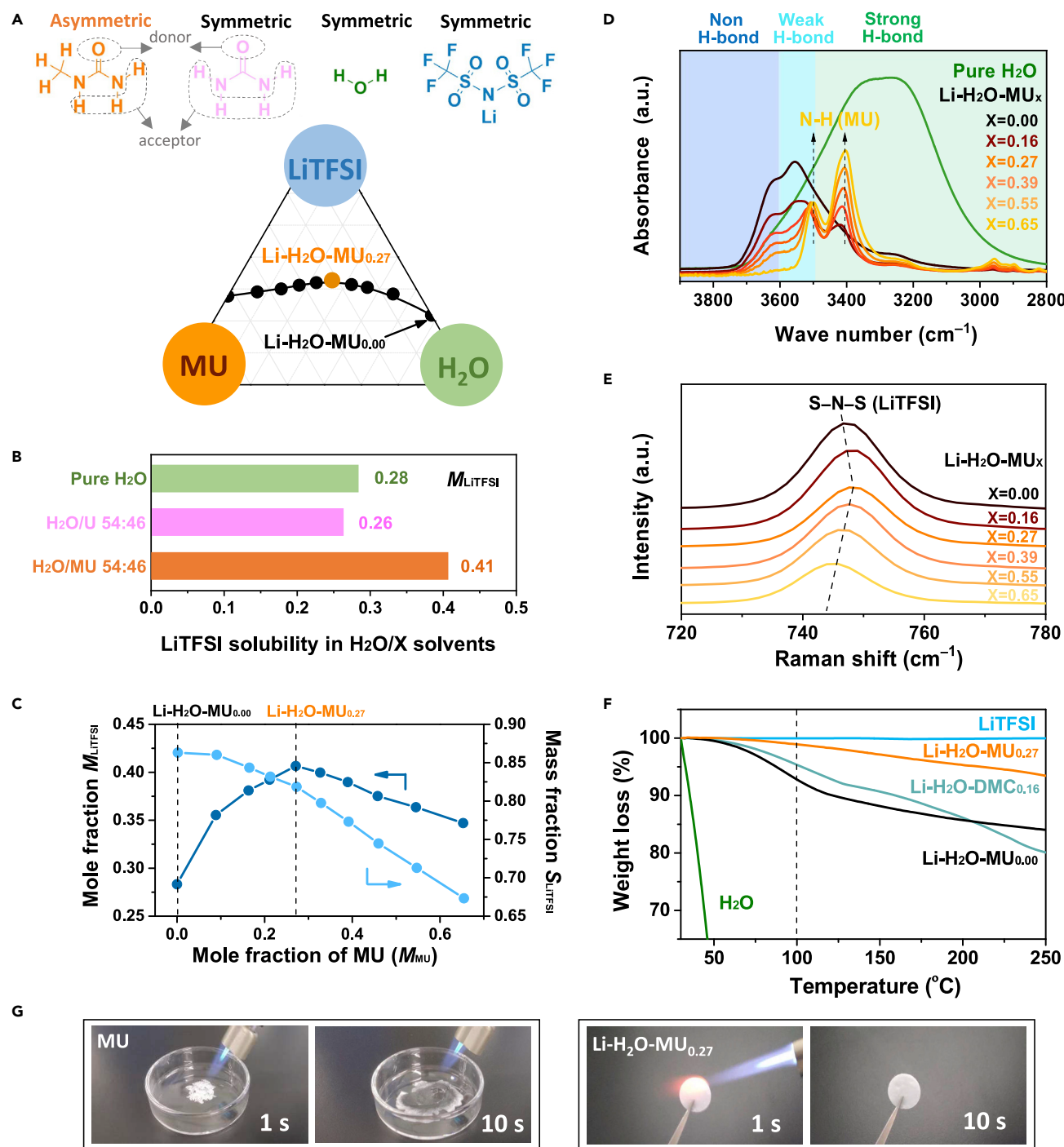


**Figure 2. Preparation and characterizations of LiTFSI(Li)-H<sub>2</sub>O-MU solutions**

(A) Ternary diagram of the compositional variation of Li-H<sub>2</sub>O-MU<sub>x</sub>. x corresponds to the mole fraction of MU in the solutions.

(B) Comparison of the LiTFSI solubility in H<sub>2</sub>O, H<sub>2</sub>O/U, and H<sub>2</sub>O/MU solvents.

(C) Mole and mass fractions of LiTFSI dependent of the content of MU in the solutions.

(D and E) FTIR (D) and Raman (E) spectra of Li-H<sub>2</sub>O-MU<sub>x</sub> (x = 0.00~0.65) solutions. For solutions with x > 0.16, IR absorbance corresponding to Strong and Weak H-bond almost disappears, evidencing the introduction of MU effectively decreases the content of free-state water in the solutions.

(F) Weight loss of Li-H<sub>2</sub>O-MU<sub>0.00</sub>, Li-H<sub>2</sub>O-MU<sub>0.27</sub>, and Li-H<sub>2</sub>O-DMC<sub>0.16</sub> solutions in the thermogravimetric tests. Pristine LiTFSI salt and water are used for comparison.

(G) Flame tests of pristine MU and Li-H<sub>2</sub>O-MU<sub>0.27</sub> solution.

**Table 1. Physicochemical properties of different aqueous electrolytes**

Electrolyte	Conductivity (mS cm <sup>-1</sup> )	Viscosity (mPa s)	Flash point (°C)	Self-extinguish time (s g <sup>-1</sup> )	Weight loss at 100°C (wt %)
Li-H <sub>2</sub> O-MU <sub>0.00</sub>	7.8	65	n/a	0	-7.2
Li-H <sub>2</sub> O-MU <sub>0.27</sub>	3.2	646	n/a	0	-1.1
Li-H <sub>2</sub> O-DMC <sub>0.16</sub>	2.0	148	103.1 ± 1	0	-4.6
Li-H <sub>2</sub> O-AN <sub>0.34</sub>	3.3	103	73.4 ± 1	0	-5.8
Li-H <sub>2</sub> O-PEG <sub>0.30</sub>	0.8	644	n/a	42 ± 2	-1.9

$M_{\text{LiTFSI}}$  only reaches 0.26 at maximum, which is even lower than that of the LiTFSI/H<sub>2</sub>O saturated solution (Figure 2B). Interestingly, the substantial increase of  $M_{\text{LiTFSI}}$  (0.28 → 0.41) in the Li-H<sub>2</sub>O-MU solution does not lead to an increase of mass fraction ( $S_{\text{LiTFSI}}$ ) or molar concentration of LiTFSI in the solution; instead, it leads to a decrease of  $S_{\text{LiTFSI}}$  from 0.86 to 0.82, as well as of the molar concentration from 5.16 to 4.69 mol L<sup>-1</sup> (see Figure 2C and Table S2), and thus contributes to a reduction of the electrolyte cost, distinct from the conventional salt-concentrated approach.

A high-performance concentrated aqueous electrolyte usually has a low content of free-state water molecules and a high content of TFSI<sup>-</sup> aggregates based on previous studies.<sup>7-26</sup> For pure water, the O-H stretching can be divided into three categories based on the strength of O-H bonds:<sup>31,32</sup> Strong H-bond (3,000–3,500 cm<sup>-1</sup>) corresponding to the weakest O-H stretching that binds strong hydrogen bonds, Weak H-bond (3,500–3,600 cm<sup>-1</sup>) corresponding to the moderate O-H stretching that binds weak hydrogen bonds, and Non H-bond (3,600–3,700 cm<sup>-1</sup>) corresponding to the strongest O-H stretching that binds no hydrogen bonds; among them, the Strong H-bond presents the predominant part (93%). As shown in Figures 2D and S1, the infrared absorbance corresponding to Strong H-bond almost disappears and that to Non H-bond becomes dominant (>75%) for the Li-H<sub>2</sub>O-MU<sub>x</sub> samples at  $x > 0.27$ , evidencing that the introduction of MU effectively decreases the content of free-state water in the solutions. On the other hand, Raman spectra showed that the Li-H<sub>2</sub>O-MU<sub>0.27</sub> sample has a highest S–N–S bending vibration frequency of TFSI<sup>-</sup> anion (748.4 cm<sup>-1</sup>; Figure 2E), which is almost identical to that of pristine LiTFSI powder sample (see Figure S2), indicating it contains the highest content of TFSI<sup>-</sup> aggregates that strongly coordinate to Li<sup>+</sup> among all the as-prepared MU-assisted solutions.<sup>7,33,34</sup> Clearly, the introduction of MU<sub>0.00</sub>→<sub>0.27</sub> can effectively enhance the TFSI<sup>-</sup>–Li<sup>+</sup> interaction and increase the content of TFSI<sup>-</sup> aggregates while reducing the content of free-state water molecules. However, introducing too much MU<sub>0.27</sub>→<sub>0.65</sub> will weaken the TFSI<sup>-</sup>–Li<sup>+</sup> interaction and compromise the ionic conductivity as well as the viscosity of the electrolyte (see Figure S3). Therefore, the sample of Li-H<sub>2</sub>O-MU<sub>0.27</sub> was selected for a detailed study in comparison to the MU-free sample of Li-H<sub>2</sub>O-MU<sub>0.00</sub>. Shown in Table 1, the Li-H<sub>2</sub>O-MU<sub>0.27</sub> sample has a good ionic conductivity of 3.2 mS cm<sup>-1</sup> at 25°C, which is superior to most reported nonaqueous/aqueous hybrid electrolytes.

Volatility and flammability are two important properties of electrolytes that profoundly affect battery safety. Shown in Figures 2F and S4, the Li-H<sub>2</sub>O-MU<sub>0.27</sub> sample (containing 4.1 wt% water) has a weight loss of 1.1 wt% at 100°C, corresponding to the evaporation of 27% of water. Even at 250°C, its weight loss is less than 7 wt%, demonstrating an outstanding thermal stability exceeding the MU-free Li-H<sub>2</sub>O-MU<sub>0.00</sub> sample and other aqueous solutions hybridized with volatile organic compounds. Taking the Li-H<sub>2</sub>O-DMC<sub>0.16</sub> sample (containing 7.0 wt% H<sub>2</sub>O and 12.0 wt% DMC) as an example, it gives a weight loss of 4.6 wt% at 100°C, which is equivalent to the evaporation of 66% of water or 38% of DMC. Because DMC has a lower boiling

point than H<sub>2</sub>O, this weight loss should be mainly from DMC evaporation. We measured the flash point of Li–H<sub>2</sub>O–DMC<sub>0.16</sub> and found its vapor ignites at 103°C (see Table 1), confirming the above assumption. For the Li–H<sub>2</sub>O–AN<sub>0.34</sub> sample, its flash point is even lower (73°C), which is ascribed to the higher volatility of AN as compared to DMC. In the case of the Li–H<sub>2</sub>O–PEG<sub>0.30</sub> sample, whose organic ingredient (PEG) is non-volatile, we did not detect its flash point, but we found that it actually supports combustion with a SET of 42 s g<sup>-1</sup> in a propane-oxygen flame ignition test (see Table 1, Figure S5, and Video S1). This can be easily understood: at high temperature, water will evaporate out quickly and the remaining materials with a high content (60 wt%) of PEG become flammable. In sharp contrast, owing to the nonflammability of MU itself, the Li–H<sub>2</sub>O–MU<sub>0.27</sub> sample shows zero SET and no flash point (see Table 1, Figure 2G, and Video S2), firmly confirming that this MU-assisted all-nonflammable-ingredient electrolyte indeed inherits the nonflammability of aqueous electrolytes. Hence, to ensure nonflammability of a nonaqueous/aqueous hybrid electrolyte, the introduced nonaqueous materials must be nonflammable.

### Safe and high-voltage aqueous Li-ion batteries

The electrochemical stability window of the as-prepared Li–H<sub>2</sub>O–MU electrolytes was evaluated by linear sweep voltammetry (LSV). Here, we performed this measurement on a carbon-coated Al foil instead of bare Ti or Al foil because it represents a harsher and more realistic environment: (1) Al current collector is indispensable in a commercial Li-ion battery owing to its low price, light weight, and easy processing despite its capability of suppressing oxygen evolution at high potentials being not as good as that of Ti; (2) conductive carbon, widely used in both anode and cathode fabrications, can produce a considerably larger current signal as compared to a bare current collector due to its much larger surface area (see Figure S6).<sup>26,35</sup> Moreover, differential electrochemical mass spectrometry (DEMS) was applied to detect H<sub>2</sub> and O<sub>2</sub> products caused by water decomposition during the LSV test. As shown in Figures 3A, S7, and S8, the introduction of MU in the LiTFSI/H<sub>2</sub>O electrolyte dramatically brings down the onset potential of cathodic leakage current from 1.8 to 0.5 V versus Li<sup>+</sup>/Li, consistent with H<sub>2</sub> evolution profiles obtained from the DEMS measurement. Moreover, a strict potentiostatic test under 0.5 V versus Li<sup>+</sup>/Li also showed that the reduction current in the Li–H<sub>2</sub>O–MU<sub>0.27</sub> electrolyte can be quickly decreased close to zero (see Figure S9). All the above firmly evidence that the water decomposition is effectively suppressed in the MU-assisted electrolyte at such a low potential. For a direct comparison with previously reported aqueous electrolytes in the literature, we carried out LSV measurements in these electrolytes under the same conditions. Clearly, the MU-assisted electrolyte even shows a considerably lower cathodic limit than that of state-of-the-art aqueous electrolyte, leading to a widest electrochemical window of 4.5 V among various reported aqueous electrolytes adopting salt-concentrated and organic-hybridized strategies (see Figures 3B and 3C). The remarkable expanded cathodic limit in the Li–H<sub>2</sub>O–MU<sub>0.27</sub> electrolyte could be resulting from the formation of SEI during the first cathodic scan (see Figure S7), thus allowing a full Li-intercalation/deintercalation of the LTO electrode (Figure 3A).

To make a full use of the wide electrochemical stability window of the Li–H<sub>2</sub>O–MU<sub>0.27</sub> electrolyte, we tried some high-capacity anodes, such as SnO<sub>2</sub> and Li metal. Unfortunately, reversible charge-discharge reactions of SnO<sub>2</sub> cannot be realized in the aqueous electrolytes (Figure S10). The reason could be associated with the fact that the conversion-type electrode suffers from continuous structural changes coupling with a large volume change, which remains a challenging issue even for a nonaqueous electrolyte. For the Li metal anode, we found that the one with a surface

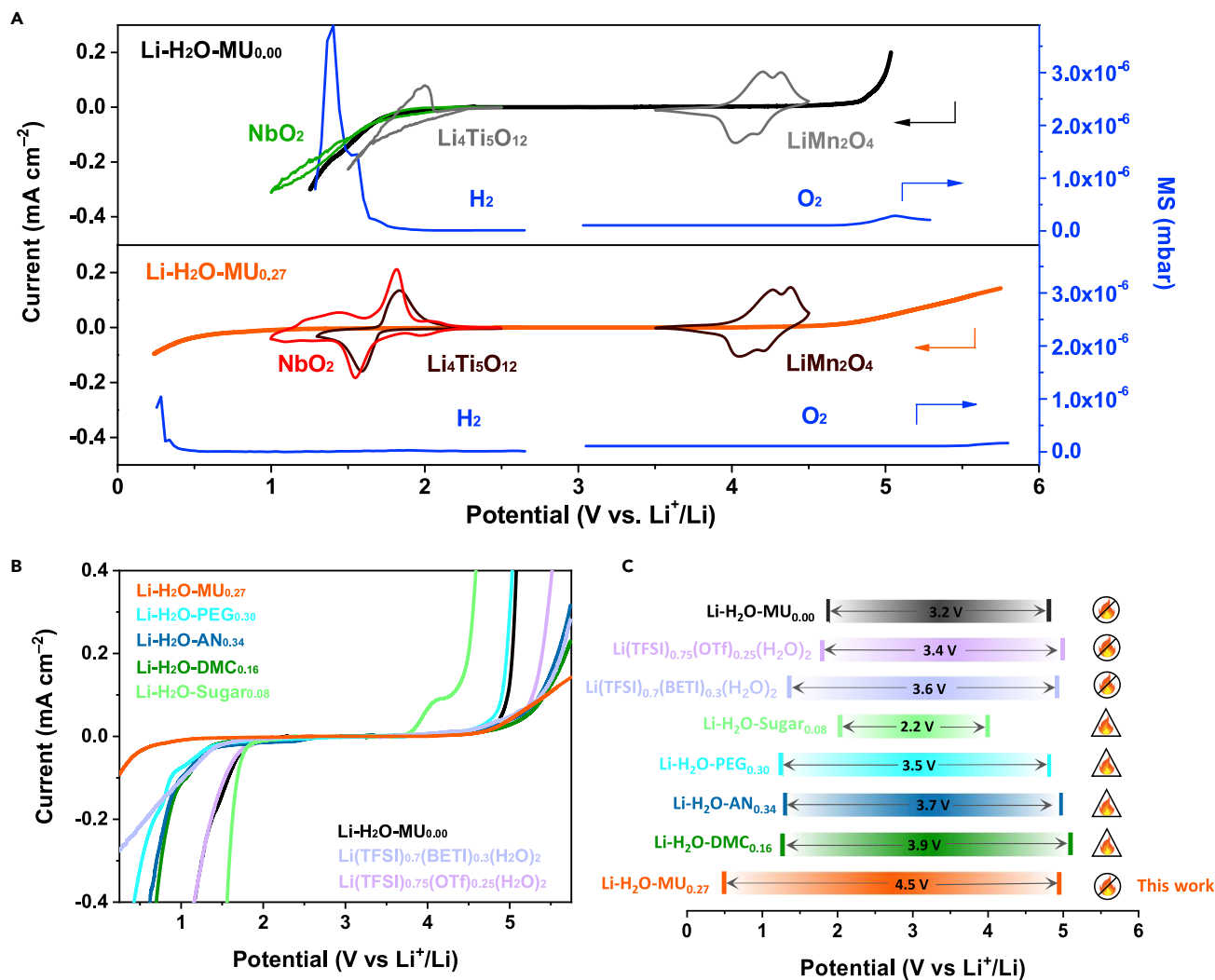


**Figure 3. Electrochemical stability window of as-prepared LiTFSI(Li)-H<sub>2</sub>O-MU solutions**

(A) Electrochemical window of the Li-H<sub>2</sub>O-MU<sub>0.00</sub> and Li-H<sub>2</sub>O-MU<sub>0.27</sub> electrolytes evaluated by LSV tests on carbon-coated Al electrode, together with H<sub>2</sub> and O<sub>2</sub> evolutions monitored by *in situ* DEMS during the cathodic and anodic scans. Clearly, both H<sub>2</sub> and O<sub>2</sub> evolutions are efficiently suppressed in the Li-H<sub>2</sub>O-MU<sub>0.27</sub> electrolyte, particularly, the cathodic limit is dramatically decreased from 1.8 to 0.5 V, versus Li<sup>+</sup>/Li. With the improved electrochemical window, charge-discharge of low-potential and high-capacity NbO<sub>2</sub> electrode can be fully operated in the Li-H<sub>2</sub>O-MU<sub>0.27</sub> electrolyte. (B) LSV curves of various aqueous electrolytes on carbon-coated Al electrode. (C) Comparison of electrochemical window between the Li-H<sub>2</sub>O-MU<sub>0.27</sub> electrolyte and other reported aqueous electrolytes as shown in (B). The LSV scan rate is 5 mV s<sup>-1</sup>, and the onset current density for the electrochemical stable window is set as 0.05 mA cm<sup>-2</sup>. For the Li-H<sub>2</sub>O-MU<sub>0.27</sub> electrolyte, the LSV and *in situ* DEMS measurements were also carried out at a low scan rate of 0.05 mV s<sup>-1</sup> (shown in Figures S7 and S8), by which consistent results were obtained with those at 5 mV s<sup>-1</sup>.

coating can be operated for several cycles, but a long-term cycling stability was not realized either (Figure S11) because Li metal works beyond the electrochemical stability window of the aqueous electrolyte. So far, the majority of reported rechargeable aqueous Li-ion batteries adopt intercalation-type materials as the electrodes. Nb-based intercalation-type materials were recently reported as promising fast-rate and high-capacity anodes for Li-ion batteries.<sup>36,37</sup> We synthesized a NbO<sub>2</sub> material without surface coating following the procedure previously reported.<sup>36</sup> The capacity of the homemade NbO<sub>2</sub> was determined to be ca. 285 mAh g<sup>-1</sup> using a commercial nonaqueous electrolyte (see Figures S12 and S13), in which about half of capacity was from the low-potential region of 1.0~1.5 V versus Li<sup>+</sup>/Li (significantly



lower than the plateau potential of LTO, 1.55 V versus  $\text{Li}^+/\text{Li}$ ). As shown in [Figure 3A](#), the  $\text{Li-H}_2\text{O-MU}_{0.27}$  electrolyte enabled a reversible charge-discharge reaction of this  $\text{NbO}_2$  electrode while the  $\text{Li-H}_2\text{O-MU}_{0.00}$  electrolyte failed. Therefore, we selected the intercalation-type  $\text{NbO}_2$  as the anode to fully exploit the potential of our electrolyte design, by which a 70% increase of energy density in the battery can be obtained as compared to that using a conventional LTO electrode.

Using  $\text{NbO}_2$  as anode and  $\text{LiMn}_2\text{O}_4$  as cathode, we fabricated a  $\text{NbO}_2|\text{LiMn}_2\text{O}_4$  full cell to evaluate the long-term cycling stability of  $\text{Li-H}_2\text{O-MU}$  electrolyte. In this battery, both the cathode and anode used a bare Al foil as the current collector, and no surface pretreatment was applied on either the current collector or the active electrode materials. The N/P is 1.0~1.1 without an excess Li resource. The amount of electrolyte per coin cell is 30 mL corresponding to an electrolyte/capacity (E/C) ratio of 30 mL  $\text{mAh}^{-1}$ . The batteries were assembled in the atmosphere without moisture control. All these procedures above guarantee a facile manufacturing of an aqueous battery using this  $\text{Li-H}_2\text{O-MU}$  electrolyte. Then the batteries were tested at a cutoff voltage of 1.5~3.3 V, in which ~44% capacity of the  $\text{NbO}_2$  anode came from the low potential region of 1.0~1.5 V versus  $\text{Li}^+/\text{Li}$  as can be found from the charge-discharge profile of a three-electrode cell ([Figure S14](#)). As shown in [Figure 4](#), the  $\text{NbO}_2|\text{LiMn}_2\text{O}_4$  full battery using the  $\text{Li-H}_2\text{O-MU}_{0.27}$  electrolyte ran a stable cycling performance at both low and high rates. At 0.35 C, it delivers a reversible capacity of 225  $\text{mAh g}^{-1}$  on basis of the  $\text{NbO}_2$  anode, achieving an energy density of 175  $\text{Wh kg}^{-1}$  on basis of the total weight of positive and negative active materials; the coulombic efficiency is 60.1% in the first cycle and quickly surpasses 98% in three cycles, hinting that a good passivation film likely formed to effectively suppress the water decomposition. In sharp contrast, all the other aqueous electrolytes show very poor initial coulombic efficiencies of <17%. Among them,  $\text{Li-H}_2\text{O-MU}_{0.00}$ ,  $\text{Li-H}_2\text{O-Sugar}_{0.08}$ , and  $\text{Li}(\text{TFSI})_{0.75}(\text{OTf})_{0.25}(\text{H}_2\text{O})_2$  cannot reach the cutoff voltage of 3.3 V in 40 h. In an extreme case, we found that the coin cell using the  $\text{Li-H}_2\text{O-Sugar}_{0.08}$  electrolyte burst during the initial charge process due to the overpressure caused by too much gas generation. Even at higher rate of 0.7 C and 3.5 C, all the batteries using MU-free electrolytes still suffer from very poor initial (<30%) and average (<95%) coulombic efficiencies as well as a fast capacity decay ([Figure 4B-4D](#) and [S15-S21](#)). In addition, we tested batteries with a higher loading of electrolyte (120 mL  $\text{mAh}^{-1}$ ), but they still declined quickly (see [Figure S22](#)). After disassembling the dead cells, we found considerable electrolyte left. This result suggests that the failure of these cells is not due to the lack of electrolyte but rather likely the consumption of limited active lithium resources in the full cells caused by continuous side reactions and/or poor passivation interphases. By contrast, for the battery using the  $\text{Li-H}_2\text{O-MU}_{0.27}$  electrolyte under the harsh testing condition, initial coulombic efficiencies at 0.7 C and 3.5 C are 72% and 93%, respectively, both of which reach above 99% after several charge-discharge cycles; almost no capacity decay was observed during 300 cycles at 0.7 C and 1,500 cycle at 3.5 C ([Figures S23](#) and [S24](#)). Moreover, it also enabled a stable charge-discharge operation at a temperature range from 0°C to 55°C ([Figures S25](#) and [S26](#)). And the  $\text{Li}_4\text{Ti}_5\text{O}_{12}|\text{LiMn}_2\text{O}_4$  battery can be also cycled for over 1,000 times in the  $\text{Li-H}_2\text{O-MU}_{0.27}$  electrolyte with little capacity decay ([Figure S27](#)). Thus, it is evident that our developed MU-assisted aqueous electrolyte enables high-voltage aqueous batteries superior to previously reported aqueous electrolytes. In addition, we tested the  $\text{NbO}_2|\text{LiMn}_2\text{O}_4$  battery in the electrolyte of  $\text{Li-H}_2\text{O-U}_{0.34}$  and found its performances much poorer than those in the electrolyte of  $\text{Li-H}_2\text{O-MU}_{0.27}$  (see [Figures S28](#) and [S29](#)), demonstrating the advantage of asymmetry-structure organic molecule in developing high-performance aqueous electrolytes.

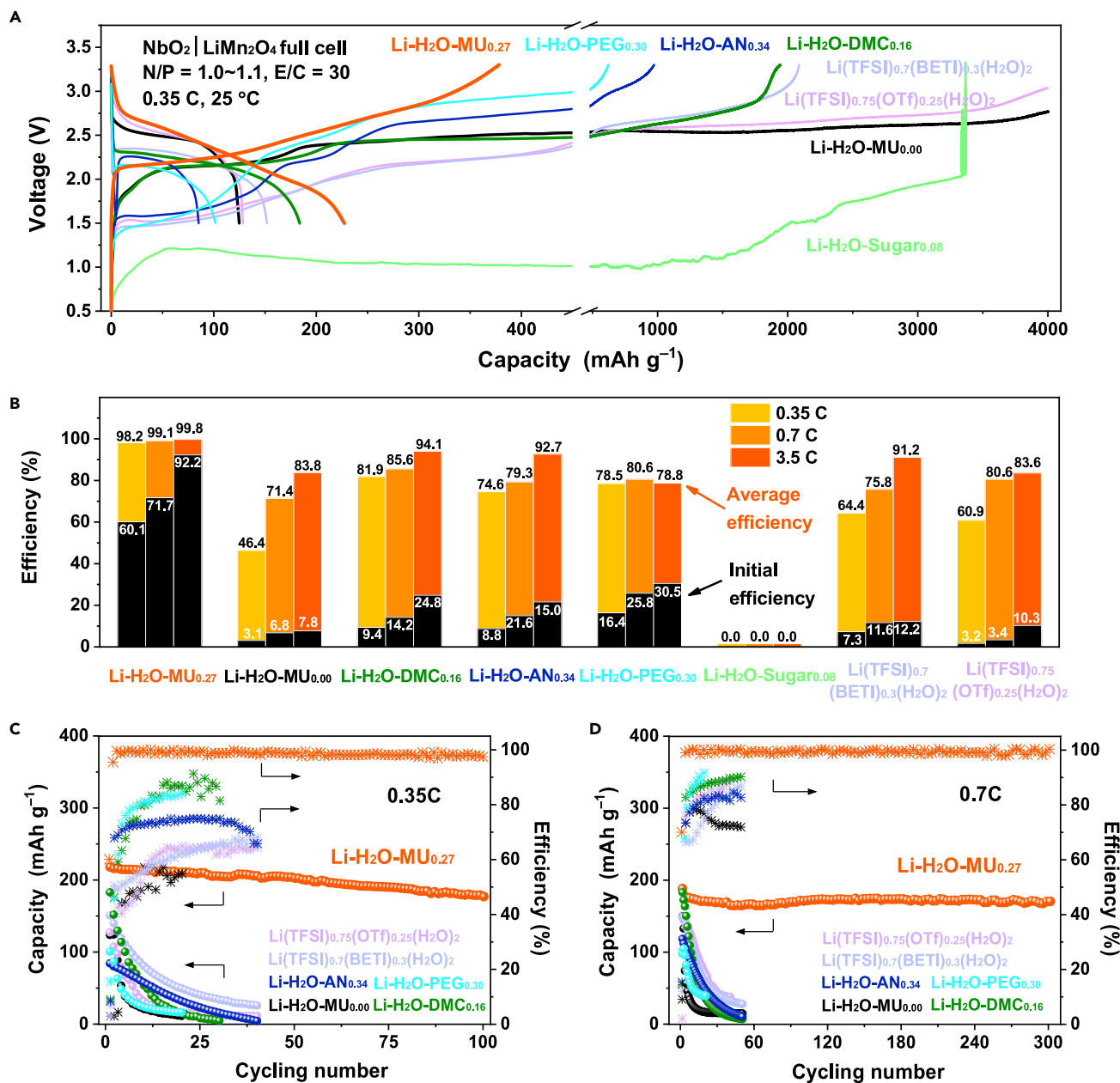


**Figure 4. Electrochemical performance of NbO<sub>2</sub>|LiMn<sub>2</sub>O<sub>4</sub> full cells**

(A and B) Initial charge-discharge voltage curves (A) and initial and average Coulombic efficiencies (B) for the full cells using as-prepared Li-H<sub>2</sub>O-MU<sub>0.27</sub> electrolyte and various reported aqueous electrolytes at different rates.

(C and D) Cycling performance and Coulombic efficiency of the full cells using these above electrolytes at 0.35 C (C) and 0.7 C (D), respectively. All charge-discharge cycling tests were conducted with a cutoff voltage of 1.5~3.3 V at 25 °C. A 1 C rate corresponds to 285 mA g<sup>-1</sup> on the weight basis of the NbO<sub>2</sub> electrode. Al foil was used as the current collector for both anode and cathode. A low electrolyte loading of 30 mL mAh<sup>-1</sup> was used. No surface coating was made on either NbO<sub>2</sub> or LiMn<sub>2</sub>O<sub>4</sub> materials.

### Mechanistic understanding

As demonstrated by our detailed experimental characterizations, the introduction of MU brings multiple benefits for the design of concentrated aqueous electrolytes without compromising its nonflammable property: increase the solubility of LiTFSI salt (Li/H<sub>2</sub>O molar ratio) without increasing the cost, decrease the content of free-state water thus further reducing the volatility, and widen the electrochemical

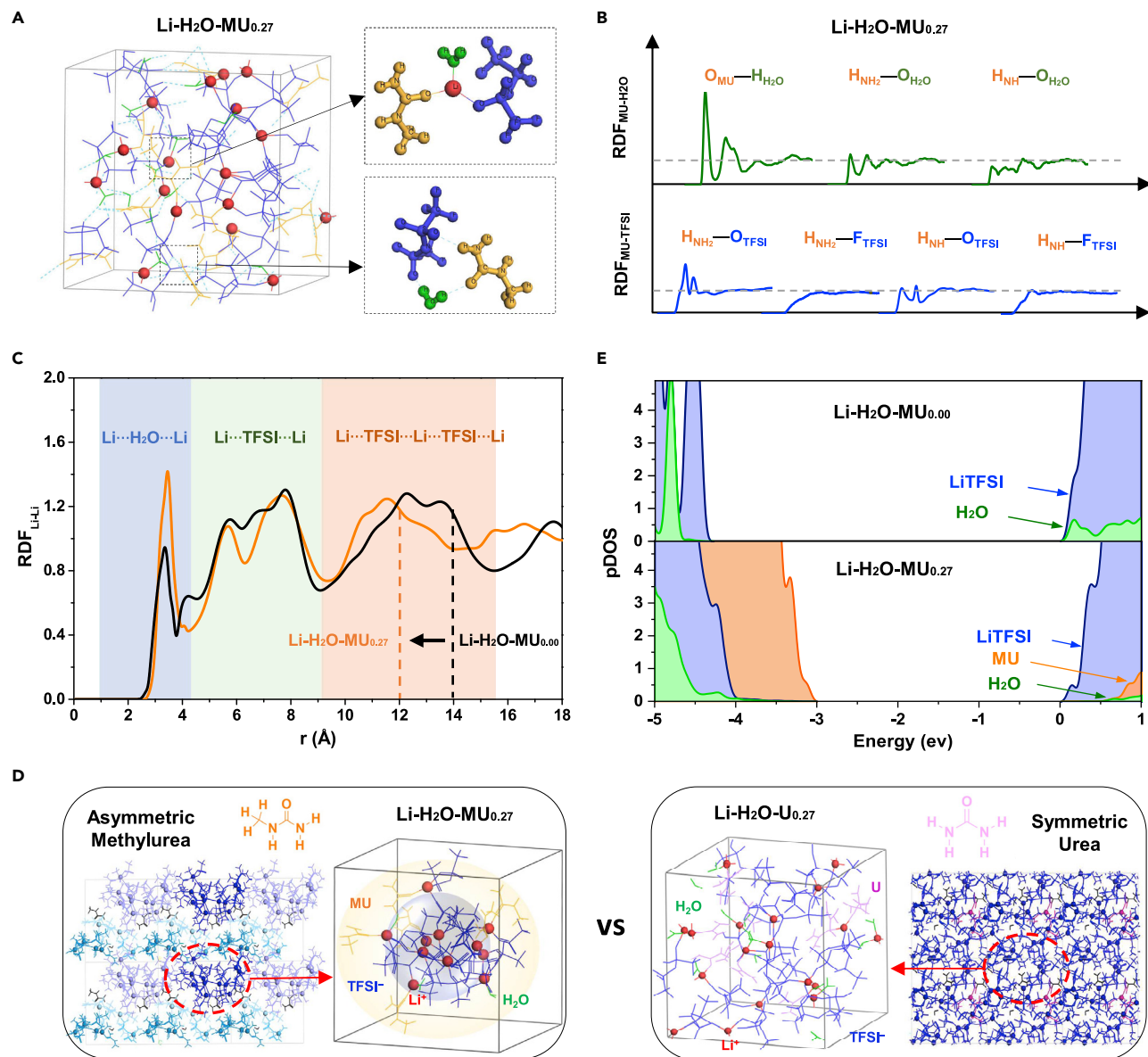


**Figure 5. *Ab initio* MD (AIMD) simulation**

(A) A snapshot of a typical equilibrium trajectory of the  $\text{Li-H}_2\text{O-MU}_{0.27}$  solution. Insets magnify the local coordination among  $\text{Li}^+$  (red),  $\text{TFSI}^-$  (blue),  $\text{H}_2\text{O}$  (green), and MU (orange).

(B) H-O and H-F RDFs of MU- $\text{H}_2\text{O}$  and MU-TFSI in the  $\text{Li-H}_2\text{O-MU}_{0.27}$  solution. MU demonstrates hydrogen bonding with both  $\text{H}_2\text{O}$  and TFSI; the MU- $\text{H}_2\text{O}$  interaction is via  $\text{O}_{\text{MU}}-\text{H}_{\text{H}_2\text{O}}$ , while the MU-TFSI interaction is via  $\text{H}_{\text{NH}_2}-\text{O}_{\text{TFSI}}$ .

(C) Li-Li RDFs of  $\text{Li-H}_2\text{O-MU}_{0.00}$  and  $\text{Li-H}_2\text{O-MU}_{0.27}$ .  $\text{Li-H}_2\text{O-MU}_{0.27}$  has a much shorter “Li-TFSI-Li-TFSI-Li” than  $\text{Li-H}_2\text{O-MU}_{0.00}$ , indicating that the introduction of MU results in a considerably more compact cation-anion structure.

(D) Comparison of solution structures of  $\text{Li-H}_2\text{O-MU}_{0.27}$  and  $\text{Li-H}_2\text{O-U}_{0.27}$  solutions over a larger length scale. The  $\text{Li-H}_2\text{O-MU}_{0.27}$  solution contains various nanoscale clusters with core-shell-like solvation structure (left inset), leading to a localized super-high concentration of LiTFSI in the solution. In sharp contrast, the  $\text{Li-H}_2\text{O-U}_{0.27}$  solution demonstrates a globally connected network (right inset), suggesting the occurrence of solidification.

(E) Calculated pDOS of  $\text{Li-H}_2\text{O-MU}_{0.00}$  and  $\text{Li-H}_2\text{O-MU}_{0.27}$  solutions.

stability window of electrolyte beneficial for a higher energy-density aqueous battery. To reveal the role of MU in the concentrated aqueous electrolyte, *ab initio* MD (AIMD) was performed to model the MU-assisted  $\text{Li-H}_2\text{O-MU}_{0.27}$  and MU-free  $\text{Li-H}_2\text{O-MU}_{0.00}$  solutions. A typical snapshot of the MU-assisted solution structure was shown in Figure 5A. We found that  $\text{Li}^+$  is mostly coordinated with  $\text{H}_2\text{O}$ ,  $\text{TFSI}^-$ ,

and MU via  $\text{Li}\cdots\text{O}$  interactions. Because of the three functional groups (C=O,  $\text{NH}_2$ , NH), MU can interact with both  $\text{H}_2\text{O}$  and  $\text{TFSI}^-$  via hydrogen bonds. We calculated radial distribution functions (RDFs) of  $\text{MU}-\text{H}_2\text{O}$  and  $\text{MU}-\text{TFSI}^-$  to identify the microscopic hydrogen bonding network. Shown in Figure 5B, the results clearly indicate MU mainly interacts with  $\text{H}_2\text{O}$  and  $\text{TFSI}^-$  via  $\text{C}=\text{O}\cdots\text{H}-\text{O}$  and  $\text{NH}_2\cdots\text{O}=\text{S}$ , respectively, demonstrating a bifunction nature of MU that regulates hydrogen bonds with both water and anions due to its unique donor-acceptor structure. Such bifunctional character enables flexible coordination among MU,  $\text{H}_2\text{O}$ ,  $\text{TFSI}^-$ , and  $\text{Li}^+$ , leading to a novel solvation structure (see discussions below). By adding MU, the content of free-state water is greatly decreased from 29% to 5%, showing the same trend as observed by Fourier transform infrared (FTIR) spectra (Figures 2D and S1). Meanwhile, the average coordination number of  $\text{TFSI}^-$  to  $\text{Li}^+$  significantly increases from 2 to 2.6 (see Figure S30), suggesting overall enhanced  $\text{Li}\cdots\text{TFSI}$  interactions in the MU-assisted solution, consistent with the Raman results (Figure 2E). Moreover, the computed Li–Li RDF shows three RDF peaks, corresponding to  $\text{H}_2\text{O}$ -bridged Li pairs ( $\sim 3.5$  Å),  $\text{TFSI}$ -bridged Li pairs ( $6\sim 8$  Å), and the average length of  $\text{Li}\cdots\text{TFSI}\cdots\text{Li}\cdots\text{TFSI}\cdots\text{Li}$  ( $10\sim 15$  Å), respectively (see Figure 5C). Among them, the third peak that reflects long-range ordering can serve as a good indicator of the compactness of  $\text{Li}\cdots\text{TFSI}$  network in solution. Evidently, the position of the third peak shifts toward a lower value in the MU-assisted solution as compared to that in the MU-free solution, implying a more compact cation-anion network (a higher content of LiTFSI) in the former.

To understand how the introduction of MU enhances the solubility of LiTFSI in the water, we examine the solution structures over a larger length scale. A salt-concentrated solution generally contains various nanoscale clusters (contact ion pairs or aggregates) that are made of cations, anions, and solvents; inside the cluster, the constitutional ions/molecules are usually bonded to each other through strong ionic or covalent interactions. These clusters then connect to each other loosely through weak van der Waals forces.<sup>33,38</sup> During the whole AIMD simulation time ( $>10$  ps), we found the presence of a few small clusters in both  $\text{Li}-\text{H}_2\text{O}-\text{MU}_{0.00}$  and  $\text{Li}-\text{H}_2\text{O}-\text{MU}_{0.27}$  systems, as shown in Figure 5D and Figure S31 for a typical snapshot. For the  $\text{Li}-\text{H}_2\text{O}-\text{MU}_{0.00}$  system, the majority of water molecules are coordinated to ions within the clusters while the others remain relatively mobile (free state) between clusters. Interestingly, for the  $\text{Li}-\text{H}_2\text{O}-\text{MU}_{0.27}$  system, both water and MU molecules predominantly occupy the narrow interspaces between clusters, whereas the interior of cluster is solely composed of  $\text{Li}^+-\text{TFSI}^-$  networks. Such solution structure, being markedly different from that of the  $\text{Li}-\text{H}_2\text{O}-\text{MU}_{0.00}$  system, resembles a “core-shell” structure in which the compact anion-cation network serves as the core, surrounded by a less-dense shell formed by MU and water molecules. It is noted that the MU and water molecules in the shell are still strongly coordinated with  $\text{Li}^+$ . The fact that the  $\text{Li}-\text{H}_2\text{O}-\text{MU}_{0.27}$  solution has an almost identical Raman spectrum with pristine LiTFSI salt supports the microscopic picture obtained with AIMD (see Figure S2). This peculiar solution structure maintains super-high LiTFSI concentrations at the nanoscale (core region) while being structurally fluid (shell region), explaining the high solubility of LiTFSI in MU and  $\text{H}_2\text{O}$  as well as low content of free-state water molecules.

Further experimental and theoretical investigations highlighted the importance of the structural asymmetry of MU molecule for the emergence of core-shell-like solution structure. As shown in Figure 2B, the introduction of structurally symmetric U failed to increase the solubility of LiTFSI in the water despite it also having donor-acceptor functional groups almost identical to MU. AIMD allows for the modeling the solution structure of  $\text{Li}-\text{H}_2\text{O}-\text{U}_{0.27}$  (70:54:46) despite this composition not being

achievable experimentally due to salt precipitation. Interestingly, we found a globally connected network that is constructed by  $\text{Li}^+$  cations and  $\text{TFSI}^-$  anions, and the water and U molecules distribute nearly homogeneously within the network (Figure 5D). The disappearance of small clusters in the simulated structure of  $\text{Li-H}_2\text{O-U}_{0.27}$  system suggests that it cannot maintain a liquid state any longer and the solidification will occur (corresponding to salt precipitation in experiments). Therefore, we suggest that it is the combination of structural asymmetry and donor-acceptor bifunctional character of MU responsible for the formation of the peculiar core-shell-like solvation structure, which not only accommodates a super-high content of  $\text{LiTFSI}$  salt in the cluster but also prevents these clusters from amalgamating together, eventually leading to an enhanced solubility of  $\text{LiTFSI}$  in the solution.

The notable change of the solvation structure of solution will inevitably induce the change of its electronic structure. The calculated projected density of states (Figure 5E) indicated that, for the MU-free solution, the conduction band minimum consists of states from  $\text{TFSI}^-$  with nonnegligible contributions from states of  $\text{H}_2\text{O}$ , which suggests a reductive decomposition of  $\text{TFSI}^-$  accompanied with  $\text{H}_2\text{O}$  decomposition at a certain low potential. In contrast, for the MU-assisted solution, the lowest unoccupied molecular orbital (LUMO) of  $\text{H}_2\text{O}$  shifts upward to a much higher energy level (even higher than the LUMO of MU), and thus, the conduction band minimum of the solution is predominantly composed of states from  $\text{TFSI}^-$  without any overlap of states from  $\text{H}_2\text{O}$ . This substantially enhanced energy of the LUMO of  $\text{H}_2\text{O}$  suggests that water reduction in the concentrated aqueous solution can be considerably suppressed at low potentials by adding MU, consistent with the DEMS results (Figure 3A). When looking at the valence band maximum of the solution, the highest occupied molecular orbital (HOMO) of  $\text{H}_2\text{O}$  shifted toward a lower energy considerably, suggesting the oxidation of  $\text{H}_2\text{O}$  is not preferred in the  $\text{Li-H}_2\text{O-MU}$ , which is also consistent with the DEMS result (Figure 3A). Overall, the introduction of MU leads to a widening of the HOMO-LUMO gap of  $\text{H}_2\text{O}$  and a narrowing of the HOMO-LUMO gap of  $\text{TFSI}^-$  and MU, which suppresses the decomposition of  $\text{H}_2\text{O}$  and facilitates the production of a good passivation film on the electrode/electrolyte interphases via the decomposition of  $\text{TFSI}^-$  and MU, and thus, contributes to a wider electrochemical stability window.

A high-voltage aqueous battery requires a stable electrode/electrolyte interphase. The suppression of water reduction will alleviate  $\text{H}_2$  gas production and subsequent gas-induced exfoliation of SEI and thus favor the formation of a good SEI on the anode. We observed the cycled  $\text{NbO}_2$  particle by transmission electron microscopy (TEM) and found a SEI with a thickness of ca. 15 nm formed on the  $\text{NbO}_2$  surface (see Figure S32). Moreover, we also examined the electrolyte left in glass fiber after 20 cycles by attenuated total reflectance Fourier transform infrared (ATR-FTIR) and found no change as compared to the fresh electrolyte (see Figure S33), which suggests this SEI is stable and consumes little electrolyte during cycling. To monitor the formation process of SEI in the MU-assisted electrolyte, *in situ* ATR-FTIR spectroscopy was performed on the  $\text{NbO}_2$  anode during the initial two charge-discharge cycles. As shown in Figure 6A, when the  $\text{NbO}_2|\text{LiMn}_2\text{O}_4$  battery was charged to 2 V, a counter-absorbance of IR signal at  $900\sim 1300\text{ cm}^{-1}$  was observed, which is resulted from the formation of TFSI-derived inorganic SEI that adheres on the surface of ATR crystal and causes the compensation of electrolyte background. The same phenomenon was also observed on the LTO anode using the MU-free electrolyte, whose SEI is mainly composed of inorganic  $\text{LiF}$  derived from  $\text{TFSI}^-$  (see Figure S34). When charging at above 2.2 V, new IR absorbance peaks attributed to the vibrations of N-H ( $3,460, 3,345, 1,590\text{ cm}^{-1}$ ), C=O ( $1,645\text{ cm}^{-1}$ ), C-N ( $1,550, 1,420\text{ cm}^{-1}$ ), and

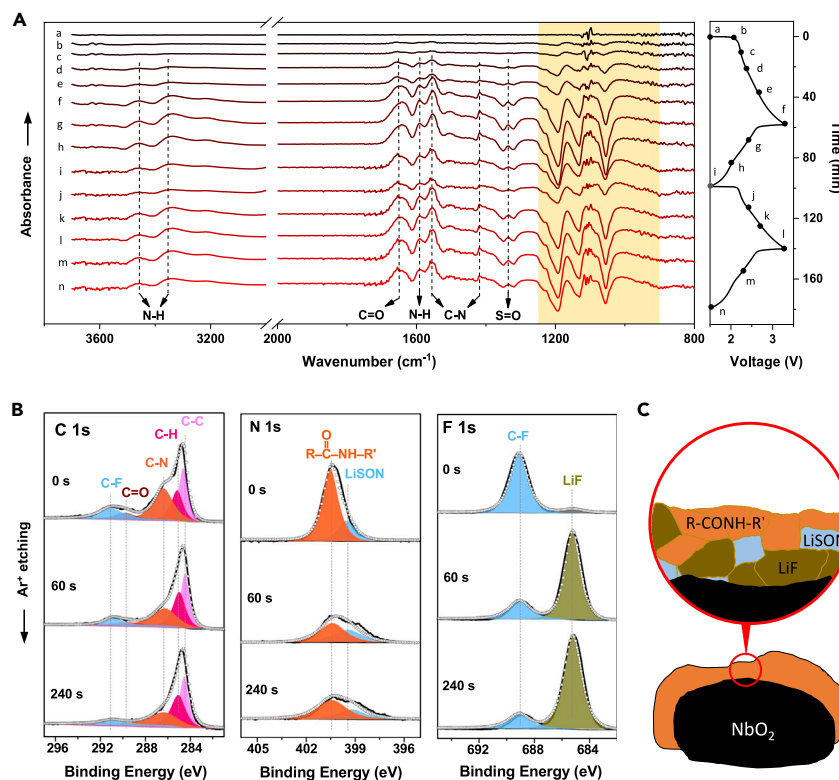


**Figure 6. Investigation of the interphase between the NbO<sub>2</sub> electrode and the Li-H<sub>2</sub>O-MU<sub>0.27</sub> electrolyte**

(A) *In situ* ATR-FTIR spectra of the NbO<sub>2</sub> electrode surface during the initial two charge-discharge cycles of the NbO<sub>2</sub>/LiMn<sub>2</sub>O<sub>4</sub> full cell. The SEI formation on the NbO<sub>2</sub> electrode starts in the charging at 2.0 V; both TFSI and MU contribute to the SEI formation.

(B) XPS spectra of the cycled NbO<sub>2</sub> electrode upon Ar<sup>+</sup> sputtering.

(C) Schematic illustration of the organic-inorganic SEI derived from the Li-H<sub>2</sub>O-MU<sub>0.27</sub> solution. MU efficiently strengthens the SEI via introducing an organic amide component of R-CONH-R', and thus, realizes a stable charge-discharge cycling of low-potential NbO<sub>2</sub> anode. LiSON represents lithium sulfur oxynitride.

S=O (1,336 cm<sup>-1</sup>) appear. After that, these IR signals keep stable during the subsequent charge/discharge process, evidencing that a stable SEI has formed on the NbO<sub>2</sub> anode in the initial charging process. This result is also consistent with the variance of battery resistance and electrolyte composition during the cycling (see Figure S35). By associating the SEI's chemical composition with the electrolyte ingredients, we can deduce that the species of N-H, C=O, and C-N are derived from the MU reduction, while that of S=O is derived from TFSI reduction. Thereby, it is unambiguous that the SEI generated in the MU-assisted electrolyte is via a prior reduction of TFSI<sup>-</sup> anions followed by a reduction of MU molecules. The chemical information of SEI revealed by IR was corroborated by X-ray photoelectron spectroscopy (XPS) measurement. The MU-derived organic amide specie of R-CONH-R' (C1s, 286.3 eV; N1s, 400.5 eV) and the TFSI<sup>-</sup>-derived inorganic species of LiF (F1s, 685.2 eV) and lithium sulfur oxynitride (LiSON N1s, 399.6 eV) can be identified from Figure 6B. As Ar<sup>+</sup> sputtering proceeds, the content of the R-CONH-R' species decreases while that of LiF increases along with the depth of SEI layer, suggesting that an organic-inorganic hierarchical SEI with an outer R-CONH-R' and an inner LiF has formed as schematically demonstrated in Figure 6C. These results demonstrate that the outer layer of MU-derived organic species can compactly cover the

inner layer of LiF, which efficiently suppresses the water reduction and contributes to such a remarkable expanded electrochemical stability window.

### Conclusions

We developed a novel asymmetric donor-acceptor molecule-regulated aqueous electrolyte that overcomes various challenges posed by conventional aqueous (hybrid) electrolytes. First, all the ingredients are nonflammable, a guarantee of high-safety electrolyte, which is distinguished from previously reported nonaqueous/aqueous hybrid electrolytes, whose safety property is largely compromised by the usage of flammable materials. Second, the structurally asymmetric MU molecule with donor-acceptor functional groups efficiently regulates the solution structure via adjusting hydrogen-bonding interactions with both water molecules and TFSI<sup>-</sup> anions, leading to the formation of peculiar core-shell-like clusters with localized super-high LiTFSI concentrations in aqueous solution, surmounting the issue of limited salt solubility faced by conventional salt-concentrated aqueous electrolytes. More importantly, this approach does not increase the mass fraction of LiTFSI as the mole fraction of LiTFSI increases, which significantly eases the cost concern. Third, the introduced MU also brings stable organic components into SEI and contributes to a robust organic-inorganic hierarchical interphase on the anode, alleviating the cathodic challenge of hydrogen evolution encountered by conventional aqueous electrolytes. Through a series of *in situ/ex situ* characterizations and AIMD simulations, we demonstrate that this new aqueous electrolyte efficiently suppresses hydrogen evolution to 0.5 V versus Li<sup>+</sup>/Li, greatly expands the electrochemical stability window to 4.5 V, and enables a stable charge-discharge operation of a rocking-chair NbO<sub>2</sub>/LiMn<sub>2</sub>O<sub>4</sub> full cell (175 Wh kg<sup>-1</sup>) under a harsh testing condition of a low electrolyte loading, no excess Li resource (N/P ≥ 1), no electrode pre-coating, and commercial Al current collector for both anode and cathode. Considering the practical application, the salt content in the present Li-H<sub>2</sub>O-MU<sub>0.27</sub> (4.69 mol L<sup>-1</sup>) is still high. Using molecules with a larger size and heavier weight than MU can further decrease the salt content as well as the density of electrolyte, which could contribute to a lower cost. In addition, if used in a lower voltage battery, such as Li<sub>4</sub>Ti<sub>5</sub>O<sub>12</sub>/LiMn<sub>2</sub>O<sub>4</sub>, a dilute electrolyte of Li-H<sub>2</sub>O-MU<sub>0.73</sub> (1.41 mol L<sup>-1</sup>) is capable of a stable charge-discharge operation of the battery (see [Figure S36](#)). Consequently, this unique electrolyte design by integrating nonflammable asymmetric donor-acceptor molecules with aqueous solutions truly inherits high safety of aqueous electrolytes and, meanwhile, remarkably widens the electrochemical stability window, boosting the development of safe, cheap, and high-energy-density aqueous batteries not limited to Li ion.

## EXPERIMENTAL PROCEDURES

### Resource availability

#### Lead contact

Further information and requests for resources and materials should be directed to and will be fulfilled by the lead contact, Jianhui Wang ([wangjianhui@westlake.edu.cn](mailto:wangjianhui@westlake.edu.cn)).

#### Materials availability

The materials in this study will be made available upon reasonable request.

#### Data and code availability

The datasets generated in this study are available from the lead contact on reasonable request.

## Materials and batteries

### *Electrolyte preparations*

Lithium bis(trifluoromethane sulfonyl) imide (LiTFSI), lithium trifluoromethanesulfonate (LiOTf), dimethyl carbonate (DMC), and acetonitrile (AN) with a purity of >99% were purchased from DodoChem. Methyurea (MU, >98%), urea (U, >98%), polyethylene glycol (PEG 400, >98%), maltose (sugar, >99%), and lithium acetate (LiAc, >99%) were purchased from Sigma-Aldrich. Deionized water for aqueous electrolytes was produced by a water purification system (Millipore, Milli-Q Intergal 15). The detailed electrolyte preparation procedure is as follows: first, 10 H<sub>2</sub>O/MU mixtures with different molar ratios (100:0, 86:14, 74:26, 66:34, 54:46, 45:55, 36:64, 27:73, 14:86, 0:100) were prepared. Second, LiTFSI salt was dissolved into these H<sub>2</sub>O/MU mixtures to form a clear and saturated solution with the help of a mixer (Thinky, AR-100). The mole and mass fractions of ingredients in as-prepared electrolytes are listed in [Table S2](#). For comparison, aqueous electrolytes of Li-H<sub>2</sub>O-DMC<sub>0.16</sub>, Li-H<sub>2</sub>O-AN<sub>0.34</sub>, Li-H<sub>2</sub>O-PEG<sub>0.30</sub>, and Li-H<sub>2</sub>O-Sugar<sub>0.08</sub> were prepared by hybridizing LiTFSI-H<sub>2</sub>O or LiAc-H<sub>2</sub>O mixtures with flammable organic chemicals of DMC, AN, PEG, and sugar in the same way. Their compositions are listed in [Table S3](#). In addition, bisalt-concentrated electrolytes with salt/solvent molar ratio of LiTFSI:LiOTf:H<sub>2</sub>O 0.75:0.25:2 (named as Li(TFSI)<sub>0.75</sub>(OTf)<sub>0.25</sub>(H<sub>2</sub>O)<sub>2</sub>) and LiTFSI:LiBETI:H<sub>2</sub>O 0.7:0.3:2 (named as Li(TFSI)<sub>0.7</sub>(BETI)<sub>0.3</sub>(H<sub>2</sub>O)<sub>2</sub>) were also prepared for comparison.

### *Electrode preparations*

The high-capacity NbO<sub>2</sub> material was home-synthesized by (1) ball milling pristine niobium pentoxide powder (Nb<sub>2</sub>O<sub>5</sub>, Sigma-Aldrich, >99.9%) in a planetary ball mill (Shanghai Jing Xin, JX-2G) and following (2) a calcination in a tube furnace (Boyuntong, LT1200) at 900°C under a mixed gas flow of Ar/H<sub>2</sub> (v/v 95:5). Li<sub>4</sub>Ti<sub>5</sub>O<sub>12</sub>, LiMn<sub>2</sub>O<sub>4</sub> materials were purchased from Guangdong Canrd New Energy Technology Co. Ltd. All these electrode materials were used directly without any surface coating. The NbO<sub>2</sub> and Li<sub>4</sub>Ti<sub>5</sub>O<sub>12</sub> electrodes were fabricated by mixing the active material, acetylene black (SZ-Kejing), and polyvinylidene fluoride (PVDF, SZ-Kejing) with a weight ratio of 80:10:10 in N-methylpyrrolidinone (NMP, SZ-Kejing). The LiMn<sub>2</sub>O<sub>4</sub> electrodes were obtained by stirring active materials, acetylene black, and sodium alginate (Guangdong Canrd New Energy Technology Co. Ltd.) with a weight ratio of 85:10:5 in deionized water. All the slurries were then cast uniformly on bare Al foil (DodoChem, 20 mm thickness) for both cathode and anode using an automatic coater (HF-Kejing, MSK-AFA-I). The obtained electrodes were dried at 120°C under vacuum for 12 h. For the LiMn<sub>2</sub>O<sub>4</sub> electrode, the mass loading was 7~10 mg cm<sup>-2</sup>; for the NbO<sub>2</sub> and Li<sub>4</sub>Ti<sub>5</sub>O<sub>12</sub> electrodes, the mass loading was 4~5 mg cm<sup>-2</sup>.

### *Cell assembly and electrochemical measurements*

Three-electrode cells were assembled for linear sweep voltammetry (LSV), cyclic voltammetry (CV), and chronoamperometry measurements on a potentiostat (BioLogic, MPG-2). Active carbon and Ag/AgCl (in saturated KCl solution, 3.239V versus Li<sup>+</sup>/Li) were used as the counter and reference electrodes, respectively. For LSV tests, conductive carbon-coated Al foil (Guangzhou Nano New Material Technology Co. Ltd.) was used as the working electrode to evaluate the electrochemical stability window of the studied electrolytes. The scan rate was 5 mV s<sup>-1</sup>. For CV tests, NbO<sub>2</sub>, Li<sub>4</sub>Ti<sub>5</sub>O<sub>12</sub>, and LiMn<sub>2</sub>O<sub>4</sub> were used as the working electrodes to examine the electrode reaction reversibility in the electrolytes. The scan rate was 0.5 mV s<sup>-1</sup>.

Full cells were assembled as CR2032-type coin cells in atmosphere environment using LiMn<sub>2</sub>O<sub>4</sub> as the cathode, NbO<sub>2</sub> or Li<sub>4</sub>Ti<sub>5</sub>O<sub>12</sub> as the anode, and glass fiber (Whatman, GF/D) as the separator. The negative/positive (N/P) capacity ratio was



1~1.1. The amount of electrolyte in a coin cell was 30 mL, corresponding to an electrolyte/capacity (E/C) ratio of ca. 30 mL mA<sup>h</sup><sup>-1</sup>. The stainless-steel cell case was used for the cathode and the Al-Clad cell case was used for the anode. At least three duplicate full cells were assembled in this work. Galvanostatic charge-discharge cycling and rate capability tests were conducted on a battery test system (Neware, CT-4008) at 25°C. Charge and discharge were conducted at the same C-rate without using a constant-voltage mode at both ends of the charge and discharge. The energy density of full cell was calculated by (total capacity × average voltage / total weight of cathode and anode).

## Characterizations

### *Characterizations of solution structures*

The coordination state of water molecules in the solutions were studied by an attenuated total reflection-fourier transform infrared spectrometer (ATR-FTIR, Thermo-Fisher, iS50). The spectra were recorded in 32 scans with a resolution of 4 cm<sup>-1</sup>. The coordination state of TFSI<sup>-</sup> anions in the electrolytes were examined by a Raman spectrometer (Anton Paar, Cora 5700) with an exciting laser of 785 nm. <sup>1</sup>H NMR spectra of Li-H<sub>2</sub>O-MU<sub>x</sub> were conducted on a Bruker Avance 500 MHz Solution NMR Spectrometer at room temperature (see [Figure S37](#)). <sup>1</sup>H signal of tetramethylsilane at 0 ppm was used as the reference.

### *Measurements of physical and chemical properties of electrolytes*

The viscosity and density of solutions were evaluated by a kinematic viscometer (Anton Paar, SVM 3001). The ionic conductivity was measured by an AC impedance spectroscopy (IVIUM, OctoStat200) in a symmetric Pt|electrolyte|Pt cell. Weight loss of solutions upon heating were measured on a thermogravimetric analyzer (Mettler-Toledo, 3+/1600 HT). The samples were sealed in an Al pan with a pinhole for gas escape during the measurements. The ramping rate is 10°C min<sup>-1</sup>, and the purge Ar flow is 50 mL min<sup>-1</sup>. Photo images of the Li-H<sub>2</sub>O-MU<sub>0.27</sub> sample before and after a thermogravimetric test (heating to 100°C) were shown in [Figure S38](#). Self-extinguishing times (SETs) of the electrolytes were determined in a flame test, in which the glass fiber soaked with 0.5 g electrolyte was ignited by a propane-oxygen torch burner. The temperature of the propane-oxygen flame is ca. 2,600°C. Flash points were examined by a micro flash point tester (Wanmu Instrument, WM-3000D). The tests were performed according to the rapid balance closed cup method. Both SET and flash point tests for each sample were repeated for several times to obtain reliable results.

### *Characterizations of materials' morphology and composition*

The morphology and crystal phase of home-made NbO<sub>2</sub> sample were characterized by a field emission scanning electron microscope (FE-SEM, Gemini500) and an X-ray diffractometer (Bruker, D8 Advance) with Cu-Kα radiation, respectively. The surface analysis of the cycled electrodes was performed on an X-ray photoelectron spectrometer (XPS, ESCALAB Xi<sup>+</sup>) with Al-Kα radiation. A charge neutralizer was applied to compensate for the sample surface charge. The binding energy was calibrated using C1s peak at 284.8 eV. The depth profile was obtained via Ar<sup>+</sup> sputtering at 1 kV. The studied electrodes were subjected to a rinse in the dimethyl carbonate solvent followed by a vacuum dry before XPS measurements.

### *In situ DEMS measurements*

*In situ* DEMS measurements were applied to detect hydrogen and oxygen gases generated on the carbon-coated Al electrode in a LSV test. A membrane inlet was positioned over the Al electrode surface with a tiny distance of about 40 mm

adjusted by an optical microscope. The generated gases were pumped through the membrane inlet and analyzed by a quadrupole mass spectrometer (QAS 100, Shanghai Linglu). The LSV test was conducted in a three-electrode cell, which included a counter electrode of active carbon, a reference electrode of Ag/AgCl (in saturated KCl solution), and a carbon-coated Al working electrode. The scan rate was  $5 \text{ mV s}^{-1}$  controlled by a potentiostat (IVIUM, OctoStat200). Before the DEMS measurement, pure Ar gas was flushed for 2 h to remove the air in the cell.

#### *In situ* ATR-FTIR measurements

*In situ* ART-FTIR measurements were performed in a homemade two-electrode cell that was fixed on the sample stage of ATR (PIKE, VeeMAX III). The studied  $\text{NbO}_2$  or  $\text{Li}_4\text{Ti}_5\text{O}_{12}$  anodes were pressed on the Ge crystal in order to get sufficiently good FTIR signals. The  $\text{NbO}_2|\text{LiMn}_2\text{O}_4$  or  $\text{Li}_4\text{Ti}_5\text{O}_{12}|\text{LiMn}_2\text{O}_4$  cell was charged/discharged on a potentiostat (IVIUM, OctoStat200) at 0.7 C rate. The initial two charge-discharge cycles were observed by a FTIR spectrometer (ThermoFisher, iS50) to reveal the SEI formation on the studied electrodes. For each FTIR test, the spectra were recorded in 32 scans with a resolution of  $4 \text{ cm}^{-1}$ .

#### Simulations

The solution structure is theoretically investigated by the *ab initio* molecule dynamic (MD) simulations, as implemented in the computational software Vienna *ab initio* simulation package.<sup>39,40</sup> The projector augmented wave method is used for electronic structure calculation.<sup>41</sup> The exchange-correlation interaction is described by PBE functional with D3 dispersion correction from Grimme.<sup>42,43</sup> The cutoff energies and electronic energy self-consistency tolerance are set to 350 eV and  $1 \times 10^{-6}$  eV, respectively.  $\text{Li-H}_2\text{O-MU}_{0.00}$ ,  $\text{Li-H}_2\text{O-MU}_{0.27}$ , and  $\text{Li-H}_2\text{O-U}_{0.27}$  solutions with  $\text{Li-H}_2\text{O:organic}$  molar ratios of 15:38:0, 18:14:12, and 18:14:12 were calculated in cubic supercells with lattice constants of 16.86, 18.36, and 18.21 Å, respectively. The gamma-point sampling is used for MD, and a  $3 \times 3 \times 3$  *k*-point grid is used for density of states calculations. The temperature of NVT ensemble is controlled using the Nosé-Hoover thermostat.<sup>44,45</sup> The solution is first equilibrated at a higher temperature (698 K, 5 ps) to generate configurations with fully mixed solvents and solutes. The high-temperature equilibrated solution structures are then used as the initial configurations for MD simulations at room temperature (298 K). To confirm the structural convergence of AIMD, three simulations with different initial configurations for different running time (10~25 ps) were performed (see Figures S39–S44). Statistical averages are computed from trajectories of at least 5 ps.

#### SUPPLEMENTAL INFORMATION

Supplemental information can be found online at <https://doi.org/10.1016/j.joule.2022.01.002>.

#### ACKNOWLEDGMENTS

This work was supported by Westlake Education Foundation and National Natural Science Foundation of China (grant no. 21975207). The authors thank Westlake Instrumentation and Service Centers for Physical Sciences and Molecular Sciences for characterization support and Westlake HPC Center for computation support.

#### AUTHOR CONTRIBUTIONS

J.W. and R.L. designed the experiments. R.L. carried out the experiments. S.L. directed the computation. S.L. and C.K. designed and performed the AIMD

simulations. All authors contributed to the discussion and the manuscript preparation. R.L. and C.K. contributed equally to this work. J.W. conceived and led the project.

## DECLARATION OF INTERESTS

The authors declare no competing interests.

Received: July 8, 2021

Revised: October 20, 2021

Accepted: January 6, 2022

Published: January 14, 2022

## REFERENCES

- Kim, H., Hong, J., Park, K.Y., Kim, H., Kim, S.W., and Kang, K. (2014). Aqueous rechargeable Li and Na ion batteries. *Chem. Rev.* **114**, 11788–11827.
- Huang, J., Guo, Z., Ma, Y., Bin, D., Wang, Y., and Xia, Y. (2019). Recent Progress of Rechargeable Batteries Using Mild Aqueous Electrolytes. *Small Methods* **3**, 1800272.
- Yamada, Y., Wang, J., Ko, S., Watanabe, E., and Yamada, A. (2019). Advances and issues in developing salt-concentrated battery electrolytes. *Nat. Energy* **4**, 269–280.
- Borodin, O., Self, J., Persson, K.A., Wang, C., and Xu, K. (2020). Uncharted Waters: Super-Concentrated Electrolytes. *Joule* **4**, 69–100.
- Li, M., Wang, C., Chen, Z., Xu, K., and Lu, J. (2020). New Concepts in Electrolytes. *Chem. Rev.* **120**, 6783–6819.
- Chao, D., and Qiao, S.-Z. (2020). Toward High-Voltage Aqueous Batteries: Super- or Low-Concentrated Electrolyte? *Joule* **4**, 1846–1851.
- Suo, L., Borodin, O., Gao, T., Olguin, M., Ho, J., Fan, X., Luo, C., Wang, C., and Xu, K. (2015). “Water-in-salt” electrolyte enables high-voltage aqueous lithium-ion chemistries. *Science* **350**, 938–943.
- Suo, L., Oh, D., Lin, Y., Zhuo, Z., Borodin, O., Gao, T., Wang, F., Kushima, A., Wang, Z., Kim, H.C., et al. (2017). How Solid-Electrolyte Interphase Forms in Aqueous Electrolytes. *J. Am. Chem. Soc.* **139**, 18670–18680.
- Suo, L., Borodin, O., Sun, W., Fan, X., Yang, C., Wang, F., Gao, T., Ma, Z., Schroeder, M., von Cresce, A., et al. (2016). Advanced High-Voltage Aqueous Lithium-Ion Battery Enabled by “Water-in-Bisalt” Electrolyte. *Angew. Chem. Int. Ed. Engl.* **55**, 7136–7141.
- Yamada, Y., Usui, K., Sodeyama, K., Ko, S., Tateyama, Y., and Yamada, A. (2016). Hydrate-melt electrolytes for high-energy-density aqueous batteries. *Nat. Energy* **1**, 16129.
- Lukatskaya, M.R., Feldblyum, J.I., Mackanic, D.G., Lissel, F., Michels, D.L., Cui, Y., and Bao, Z. (2018). Concentrated mixed cation acetate “water-in-salt” solutions as green and low-cost high voltage electrolytes for aqueous batteries. *Energy Environ. Sci.* **11**, 2876–2883.
- Ko, S., Yamada, Y., Miyazaki, K., Shimada, T., Watanabe, E., Tateyama, Y., Kamiya, T., Honda, T., Akikusa, J., and Yamada, A. (2019). Lithium-salt monohydrate melt: A stable electrolyte for aqueous lithium-ion batteries. *Electrochem. Commun.* **104**, 1904961.
- Yang, C., Chen, J., Qing, T., Fan, X., Sun, W., von Cresce, A., Ding, M.S., Borodin, O., Vatamanu, J., Schroeder, M.A., et al. (2017). 4.0 V Aqueous Li-Ion Batteries. *Joule* **1**, 122–132.
- Yang, C., Chen, J., Ji, X., Pollard, T.P., Lü, X., Sun, C.J., Hou, S., Liu, Q., Liu, C., Qing, T., et al. (2019). Aqueous Li-ion battery enabled by halogen conversion-intercalation chemistry in graphite. *Nature* **569**, 245–250.
- Zhang, J., Cui, C., Wang, P.-F., Li, Q., Chen, L., Han, F., Jin, T., Liu, S., Choudhary, H., Raghavan, S.R., et al. (2020). “Water-in-salt” polymer electrolyte for Li-ion batteries. *Energy Environ. Sci.* **13**, 2878–2887.
- Wang, F., Borodin, O., Ding, M.S., Gobet, M., Vatamanu, J., Fan, X., Gao, T., Eidson, N., Liang, Y., Sun, W., et al. (2018). Hybrid Aqueous/Non-aqueous Electrolyte for Safe and High-Energy Li-Ion Batteries. *Joule* **2**, 927–937.
- Dou, Q., Lei, S., Wang, D.-W., Zhang, Q., Xiao, D., Guo, H., Wang, A., Yang, H., Li, Y., Shi, S., and Yan, X. (2018). Safe and high-rate supercapacitors based on an “acetonitrile/water in salt” hybrid electrolyte. *Energy Environ. Sci.* **11**, 3212–3219.
- Chen, J., Vatamanu, J., Xing, L., Borodin, O., Chen, H., Guan, X., Liu, X., Xu, K., and Li, W. (2020). Improving Electrochemical Stability and Low-Temperature Performance with Water/Acetonitrile Hybrid Electrolytes. *Adv. Energy Mater.* **10**, 1902654.
- Yang, W., Du, X., Zhao, J., Chen, Z., Li, J., Xie, J., Zhang, Y., Cui, Z., Kong, Q., Zhao, Z., et al. (2020). Hydrated Eutectic Electrolytes with Ligand-Oriented Solvation Shells for Long-Cycling Zinc-Organic Batteries. *Joule* **4**, 1557–1574.
- Zhang, H., Qin, B., Han, J., and Passerini, S. (2018). Aqueous/Nonaqueous Hybrid Electrolyte for Sodium-Ion Batteries. *ACS Energy Lett.* **3**, 1769–1770.
- Jiang, P., Chen, L., Shao, H., Huang, S., Wang, Q., Su, Y., Yan, X., Liang, X., Zhang, J., Feng, J., and Liu, Z. (2019). Methylsulfonylmethane-Based Deep Eutectic Solvent as a New Type of Green Electrolyte for a High-Energy-Density Aqueous Lithium-Ion Battery. *ACS Energy Lett.* **4**, 1419–1426.
- Shang, Y., Chen, N., Li, Y., Chen, S., Lai, J., Huang, Y., Qu, W., Wu, F., and Chen, R. (2020). An “Ether-In-Water” Electrolyte Boosts Stable Interfacial Chemistry for Aqueous Lithium-Ion Batteries. *Adv. Mater.* **32**, e2004017.
- Nian, Q., Wang, J., Liu, S., Sun, T., Zheng, S., Zhang, Y., Tao, Z., and Chen, J. (2019). Aqueous Batteries Operated at -50 °C. *Angew. Chem. Int. Ed. Engl.* **58**, 16994–16999.
- Lu, X., Jiménez-Riobóo, R.J., Leech, D., Gutiérrez, M.C., Ferrer, M.L., and Del Monte, F. (2020). Aqueous-Eutectic-in-Salt Electrolytes for High-Energy-Density Supercapacitors with an Operational Temperature Window of 100 °C, from -35 to +65 °C. *ACS Appl. Mater. Interfaces* **12**, 29181–29193.
- Bi, H., Wang, X., Liu, H., He, Y., Wang, W., Deng, W., Ma, X., Wang, Y., Rao, W., Chai, Y., et al. (2020). A Universal Approach to Aqueous Energy Storage via Ultralow-Cost Electrolyte with Super-Concentrated Sugar as Hydrogen-Bond-Regulated Solute. *Adv. Mater.* **32**, e2000074.
- Xie, J., Liang, Z., and Lu, Y.C. (2020). Molecular crowding electrolytes for high-voltage aqueous batteries. *Nat. Mater.* **19**, 1006–1011.
- Wang, J., Yamada, Y., Sodeyama, K., Watanabe, E., Takada, K., Tateyama, Y., and Yamada, A. (2018). Fire-extinguishing organic electrolytes for safe batteries. *Nat. Energy* **3**, 22–29.
- Hess, S., Wohlfahrt-Mehrens, M., and Wachtler, M. (2015). Flammability of Li-Ion Battery Electrolytes: Flash Point and Self-Extinguishing Time Measurements. *J. Electrochem. Soc.* **162**, A3084.
- Zheng, Q., Miura, S., Miyazaki, K., Ko, S., Watanabe, E., Okoshi, M., Chou, C.P., Nishimura, Y., Nakai, H., Kamiya, T., et al. (2019). Sodium- and Potassium-Hydrate Melts Containing Asymmetric Imide Anions for High-Voltage Aqueous Batteries. *Angew. Chem. Int. Ed. Engl.* **58**, 14202–14207.
- Chen, L., Zhang, J., Li, Q., Vatamanu, J., Ji, X., Pollard, T.P., Cui, C., Hou, S., Chen, J., Yang, C., et al. (2020). A 63 m Superconcentrated

- Aqueous Electrolyte for High-Energy Li-Ion Batteries. *ACS Energy Lett.* 5, 968–974.
31. Scatena, L.F., Brown, M.G., and Richmond, G.L. (2001). Water at hydrophobic surfaces: weak hydrogen bonding and strong orientation effects. *Science* 292, 908–912.
  32. Choe, C., Lademann, J., and Darvin, M.E. (2016). Depth profiles of hydrogen bound water molecule types and their relation to lipid and protein interaction in the human stratum corneum in vivo. *Analyst (Lond.)* 141, 6329–6337.
  33. Yamada, Y., Furukawa, K., Sodeyama, K., Kikuchi, K., Yaegashi, M., Tateyama, Y., and Yamada, A. (2014). Unusual stability of acetonitrile-based superconcentrated electrolytes for fast-charging lithium-ion batteries. *J. Am. Chem. Soc.* 136, 5039–5046.
  34. Wang, J., Yamada, Y., Sodeyama, K., Chiang, C.H., Tateyama, Y., and Yamada, A. (2016). Superconcentrated electrolytes for a high-voltage lithium-ion battery. *Nat. Commun.* 7, 12032.
  35. Han, F., Zhu, Y., He, X., Mo, Y., and Wang, C. (2016). Electrochemical Stability of Li<sub>10</sub>GeP<sub>2</sub>S<sub>12</sub> and Li<sub>7</sub>La<sub>3</sub>Zr<sub>2</sub>O<sub>12</sub>. *Adv. Energy Mater.* 6, 1501590.
  36. Park, H., Lee, D., and Song, T. (2019). High capacity monoclinic Nb<sub>2</sub>O<sub>5</sub> and semiconducting NbO<sub>2</sub> composite as high-power anode material for Li-ion batteries. *J. Power Sources* 414, 377–382.
  37. Griffith, K.J., Wiaderek, K.M., Cibir, G., Marbella, L.E., and Grey, C.P. (2018). Niobium tungsten oxides for high-rate lithium-ion energy storage. *Nature* 559, 556–563.
  38. Borodin, O., Suo, L., Gobet, M., Ren, X., Wang, F., Faraone, A., Peng, J., Olguin, M., Schroeder, M., Ding, M.S., et al. (2017). Liquid Structure with Nano-Heterogeneity Promotes Cationic Transport in Concentrated Electrolytes. *ACS Nano* 11, 10462–10471.
  39. Kresse, G., and Furthmuller, J. (1996). Efficiency of ab-initio total energy calculations for metals and semiconductors using a plane-wave basis set. *Comput. Mater. Sci.* 6, 15–50.
  40. Kresse, G., and Furthmüller, J. (1996). Efficient iterative schemes for ab initio total-energy calculations using a plane-wave basis set. *Phys. Rev. B Condens. Matter* 54, 11169–11186.
  41. Blöchl, P.E. (1994). Projector augmented-wave method. *Phys. Rev. B Condens. Matter* 50, 17953–17979.
  42. Perdew, J.P., Burke, K., and Ernzerhof, M. (1996). Generalized Gradient Approximation Made Simple. *Phys. Rev. Lett.* 77, 3865–3868.
  43. Grimme, S., Ehrlich, S., and Goerigk, L. (2011). Effect of the damping function in dispersion corrected density functional theory. *J. Comput. Chem.* 32, 1456–1465.
  44. Nosé, S. (1984). A unified formulation of the constant temperature molecular dynamics methods. *J. Chem. Phys.* 81, 511–519.
  45. Hoover, W.G. (1985). Canonical dynamics: Equilibrium phase-space distributions. *Phys. Rev. A Gen. Phys.* 31, 1695–1697.

**Joule, Volume 6**

**Supplemental information**

**Asymmetric donor-acceptor molecule-regulated  
core-shell-solvation electrolyte for high-voltage  
aqueous batteries**

**Rui Lin, Changming Ke, Juner Chen, Shi Liu, and Jianhui Wang**

## Content outline

### 1 Figures

Figure S1. Quantitative analysis of infrared O-H stretching of Li-H<sub>2</sub>O-MU<sub>x</sub> solutions.

Figure S2. Raman spectra of as-prepared Li-H<sub>2</sub>O-MU solutions and pure LiTFSI powder.

Figure S3. Ion conductivity and viscosity of as-prepared Li-H<sub>2</sub>O-MU electrolytes at 25 °C.

Figure S4. Weight loss of various aqueous solutions in the thermogravimetric tests.

Figure S5. Flame tests of the Li-H<sub>2</sub>O-PEG<sub>0.30</sub> electrolyte.

Figure S6. Comparison of LSV results tested on the carbon-coated and bare Al electrodes.

Figure S7. Comparison of LSV curves on the carbon-coated Al electrodes in different scan rates.

Figure S8. In-situ DEMS monitoring hydrogen evolution during the first two cathodic LSV scans in the Li-H<sub>2</sub>O-MU<sub>0.27</sub> solution.

Figure S9. Potentiostatic curves of various aqueous electrolytes on carbon-coated Al electrode.

Figure S10. Initial charge-discharge profile of the SnO<sub>2</sub>|LiMn<sub>2</sub>O<sub>4</sub> full cell using different electrolytes.

Figure S11. Charge-discharge profiles of a precoated Li|LiMn<sub>2</sub>O<sub>4</sub> cell using the Li-H<sub>2</sub>O-MU<sub>0.27</sub> electrolyte.

Figure S12. Structural characterizations of home-made niobium oxide material.

Figure S13. Electrochemical performance of the NbO<sub>2</sub>|Li half-cell using a commercial organic electrolyte of 1M LiPF<sub>6</sub>/EC:DMC (1:1).

Figure S14. Initial charge-discharge profiles for a three-electrode cell with a NbO<sub>2</sub> anode, a LiMn<sub>2</sub>O<sub>4</sub> cathode and an Ag/AgCl reference electrode.

Figure S15. Electrochemical performance of a NbO<sub>2</sub>|LiMn<sub>2</sub>O<sub>4</sub> full cell in the Li-H<sub>2</sub>O-MU<sub>0.00</sub> electrolyte.

Figure S16. Electrochemical performance of a NbO<sub>2</sub>|LiMn<sub>2</sub>O<sub>4</sub> full cell in bisalt-concentrated Li(TFSI)<sub>0.75</sub>(OTf)<sub>0.25</sub>(H<sub>2</sub>O)<sub>2</sub> electrolyte.

Figure S17. Electrochemical performance of a NbO<sub>2</sub>|LiMn<sub>2</sub>O<sub>4</sub> full cell in bisalt-concentrated Li(TFSI)<sub>0.7</sub>(BETI)<sub>0.3</sub>(H<sub>2</sub>O)<sub>2</sub> electrolyte.

Figure S18. Charge curves of a  $\text{NbO}_2|\text{LiMn}_2\text{O}_4$  full cell at various rates in the  $\text{Li-H}_2\text{O-Sugar}_{0.08}$  electrolyte.

Figure S19. Electrochemical performance of a  $\text{NbO}_2|\text{LiMn}_2\text{O}_4$  full cell in  $\text{Li-H}_2\text{O-PEG}_{0.30}$  electrolyte.

Figure S20. Electrochemical performance of a  $\text{NbO}_2|\text{LiMn}_2\text{O}_4$  full cell in  $\text{Li-H}_2\text{O-AN}_{0.34}$  electrolyte.

Figure S21. Electrochemical performance of a  $\text{NbO}_2|\text{LiMn}_2\text{O}_4$  full cell in  $\text{Li-H}_2\text{O-DMC}_{0.16}$  electrolyte.

Figure S22. Electrochemical performance of  $\text{NbO}_2|\text{LiMn}_2\text{O}_4$  full cells using a high loading of electrolytes.

Figure S23. Electrochemical performance of  $\text{NbO}_2|\text{LiMn}_2\text{O}_4$  cells in the as-prepared MU-assisted electrolytes and various reported aqueous electrolytes.

Figure S24. Electrochemical performance of three duplicate  $\text{NbO}_2|\text{LiMn}_2\text{O}_4$  full cells in  $\text{Li-H}_2\text{O-MU}_{0.27}$  electrolyte.

Figure S25. Electrochemical performance of a  $\text{NbO}_2|\text{LiMn}_2\text{O}_4$  full cell at 0 and 55 °C.

Figure S26. DSC curves of the solutions of  $\text{Li-H}_2\text{O-MU}_{0.00}$  and  $\text{Li-H}_2\text{O-MU}_{0.27}$ .

Figure S27. Electrochemical performance of a  $\text{Li}_4\text{Ti}_5\text{O}_{12}|\text{LiMn}_2\text{O}_4$  full cell using the  $\text{Li-H}_2\text{O-MU}_{0.27}$  electrolyte.

Figure S28. LSV curves of a carbon-coated Al electrode in the electrolyte of  $\text{Li-H}_2\text{O-U}_{0.34}$ .

Figure S29. Electrochemical performance of a  $\text{NbO}_2|\text{LiMn}_2\text{O}_4$  full cell in  $\text{Li-H}_2\text{O-U}_{0.34}$  electrolyte.

Figure S30. Average coordination numbers of  $\text{TFSI}^-$ ,  $\text{H}_2\text{O}$  and MU to  $\text{Li}^+$ .

Figure S31. Solution structures of  $\text{Li-H}_2\text{O-MU}_{0.00}$ ,  $\text{Li-H}_2\text{O-MU}_{0.27}$  and  $\text{Li-H}_2\text{O-U}_{0.27}$  solutions from DFT-MD.

Figure S32. TEM image of the cycled  $\text{NbO}_2$ .

Figure S33. ATR-FTIR spectra of the  $\text{Li-H}_2\text{O-MU}_{0.27}$  electrolyte before and after cycling.

Figure S34. In-situ ATR-FTIR observation of SEI formation in a  $\text{Li}_4\text{Ti}_5\text{O}_{12}|\text{LiMn}_2\text{O}_4$  full cell using the  $\text{Li-H}_2\text{O-MU}_{0.00}$  during the initial two charge-discharge cycles.

Figure S35. Impedance spectra of the  $\text{NbO}_2|\text{LiMn}_2\text{O}_4$  full cells using the  $\text{Li-H}_2\text{O-MU}_{0.00}$  and  $\text{Li-H}_2\text{O-MU}_{0.27}$  electrolytes during the cycling.

Figure S36. A dilute Li-H<sub>2</sub>O-MU<sub>0.73</sub> electrolyte enables a stable operation of Li<sub>4</sub>Ti<sub>5</sub>O<sub>12</sub>|LiMn<sub>2</sub>O<sub>4</sub> full cell.

Figure S37. <sup>1</sup>H NMR spectra of Li-H<sub>2</sub>O-MU<sub>x</sub>.

Figure S38. Images of the Li-H<sub>2</sub>O-MU<sub>0.27</sub> sample in an Al pan.

Figure S39. Comparison of electrolyte structure of Li-H<sub>2</sub>O-MU<sub>0.27</sub> at 298 K and 698 K.

Figure S40. The structural convergence of AIMD of Li-H<sub>2</sub>O-MU<sub>0.27</sub> in 25 ps.

Figure S41. Total energy vs. time plot for a 10 ps AIMD starting with an initial configuration from 698K AIMD.

Figure S42. Structural convergence of AIMD of Li-H<sub>2</sub>O-MU<sub>0.27</sub> at 298 K using different initial configurations.

Figure S43. Final configurations of Li-H<sub>2</sub>O-U<sub>0.27</sub> in the three AIMD simulations from different configurations.

Figure S44. Mass center displacements during AIMD simulations.

## 2 Tables

Table S1. Comparison of aqueous Li-ion battery parameters of this work with those reported in literatures.

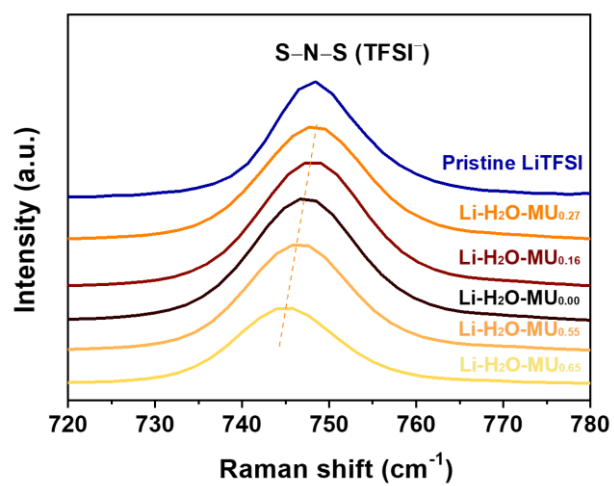
Table S2. The density, molar concentration, mole and mass fractions of ingredients of the Li-H<sub>2</sub>O-MU<sub>x</sub> electrolytes

Table S3. The mole ratios and mass percentages of ingredients of aqueous electrolytes hybridized with various flammable organic materials.

## 3 References







**Figure S2. Raman spectra of as-prepared Li-H<sub>2</sub>O-MU solutions and pure LiTFSI powder.**

Raman spectrum of Li-H<sub>2</sub>O-MU<sub>0.27</sub> shows almost identical with that of pristine LiTFSI.

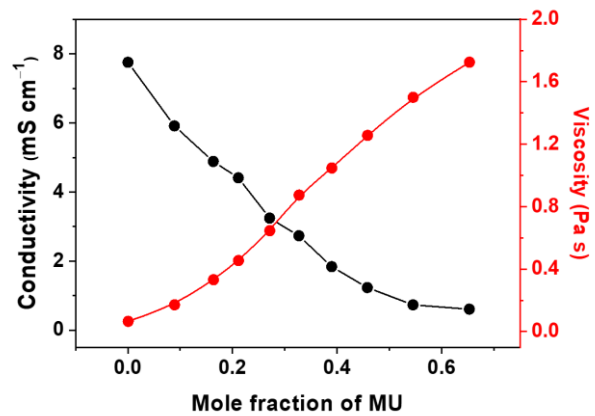
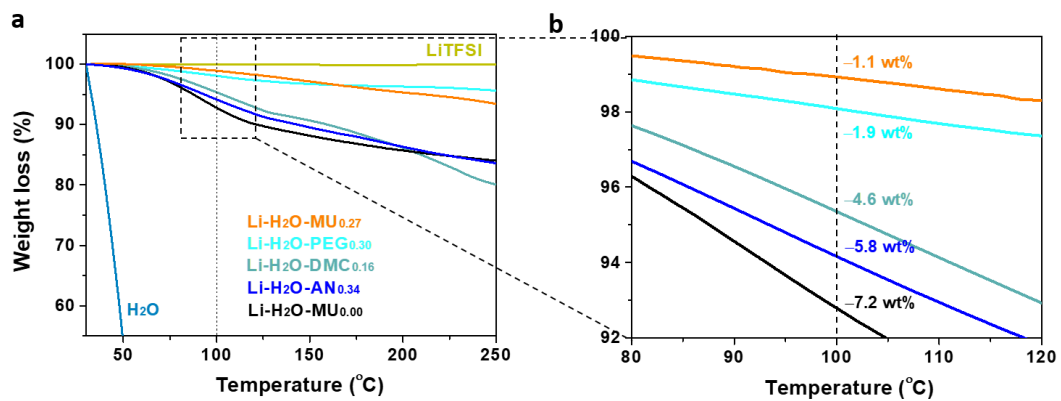
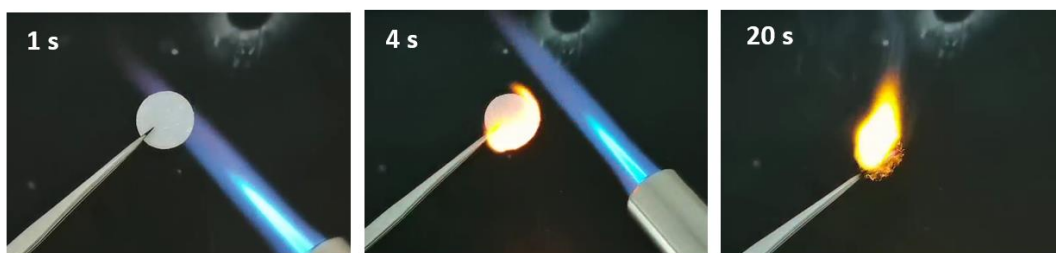


Figure S3. Ion conductivity and viscosity of as-prepared Li-H<sub>2</sub>O-MU electrolytes at 25 °C.



**Figure S4. Weight loss of various aqueous solutions in the thermogravimetric tests.**

Pristine LiTFSI salt and water are used for comparison.



**Figure S5. Flame tests of the Li-H<sub>2</sub>O-PEG<sub>0.30</sub> electrolyte.** The Li-H<sub>2</sub>O-PEG<sub>0.30</sub> electrolyte can be ignited by the propane-oxygen flame in 3 seconds. The SET was determined 42 s g<sup>-1</sup>.

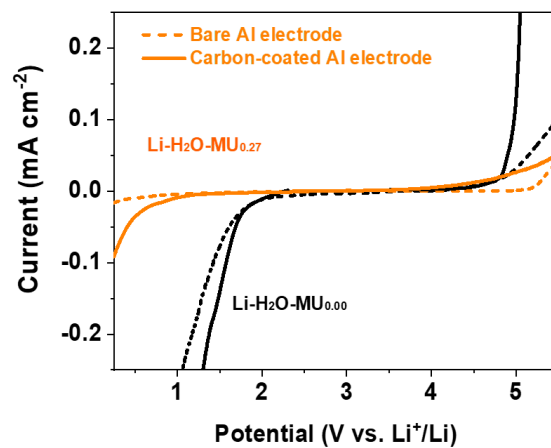


**Figure S6. Comparison of LSV results tested on the carbon-coated and bare Al electrodes.** The scan rate is 5 mV s<sup>-1</sup>.

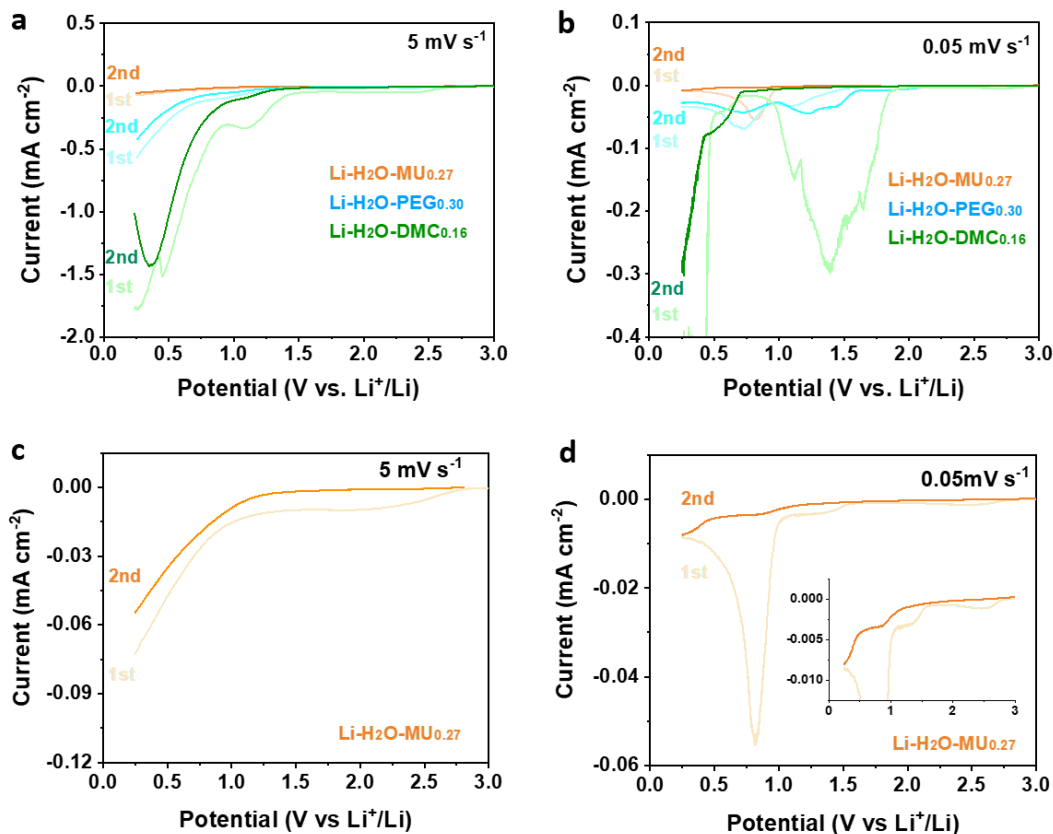


**Figure S7. Comparison of LSV curves on the carbon-coated Al electrodes in different scan rates.** (a, b), LSV curves for the electrolytes of Li-H<sub>2</sub>O-MU<sub>0.27</sub>, Li-H<sub>2</sub>O-PEG<sub>0.30</sub> and Li-H<sub>2</sub>O-DMC<sub>0.16</sub> at a high scan rate of 5 mV s<sup>-1</sup> (a) and a low scan rate of 0.05 mV s<sup>-1</sup> (b). An obvious difference is that the current density at the low scan rate is considerably lower than that at the high scan rate. This is because a lower scan rate leads to a longer time, and thus resulting in a lower current density ( $Q = I \cdot t$ ). (c, d) Magnified view of LSV curves for the Li-H<sub>2</sub>O-MU<sub>0.27</sub> electrolyte at a high scan rate of 5 mV s<sup>-1</sup> (c) and a low scan rate of 0.05 mV s<sup>-1</sup> (d). Clearly, the Li-H<sub>2</sub>O-MU<sub>0.27</sub> electrolyte can stabilize at 0.5 V vs. Li<sup>+</sup>/Li under both the testing conditions; the reduction current density is reduced at the second cathodic scan, suggesting the formation of SEI during the first cathodic scan. Because the reduction current density of the second cathodic scan at 0.05 mV s<sup>-1</sup> becomes almost one order lower than that at 5 mV s<sup>-1</sup>, the onset current densities for the electrochemical stable window should be different at different scan rates. In this work, 0.05 and 0.005 mA cm<sup>-2</sup> are set as the onset current densities for 5 and 0.05 mV s<sup>-1</sup>, respectively.

Besides the scan rate, the LSV current density is also significantly influenced by other factors, such as the surface area of the electrode and the distance between the work electrode and the counter electrode. The testing conditions are somewhat different in different labs, which causes some variance of the reported results. Nevertheless, it is meaningful to compare the LSV results under the identical testing condition. That's why we tested various electrolytes under the same condition in this work. We think this is the most reliable way to compare our core-shell-solvation electrolyte with other reported electrolytes.

Regarding SEI formation, the LSV curves of the first two cathodic scans provide useful information for evaluation. Figure S7c,d show the reduction current density is considerably reduced at the second cathodic scan, suggesting the formation of SEI during the first cathodic scan. There are two main reduction peaks in the first cathodic scan, i.e., a small reduction peak at ca. 2.5 V vs. Li<sup>+</sup>/Li followed by a larger reduction peak starting at ca. 1.8 V vs. Li<sup>+</sup>/Li. Combined with XPS and in-situ ATR-FTIR (see Figure 6), the first peak is likely resulted from the reduction of TFSI<sup>-</sup> anion, which contributes to the formation of an inorganic passivation film on the NbO<sub>2</sub> electrode; the second peak is likely resulted from the reduction of MU, which contributes to an extra organic passivation layer on the aforementioned inorganic film. Finally, an organic-inorganic hierarchical interphase on the anode is developed. For the electrolytes of Li-H<sub>2</sub>O-PEG<sub>0.30</sub> and Li-H<sub>2</sub>O-DMC<sub>0.16</sub>, large reduction currents can be found in both the first and the second cathodic scans, indicating that their passivation films are not sufficiently good to effectively suppress the electrolyte reduction at low potentials.



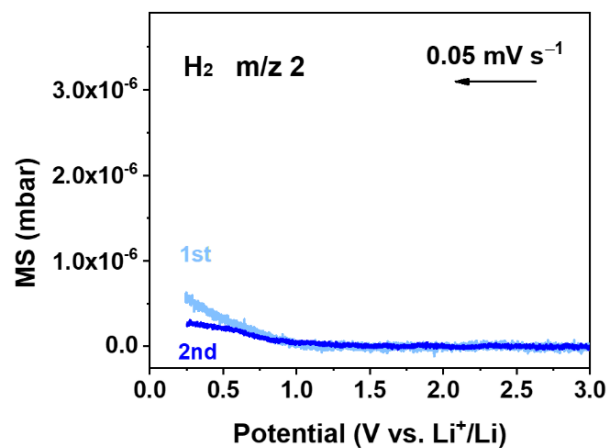


**Figure S8.** In-situ DEMS monitoring hydrogen evolution during the first two cathodic LSV scans in the Li-H<sub>2</sub>O-MU<sub>0.27</sub> solution. The scan rate is 0.05 mV s<sup>-1</sup>. The results evidence that hydrogen evolution reaction is effectively suppressed at the low potential of 0.5 V vs. Li<sup>+</sup>/Li, particularly for the second cathodic scan.

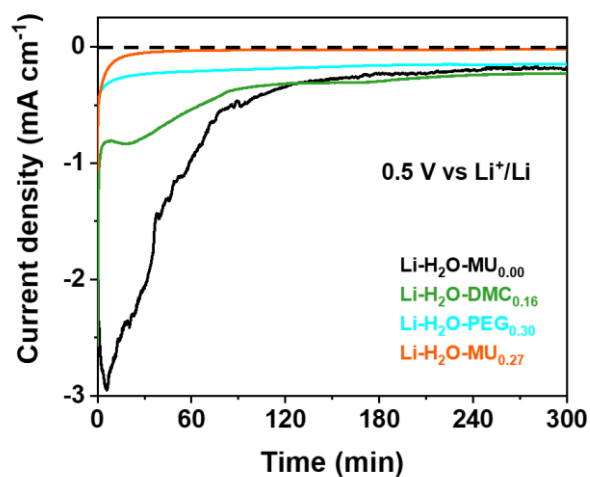


**Figure S9. Potentiostatic curves of various aqueous electrolytes on carbon-coated Al electrode.** Under 0.5 V vs.  $\text{Li}^+/\text{Li}$ , the reduction current decreases close to zero in 30 mins for the core-shell-solvation electrolyte of  $\text{Li-H}_2\text{O-MU}_{0.27}$ , indicating hydrogen evolution reaction has been effectively suppressed. In contrast, a significant reduction current remains even after 300 mins' test for the other aqueous electrolytes, indicating they are not stable at 0.5 V vs.  $\text{Li}^+/\text{Li}$ .

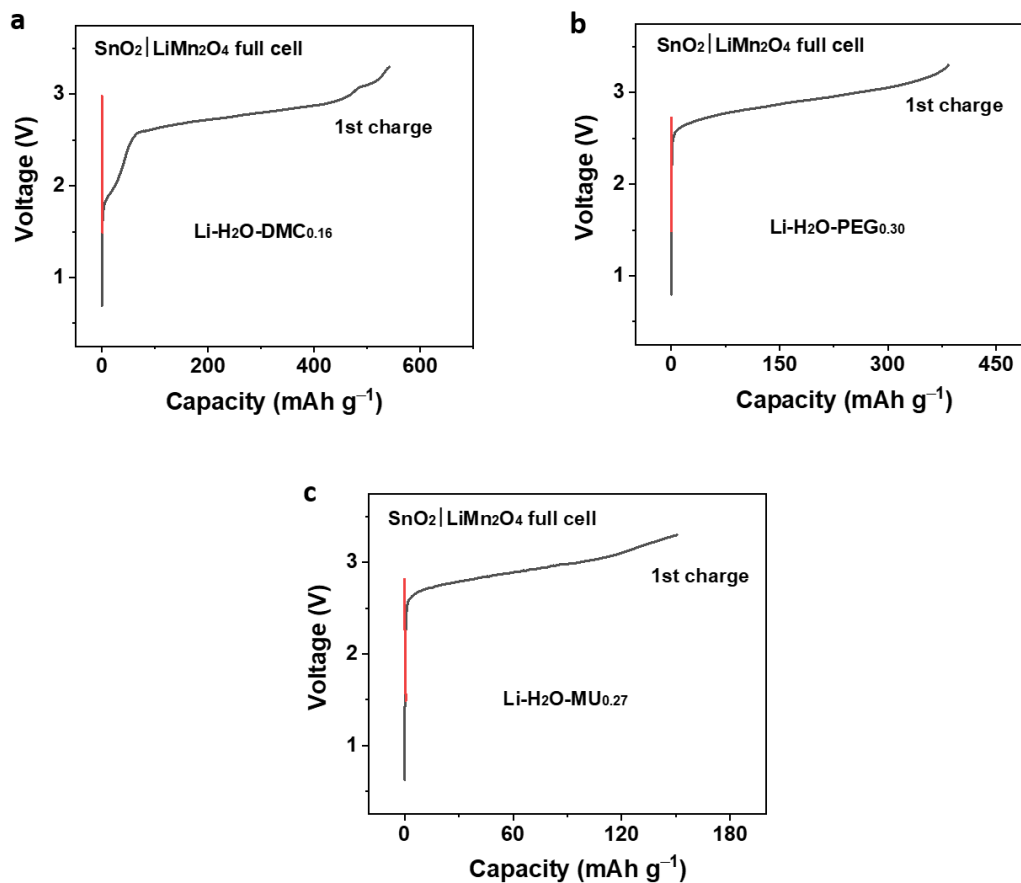


**Figure S10. Initial charge-discharge profile of the SnO<sub>2</sub>|LiMn<sub>2</sub>O<sub>4</sub> full cell using different electrolytes. a) Li-H<sub>2</sub>O-DMC<sub>0.16</sub>; b) Li-H<sub>2</sub>O-PEG<sub>0.30</sub>; c) Li-H<sub>2</sub>O-MU<sub>0.27</sub>.** Both SnO<sub>2</sub> and LiMn<sub>2</sub>O<sub>4</sub> contain no surface coating. The charge-discharge current density is 200 mA g<sup>-1</sup> on the weight basis of the SnO<sub>2</sub> electrode. Charge was conducted at 25 °C with a cutoff voltage of 3.3 V, corresponding to a reduction potential of 1.0 V vs Li<sup>+</sup>/Li for the SnO<sub>2</sub> anode. For all the tested aqueous electrolytes, no discharge capacity was obtained, showing the difficulty of operating a conversion-type anode in the aqueous electrolytes.

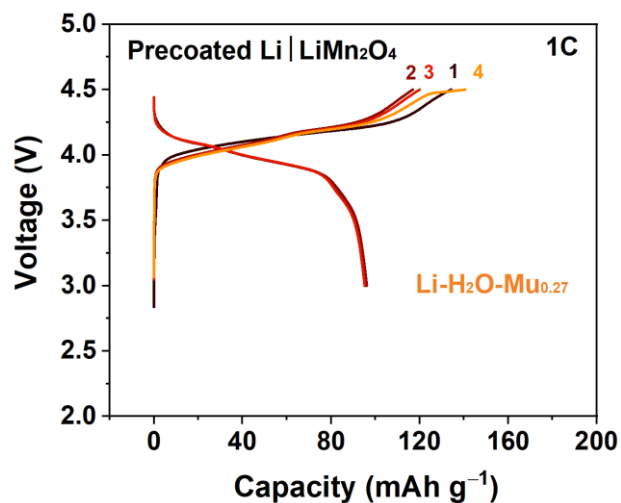


**Figure S11. Charge-discharge profiles of a pre-coated Li|LiMn<sub>2</sub>O<sub>4</sub> cell using the Li-H<sub>2</sub>O-MU<sub>0.27</sub> electrolyte.** The Li metal foil was pre-coated by a polymer electrolyte of LiTFSI/12PEO with the help of THF solvent. After drying in the glovebox, the pre-coated Li metal foil was moved into the ambient atmosphere for cell assembling. Charge and discharge were conducted at 25 °C with a cutoff voltage of 2.8~4.5 V. A 1C rate corresponds to 120 mA g<sup>-1</sup> on the weight basis of the LiMn<sub>2</sub>O<sub>4</sub> electrode.

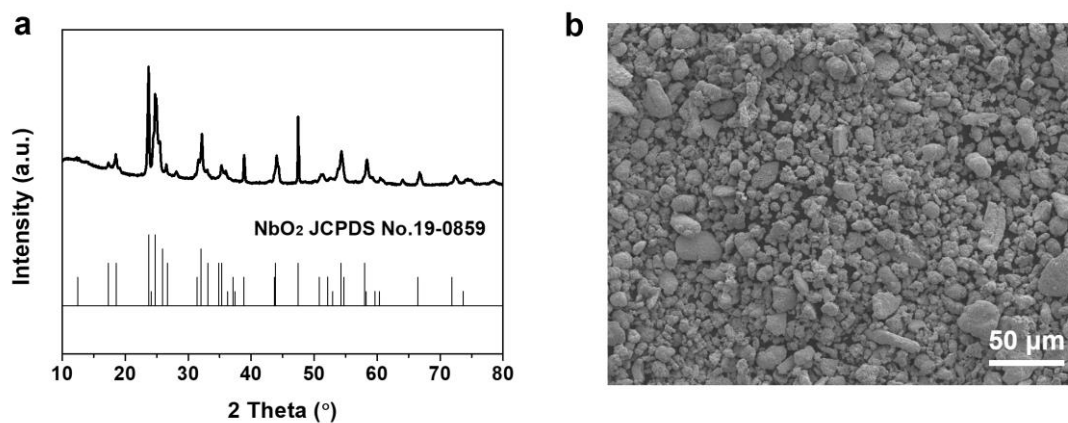


**Figure S12. Structural characterizations of home-made niobium oxide material.** XRD pattern (a) and SEM image (b) of the niobium oxide sample after calcination.

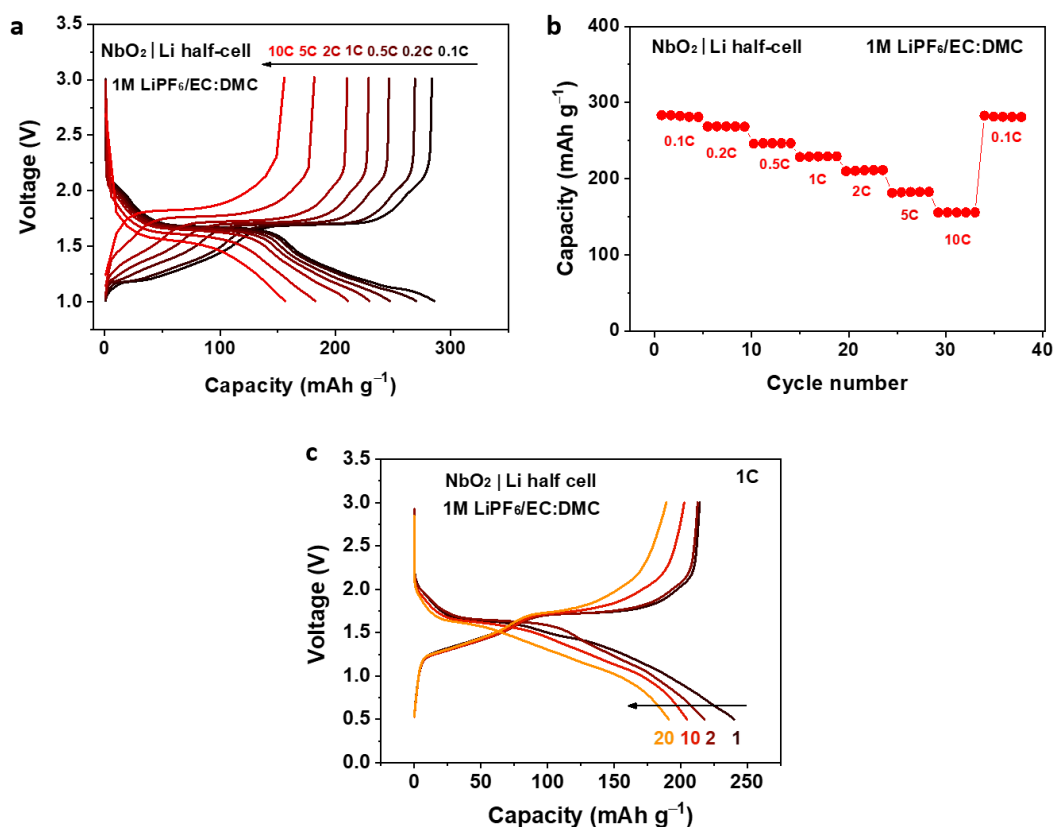


**Figure S13. Electrochemical performance of the NbO<sub>2</sub>|Li half-cell using a commercial organic electrolyte of 1M LiPF<sub>6</sub>/EC:DMC (1:1).** Charge-discharge voltage curves (a) and discharge capacities (b) at different rates with a cutoff voltage of 1.0~3.0 V. (c) Charge-discharge voltage curves at 1C rate with a cutoff voltage of 0.5~3.0 V. A significant capacity decay can be found when the cell discharges to 0.5 V, which may be associated with a structural change at the low potential. Thus, we conducted charge-discharge of the NbO<sub>2</sub> electrode in the aqueous electrolytes with a cutoff voltage of 1.0~3.0 V. All charge-discharge cycling tests were conducted at 25 °C. A 1C rate corresponds to 285 mA g<sup>-1</sup> on the weight basis of the NbO<sub>2</sub> electrode.

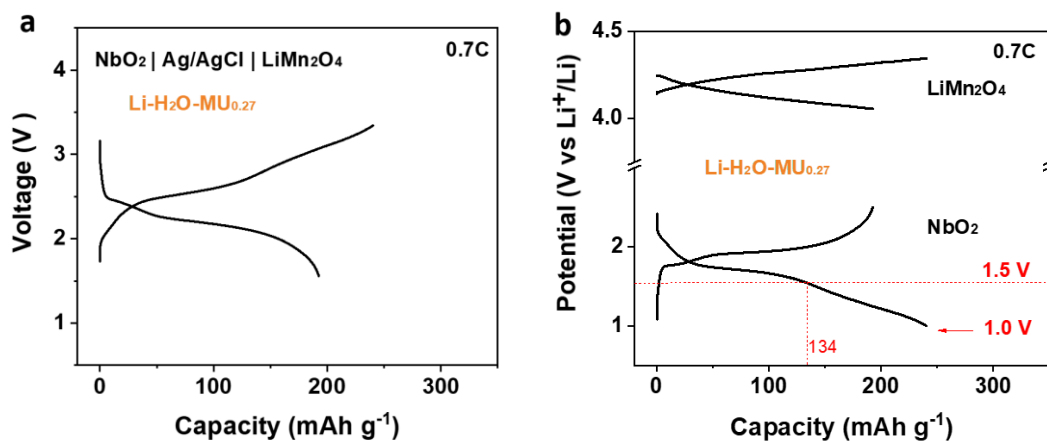


**Figure S14. Initial charge-discharge profiles for a three-electrode cell with a  $\text{NbO}_2$  anode, a  $\text{LiMn}_2\text{O}_4$  cathode and an  $\text{Ag/AgCl}$  reference electrode.** a) Charge-discharge profiles of the  $\text{LiMn}_2\text{O}_4$  cathode vs.  $\text{NbO}_2$  anode. b) Charge-discharge profiles of  $\text{LiMn}_2\text{O}_4$  cathode (vs.  $\text{Ag/AgCl}$ ) and  $\text{NbO}_2$  anode (vs.  $\text{Ag/AgCl}$ , in saturated KCl solution, 3.239 V vs.  $\text{Li}^+/\text{Li}$ ). Half capacity of the  $\text{NbO}_2$  anode came from the low potential region of 1.0 ~ 1.5 V vs.  $\text{Li}^+/\text{Li}$ . A 1C rate corresponds to 285  $\text{mA g}^{-1}$  on the weight basis of the  $\text{NbO}_2$  electrode.

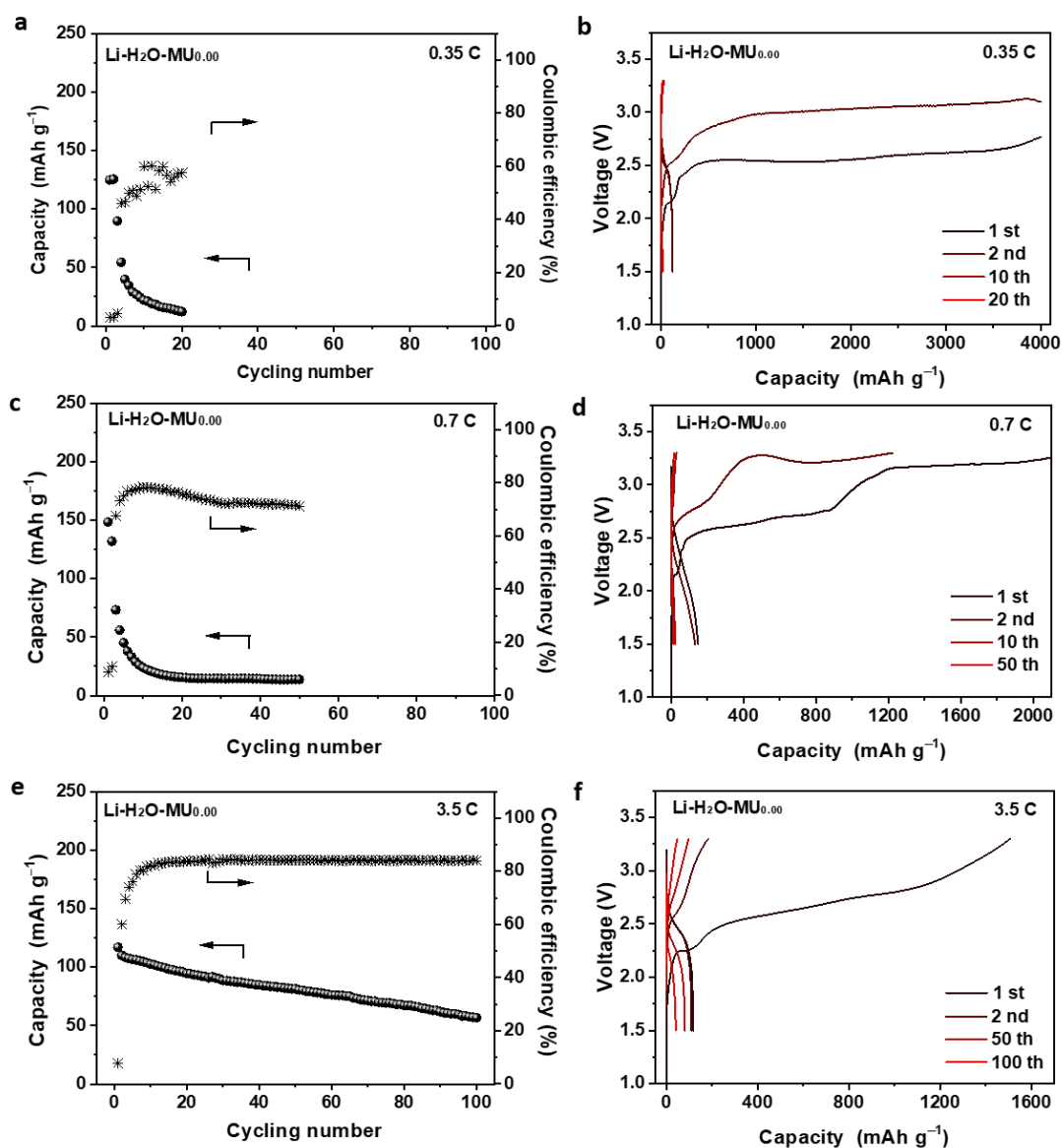


**Figure S15. Electrochemical performance of a NbO<sub>2</sub>|LiMn<sub>2</sub>O<sub>4</sub> full cell in the Li-H<sub>2</sub>O-MU<sub>0.00</sub> electrolyte.** Discharge capacity retention and coulombic efficiency of the NbO<sub>2</sub>|LiMn<sub>2</sub>O<sub>4</sub> full cell at different rates (**a**, **c**, **e**) and their corresponding charge-discharge curves (**b**, **d**, **f**). Charge and discharge were conducted at 25 °C with a cutoff voltage of 1.5~3.3 V and a maximum time of 40 hours in case the voltage cannot reach 3.3 V due to severe side reactions of hydrogen evolution. A 1C rate corresponds to 285 mA g<sup>-1</sup> on the weight basis of the NbO<sub>2</sub> electrode.



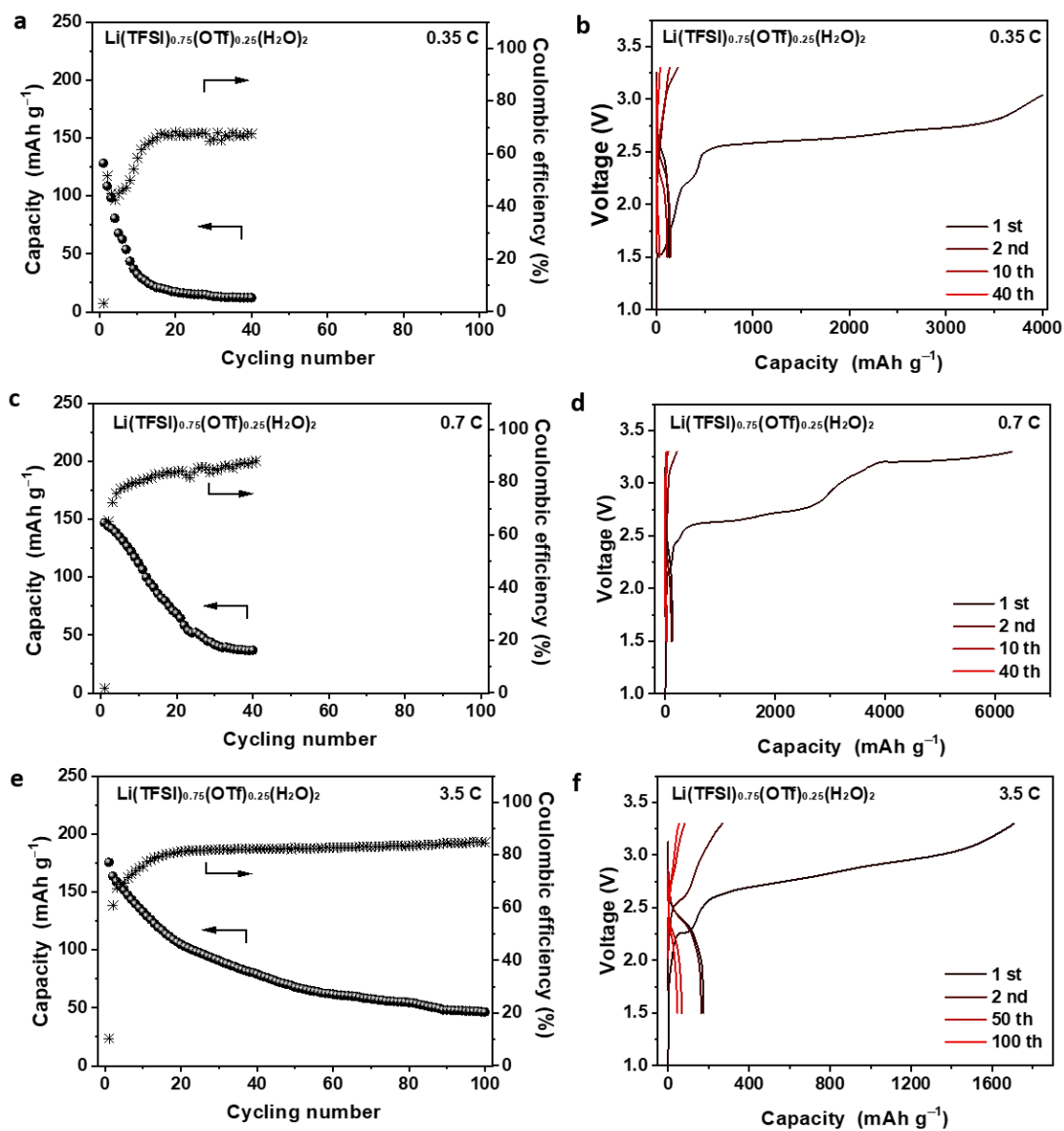


**Figure S16.** Electrochemical performance of a  $\text{NbO}_2|\text{LiMn}_2\text{O}_4$  full cell in bisalt-concentrated  $\text{Li}(\text{TFSI})_{0.75}(\text{OTf})_{0.25}(\text{H}_2\text{O})_2$  electrolyte. Discharge capacity retention and coulombic efficiency of the  $\text{NbO}_2|\text{LiMn}_2\text{O}_4$  full cell at different rates (**a**, **c**, **e**) and their corresponding charge-discharge curves (**b**, **d**, **f**). Charge and discharge were conducted at 25 °C with a cutoff voltage of 1.5~3.3 V and a maximum time of 40 hours in case the voltage cannot reach 3.3 V due to severe side reactions of hydrogen evolution. A 1C rate corresponds to 285  $\text{mA g}^{-1}$  on the weight basis of the  $\text{NbO}_2$  electrode.

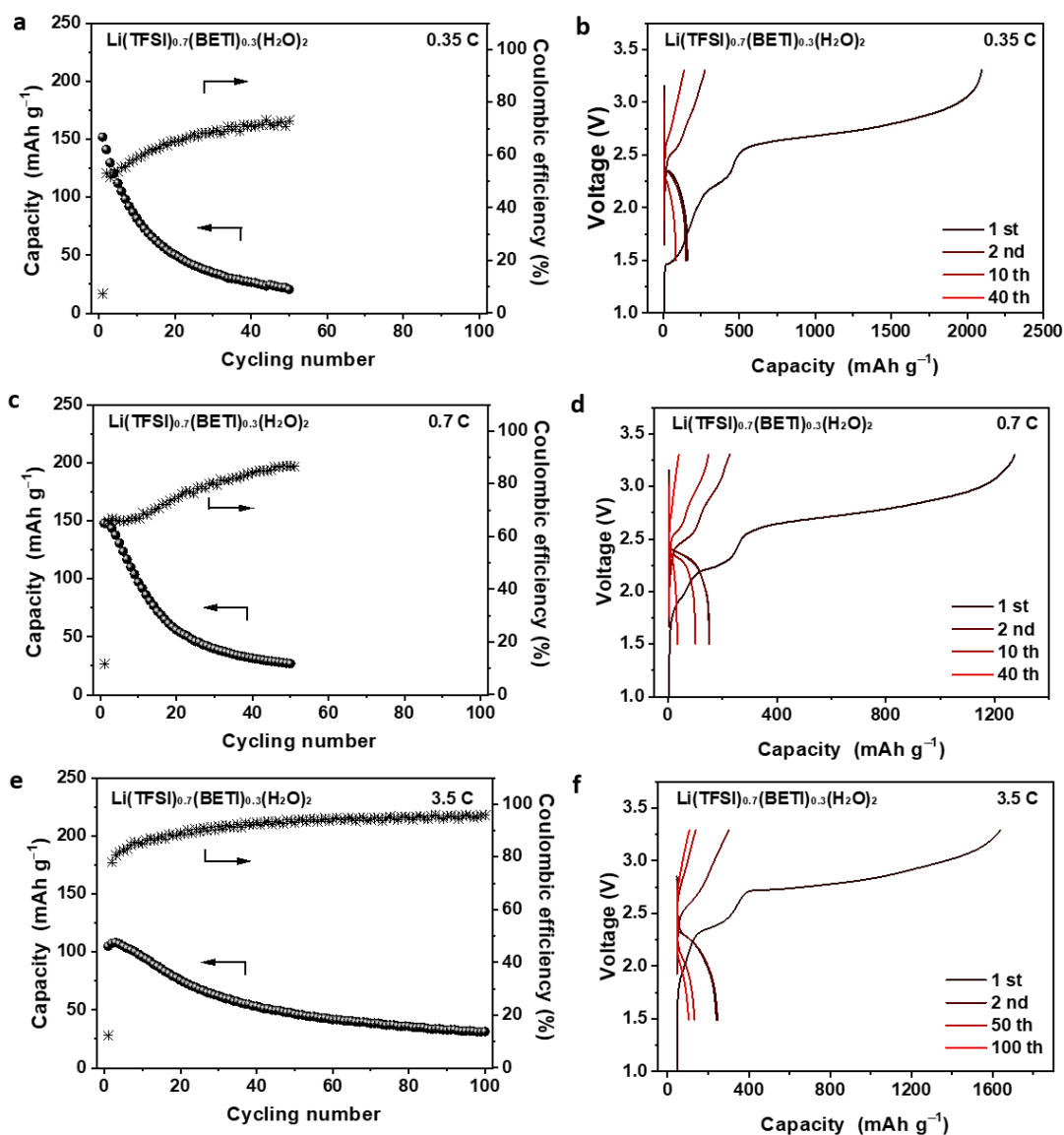


**Figure S17.** Electrochemical performance of a  $\text{NbO}_2|\text{LiMn}_2\text{O}_4$  full cell in bisalt-concentrated  $\text{Li}(\text{TFSI})_{0.7}(\text{BETI})_{0.3}(\text{H}_2\text{O})_2$  electrolyte. Discharge capacity retention and coulombic efficiency of the  $\text{NbO}_2|\text{LiMn}_2\text{O}_4$  full cell at different rates (a, c, e) and their corresponding charge-discharge curves (b, d, f). Charge and discharge were conducted at 25 °C with a cutoff voltage of 1.5~3.3 V and a maximum time of 40 hours in case the voltage cannot reach 3.3 V due to severe side reactions of hydrogen evolution. A 1C rate corresponds to 285  $\text{mA g}^{-1}$  on the weight basis of the  $\text{NbO}_2$  electrode.

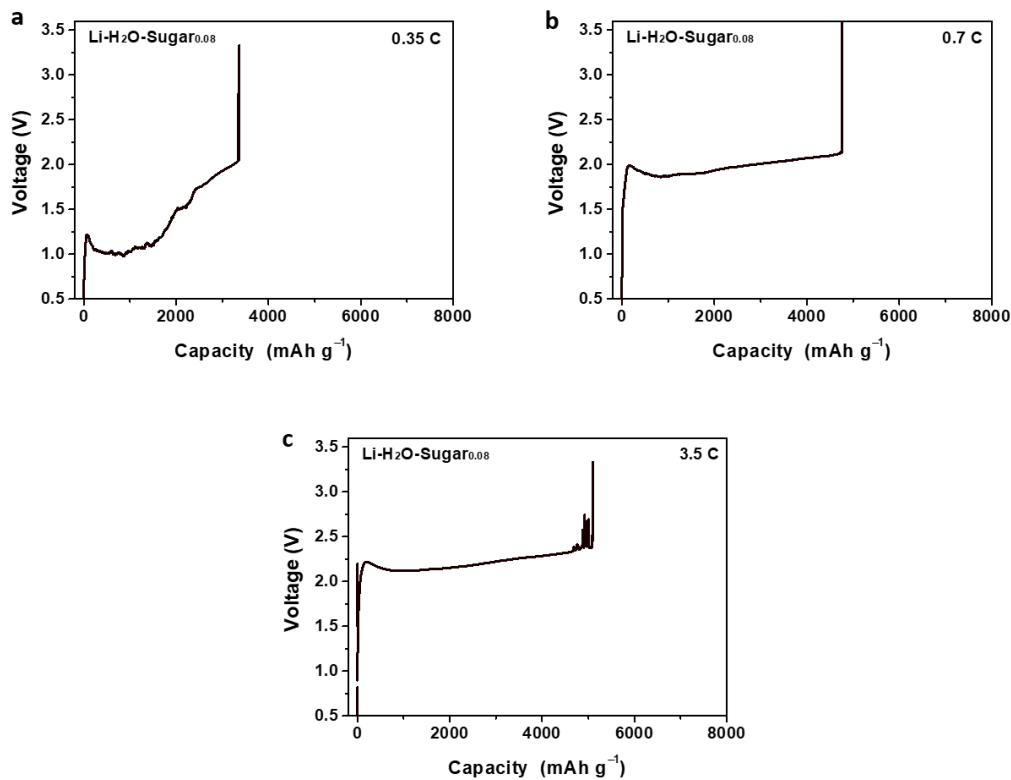


**Figure S18. Charge curves of a  $\text{NbO}_2|\text{LiMn}_2\text{O}_4$  full cell at various rates in the  $\text{Li-H}_2\text{O-Sugar}_{0.08}$  electrolyte.** Charge and discharge were conducted at 25 °C with a cutoff voltage of 1.5–3.3 V and a maximum time of 40 hours in case the voltage cannot reach 3.3 V due to severe side reactions of hydrogen evolution. A 1C rate corresponds to  $285 \text{ mA g}^{-1}$  on the weight basis of the  $\text{NbO}_2$  electrode. All the coin cells burst during the initial charge process at both low and high rates due to the overpressure caused by too much gas generation.

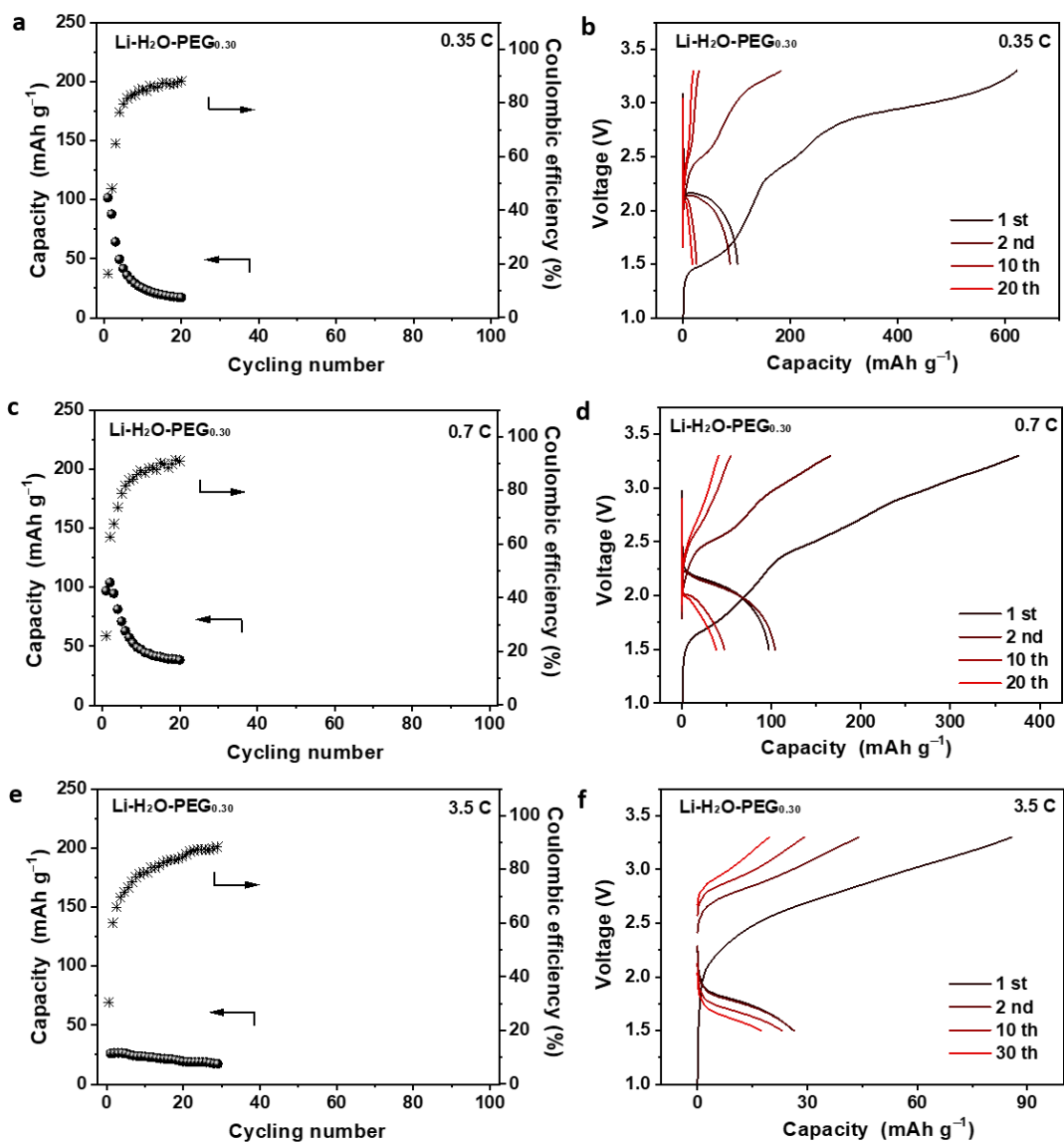


**Figure S19. Electrochemical performance of a NbO<sub>2</sub>|LiMn<sub>2</sub>O<sub>4</sub> full cell in Li-H<sub>2</sub>O-PEG<sub>0.30</sub> electrolyte.** Discharge capacity retention and coulombic efficiency of the NbO<sub>2</sub>|LiMn<sub>2</sub>O<sub>4</sub> full cell at different rates (**a**, **c**, **e**) and their corresponding charge-discharge curves (**b**, **d**, **f**). Charge and discharge were conducted at 25 °C with a cutoff voltage of 1.5~3.3 V and a maximum time of 40 hours in case the voltage cannot reach 3.3 V due to severe side reactions of hydrogen evolution. A 1C rate corresponds to 285 mA g<sup>-1</sup> on the weight basis of the NbO<sub>2</sub> electrode.

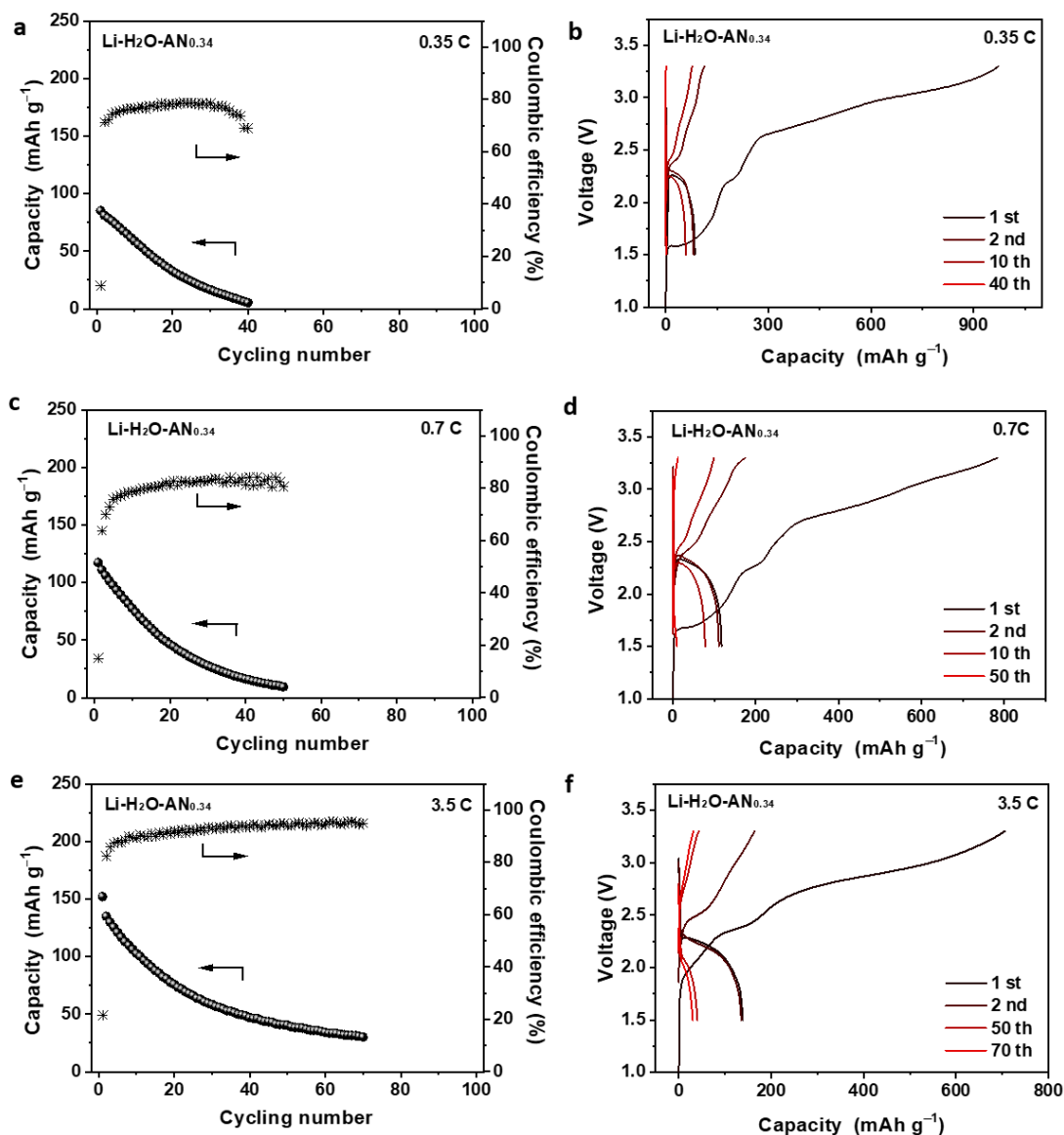


**Figure S20. Electrochemical performance of a  $\text{NbO}_2|\text{LiMn}_2\text{O}_4$  full cell in  $\text{Li-H}_2\text{O-AN}_{0.34}$  electrolyte.** Discharge capacity retention and coulombic efficiency of the  $\text{NbO}_2|\text{LiMn}_2\text{O}_4$  full cell at different rates (**a, c, e**) and their corresponding charge-discharge curves (**b, d, f**). Charge and discharge were conducted at 25 °C with a cutoff voltage of 1.5~3.3 V and a maximum time of 40 hours in case the voltage cannot reach 3.3 V due to severe side reactions of hydrogen evolution. A 1C rate corresponds to 285  $\text{mA g}^{-1}$  on the weight basis of the  $\text{NbO}_2$  electrode.

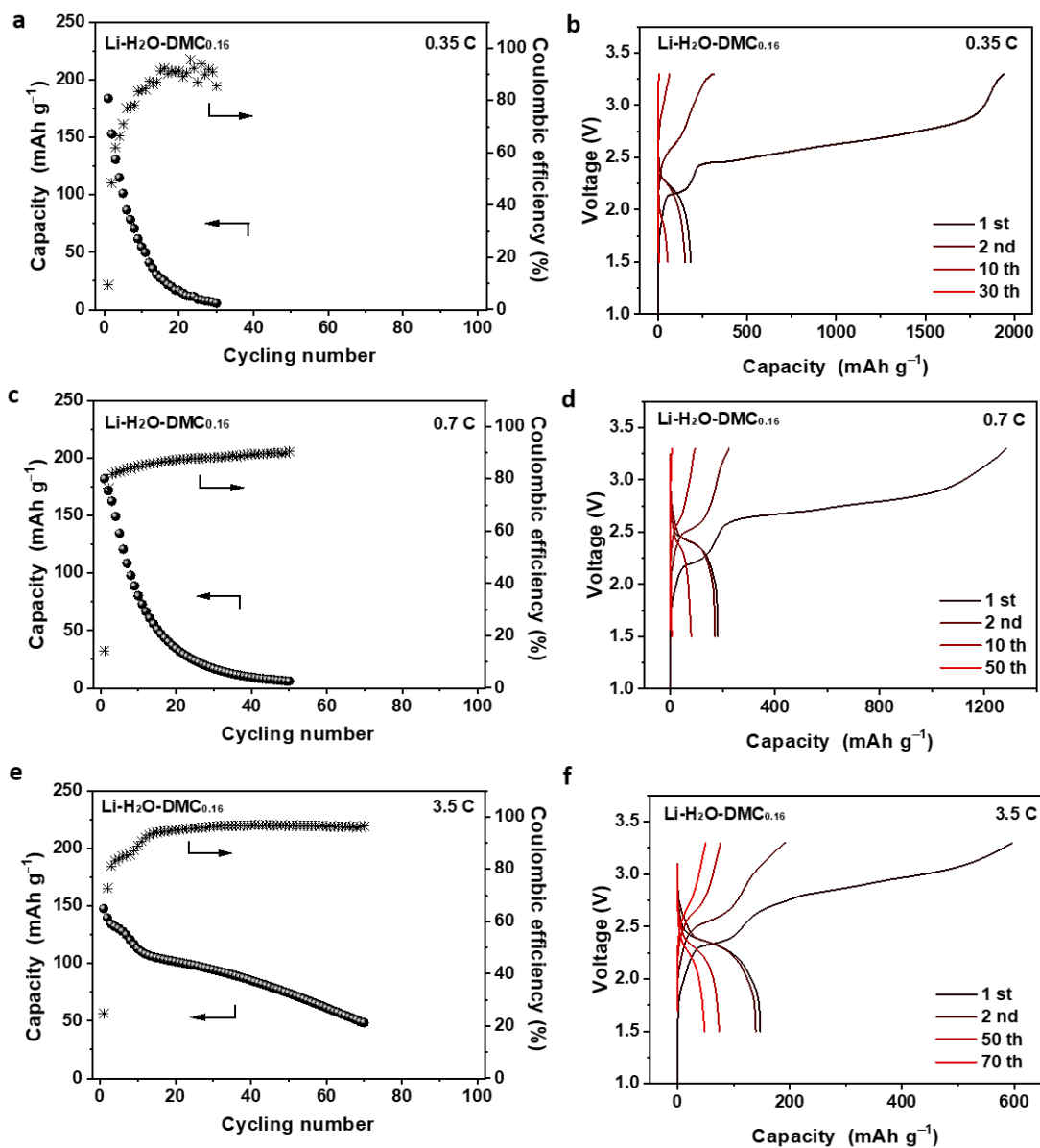


**Figure S21. Electrochemical performance of a  $\text{NbO}_2|\text{LiMn}_2\text{O}_4$  full cell in  $\text{Li-H}_2\text{O-DMC}_{0.16}$  electrolyte.** Discharge capacity retention and coulombic efficiency of the  $\text{NbO}_2|\text{LiMn}_2\text{O}_4$  full cell at different rates (a, c, e) and their corresponding charge-discharge curves (b, d, f). Charge and discharge were conducted at 25 °C with a cutoff voltage of 1.5~3.3 V and a maximum time of 40 hours in case the voltage cannot reach 3.3 V due to severe side reactions of hydrogen evolution. A 1C rate corresponds to 285  $\text{mA g}^{-1}$  on the weight basis of the  $\text{NbO}_2$  electrode.

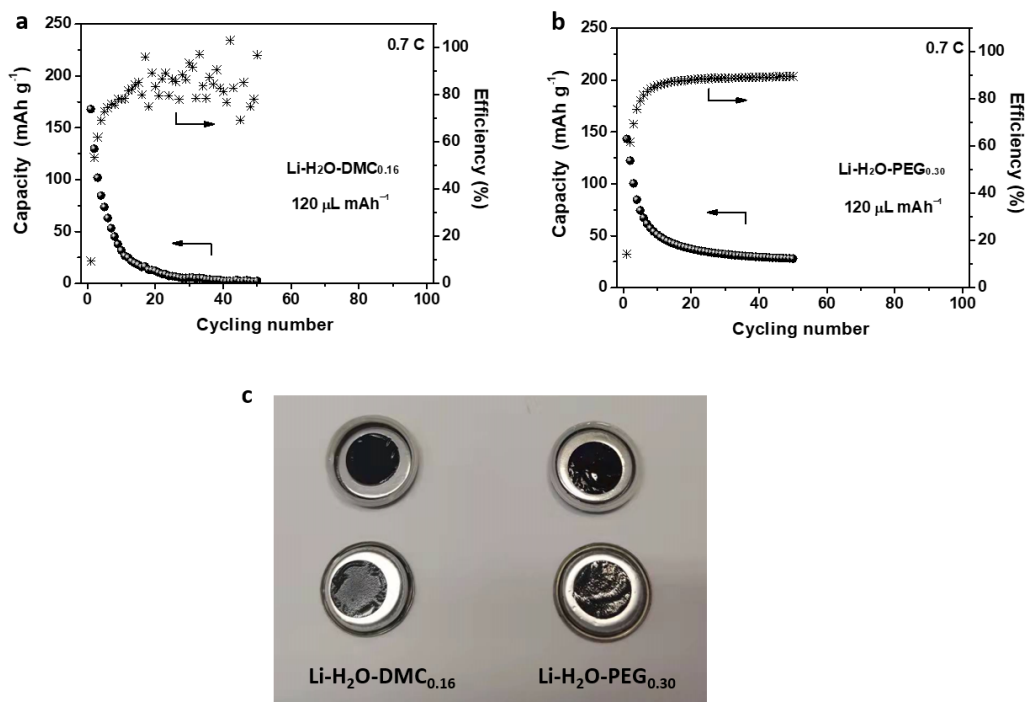


**Figure S22. Electrochemical performance of NbO<sub>2</sub>|LiMn<sub>2</sub>O<sub>4</sub> full cells using a high loading of electrolytes. (a) Capacity retention and columbic efficiency of the cell using the Li-H<sub>2</sub>O-DMC<sub>0.16</sub> electrolyte. (b) Capacity retention and columbic efficiency of the cell using the Li-H<sub>2</sub>O-PEG<sub>0.30</sub> electrolyte. (c) Images of disassembled cells after cycling. With a high loading of electrolytes (120 μL mAh<sup>-1</sup>), the cells still suffered from a fast decay; after cycling, much electrolyte was left in the cells. Thus, it can be concluded that the failure of these cells is not due to the lack of electrolyte but rather likely the consumption of limited active lithium resources caused by continuous side reactions and/or poor passivation interphases.**

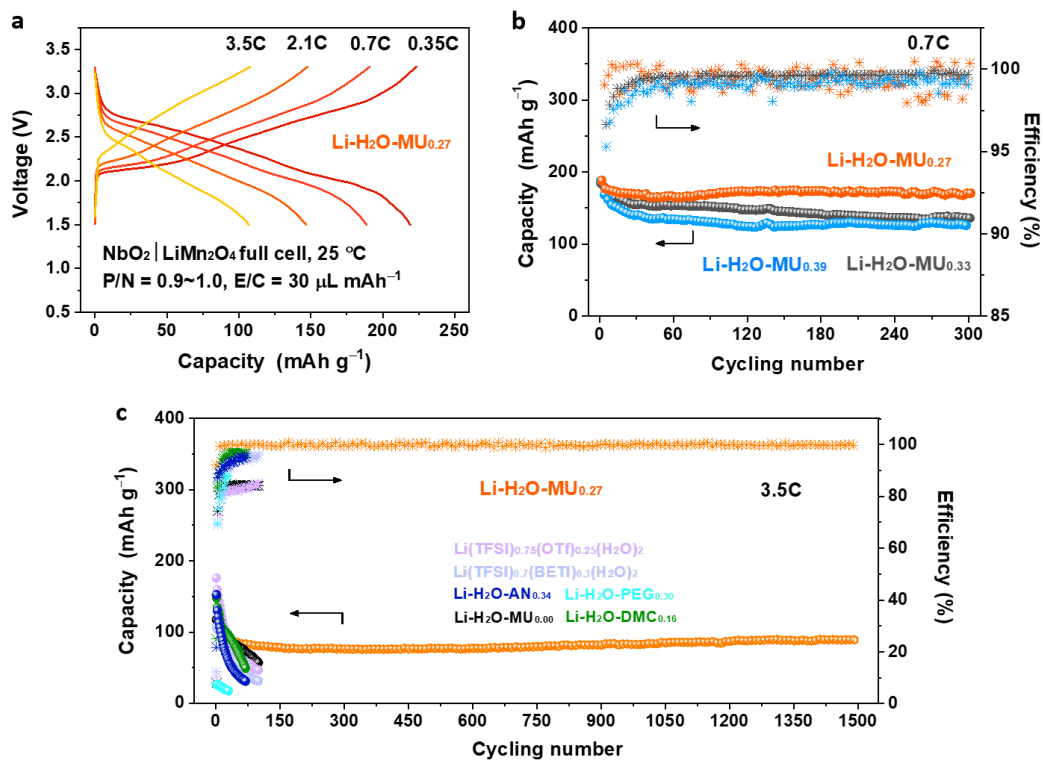


**Figure S23. Electrochemical performance of  $\text{NbO}_2|\text{LiMn}_2\text{O}_4$  cells in the as-prepared MU-assisted electrolytes and various reported aqueous electrolytes. (a) Typical charge-discharge curves for the  $\text{NbO}_2|\text{LiMn}_2\text{O}_4$  battery using the  $\text{Li-H}_2\text{O-MU}_{0.27}$  electrolyte at different current rates (0.35~3.5C). (b) Comparison of cycling stability of the  $\text{NbO}_2|\text{LiMn}_2\text{O}_4$  battery using the MU-assisted electrolytes with different contents of MU. (c) Comparison of cycling stability of the  $\text{NbO}_2|\text{LiMn}_2\text{O}_4$  battery using the  $\text{Li-H}_2\text{O-MU}_{0.27}$  electrolyte with those using various reported aqueous electrolytes at a rate of 3.5C. Charge and discharge were conducted at 25 °C with a cutoff voltage of 1.5~3.3 V. A 1C rate corresponds to  $285 \text{ mA g}^{-1}$  on the weight basis of the  $\text{NbO}_2$  electrode.**



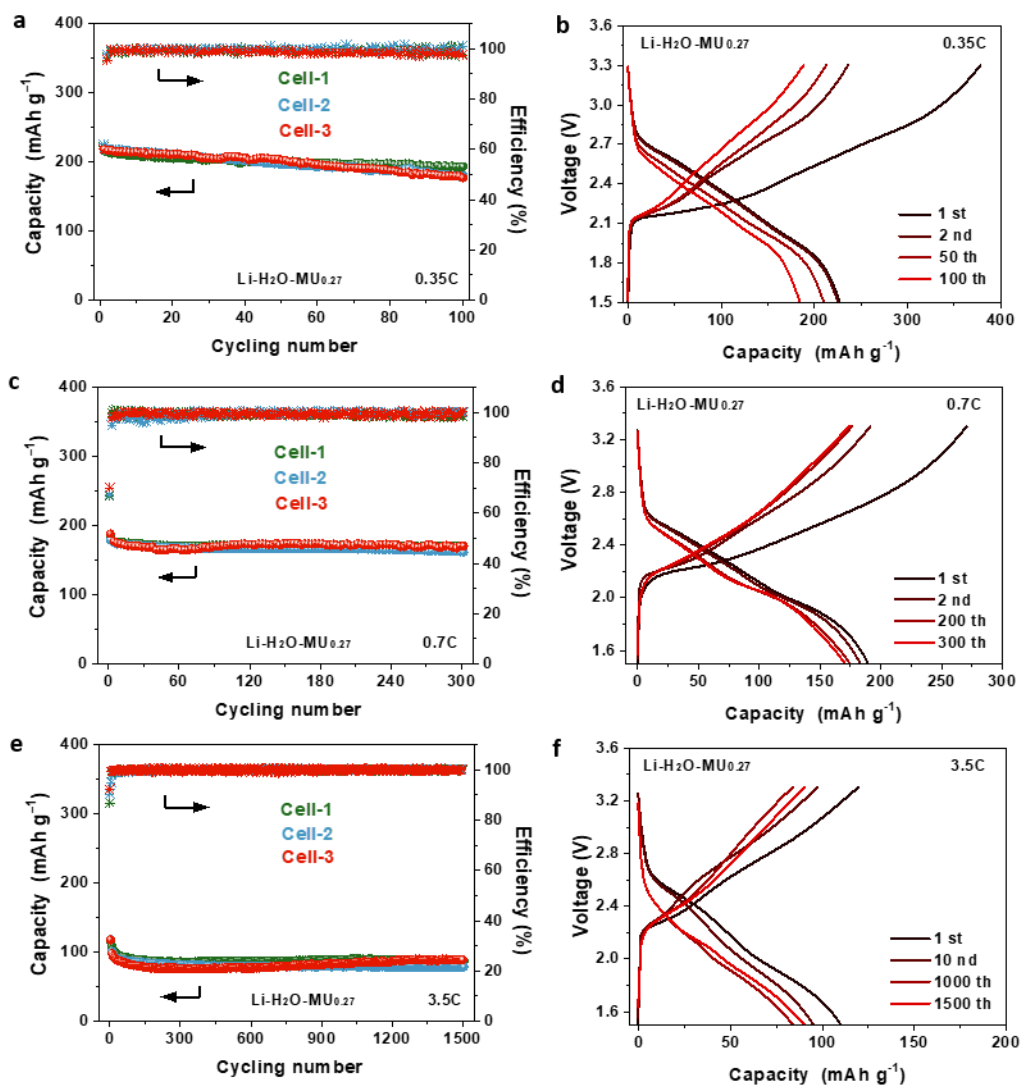


**Figure S24. Electrochemical performance of three duplicate  $\text{NbO}_2|\text{LiMn}_2\text{O}_4$  full cells in  $\text{Li-H}_2\text{O-MU}_{0.27}$  electrolyte.** Discharge capacity retention and coulombic efficiency of three duplicate  $\text{NbO}_2|\text{LiMn}_2\text{O}_4$  full cells at different rates (**a, c, e**) and charge-discharge curves of Cell-3 (**b, d, f**). Charge and discharge were conducted at 25 °C with a cutoff voltage of 1.5~3.3 V and a maximum time of 40 hours in case the voltage cannot reach 3.3 V due to severe side reactions of hydrogen evolution. A 1C rate corresponds to 285  $\text{mA g}^{-1}$  on the weight basis of the  $\text{NbO}_2$  electrode.

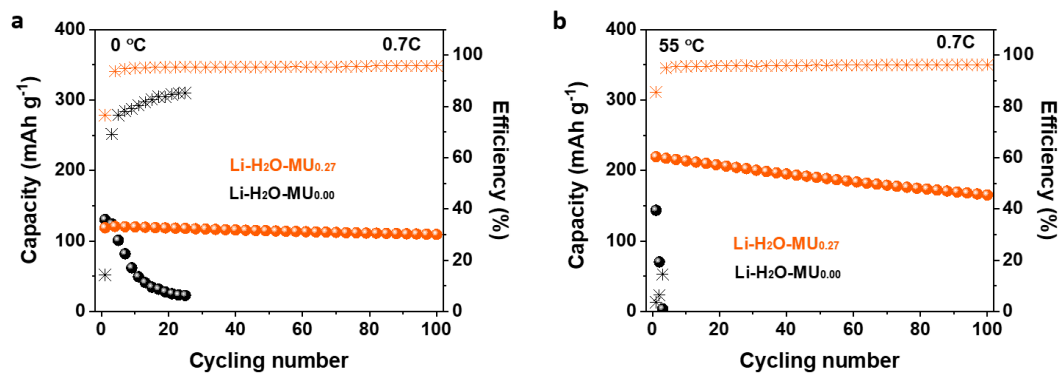


**Figure S25. Electrochemical performance of a  $\text{NbO}_2|\text{LiMn}_2\text{O}_4$  full cell at 0 and 55 °C.** For the  $\text{Li-H}_2\text{O-MU}_{0.27}$  electrolyte, the initial and average CEs, and the capacity retentions in 100 cycles at 0 °C are 76.6%, 95.2%, and 91.2%, respectively; those at 55 °C are 85.6%, 95.8%, and 75.5%, respectively. By contrast, the battery using the  $\text{Li-H}_2\text{O-MU}_{0.00}$  electrolyte quickly died in several cycles.

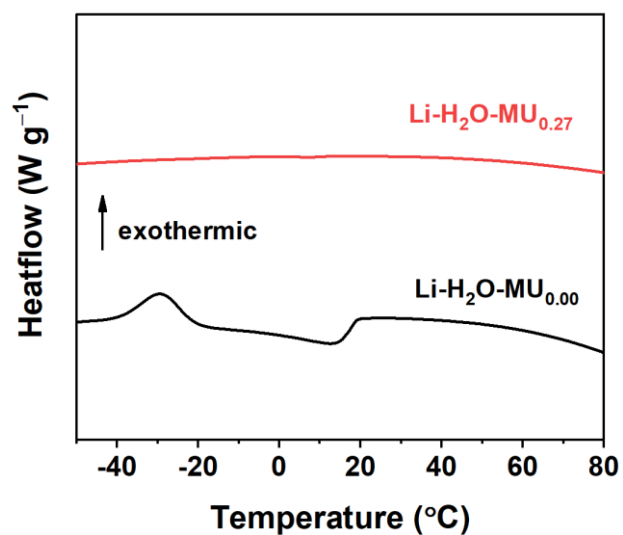


**Figure S26.** DSC curves of the solutions of Li-H<sub>2</sub>O-MU<sub>0.00</sub> and Li-H<sub>2</sub>O-MU<sub>0.27</sub>. The solution sample was loaded in an Al pan. The sample was firstly cooled to -50 °C and then heated to 80 °C at a heating rate of 5 °C min<sup>-1</sup>. The purge Ar flow is 50 ml min<sup>-1</sup>.

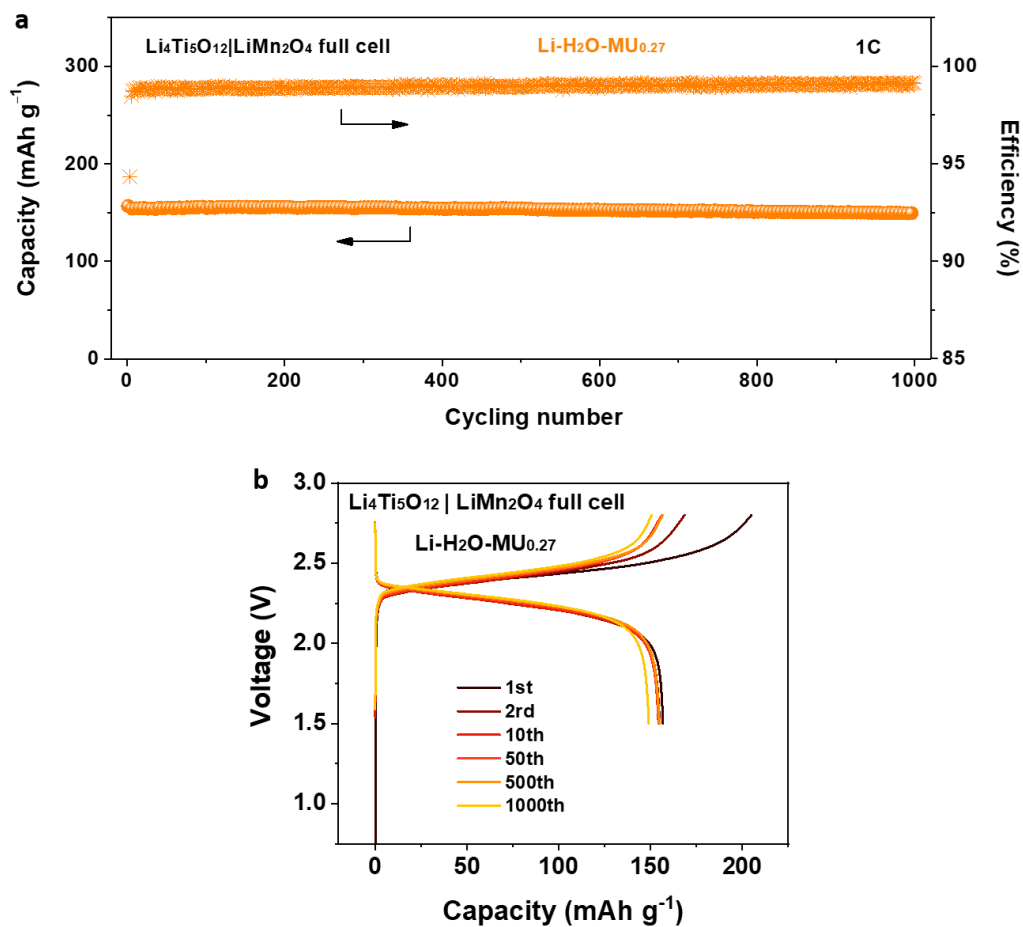


**Figure S27. Electrochemical performance of a  $\text{Li}_4\text{Ti}_5\text{O}_{12}|\text{LiMn}_2\text{O}_4$  full cell using the  $\text{Li-H}_2\text{O-MU}_{0.27}$  electrolyte.** a) Discharge capacity retention and coulombic efficiency at 1C rate. b) Selected charge-discharge curves. Charge and discharge were conducted at 25 °C with a cutoff voltage of 1.5~2.8 V. A 1C rate corresponds to 170  $\text{mA g}^{-1}$  on the weight basis of the  $\text{Li}_4\text{Ti}_5\text{O}_{12}$  electrode.

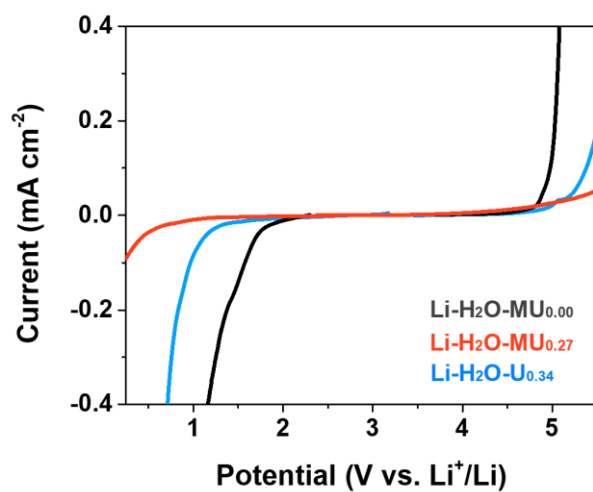


**Figure S28.** LSV curves of a carbon-coated Al electrode in the electrolyte of Li-H<sub>2</sub>O-U<sub>0.34</sub>.

The scan rate is 5 mV s<sup>-1</sup>.

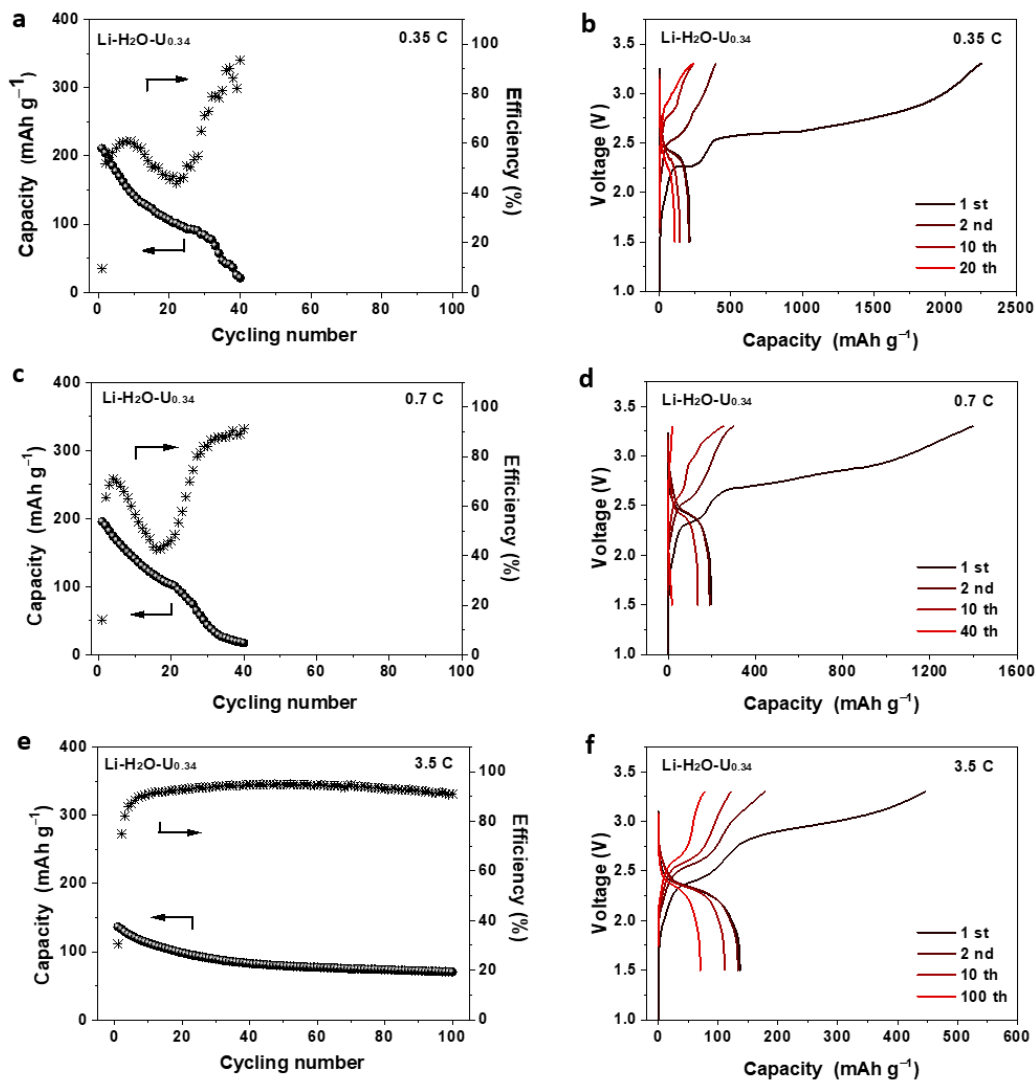


**Figure S29. Electrochemical performance of a  $\text{NbO}_2|\text{LiMn}_2\text{O}_4$  full cell in  $\text{Li-H}_2\text{O-U}_{0.34}$  electrolyte.** Discharge capacity retention and coulombic efficiency of the  $\text{NbO}_2|\text{LiMn}_2\text{O}_4$  full cell at different rates (**a**, **c**, **e**) and their corresponding charge-discharge curves (**b**, **d**, **f**). Charge and discharge were conducted at 25 °C with a cutoff voltage of 1.5 ~ 3.3 V and a maximum time of 40 hours in case the voltage cannot reach 3.3 V due to severe side reactions of hydrogen evolution. A 1C rate corresponds to 285  $\text{mA g}^{-1}$  on the weight basis of the  $\text{NbO}_2$  electrode.

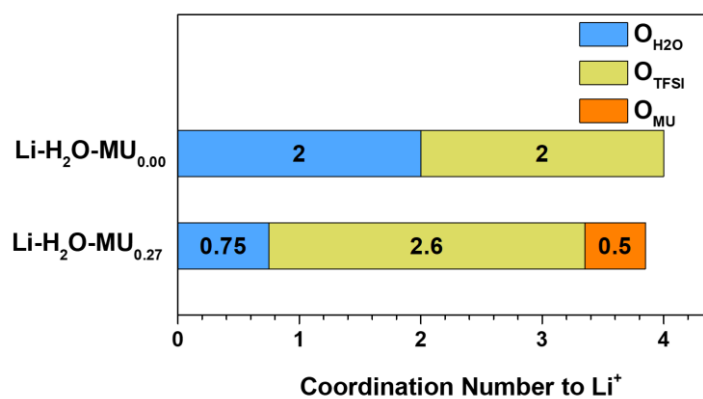


**Figure S30. Average coordination numbers of TFSI<sup>-</sup>, H<sub>2</sub>O and MU to Li<sup>+</sup>.** For the Li-H<sub>2</sub>O-MU<sub>0.00</sub> solution, a Li<sup>+</sup> has a typical fourfold coordination with H<sub>2</sub>O (2) and TFSI<sup>-</sup> (2). For the Li-H<sub>2</sub>O-MU<sub>0.27</sub> solution, the introduction of MU results in an increase of coordination number of TFSI (2.6) and a decrease of coordination number of H<sub>2</sub>O (0.75) to Li<sup>+</sup>, showing a dramatic change of local coordination environment in the solution.

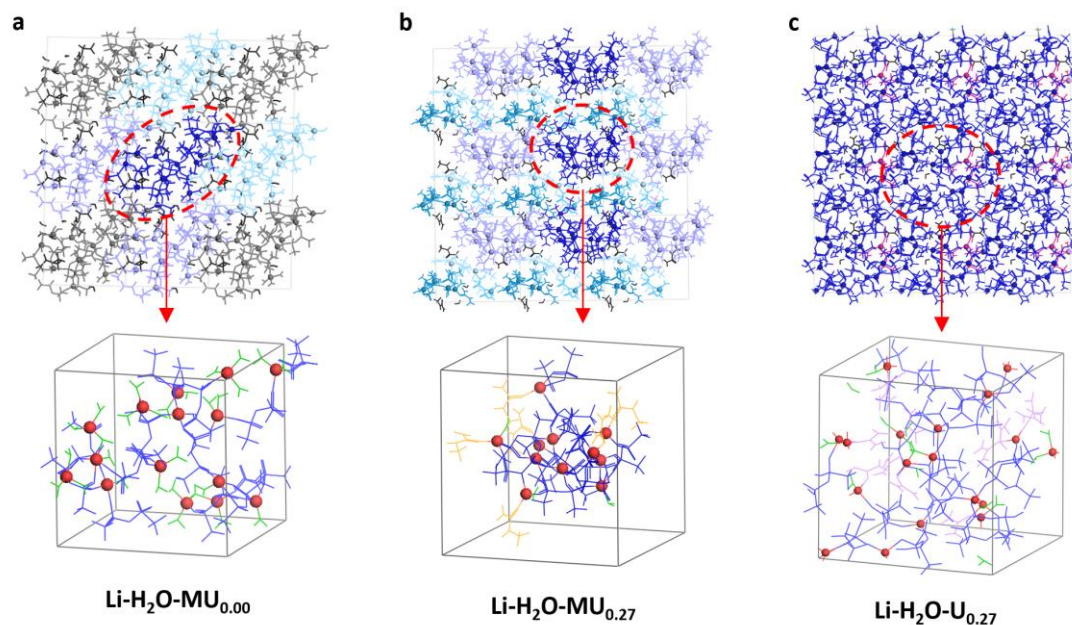


**Figure S31. Solution structures of Li-H<sub>2</sub>O-MU<sub>0.00</sub>, Li-H<sub>2</sub>O-MU<sub>0.27</sub> and Li-H<sub>2</sub>O-U<sub>0.27</sub> solutions from DFT-MD.** (a) For Li-H<sub>2</sub>O-MU<sub>0.00</sub>, a mass of H<sub>2</sub>O molecules coordinates with Li<sup>+</sup> thus reduce the number of free-state water. (b) The MU-assisted solution structure shows many agminated nanoscale clusters are distributed in the solution, indicating that the introduction of MU help to form these core-shell-like structure. (c) When asymmetric MU is replaced by symmetric U, the nanoclusters are no longer maintained and form a uniform dispersed structure.



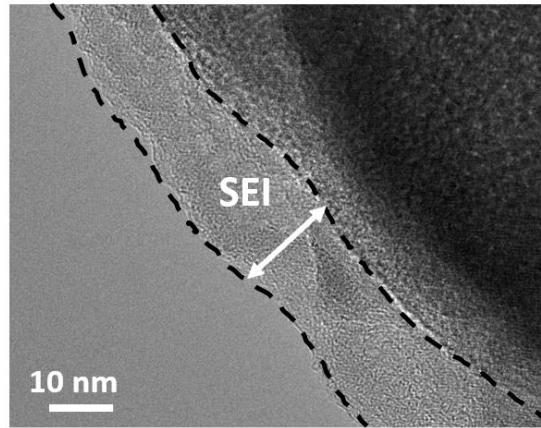
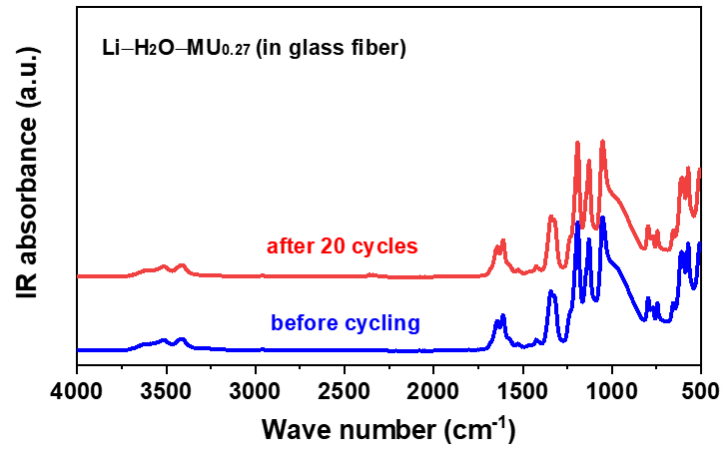
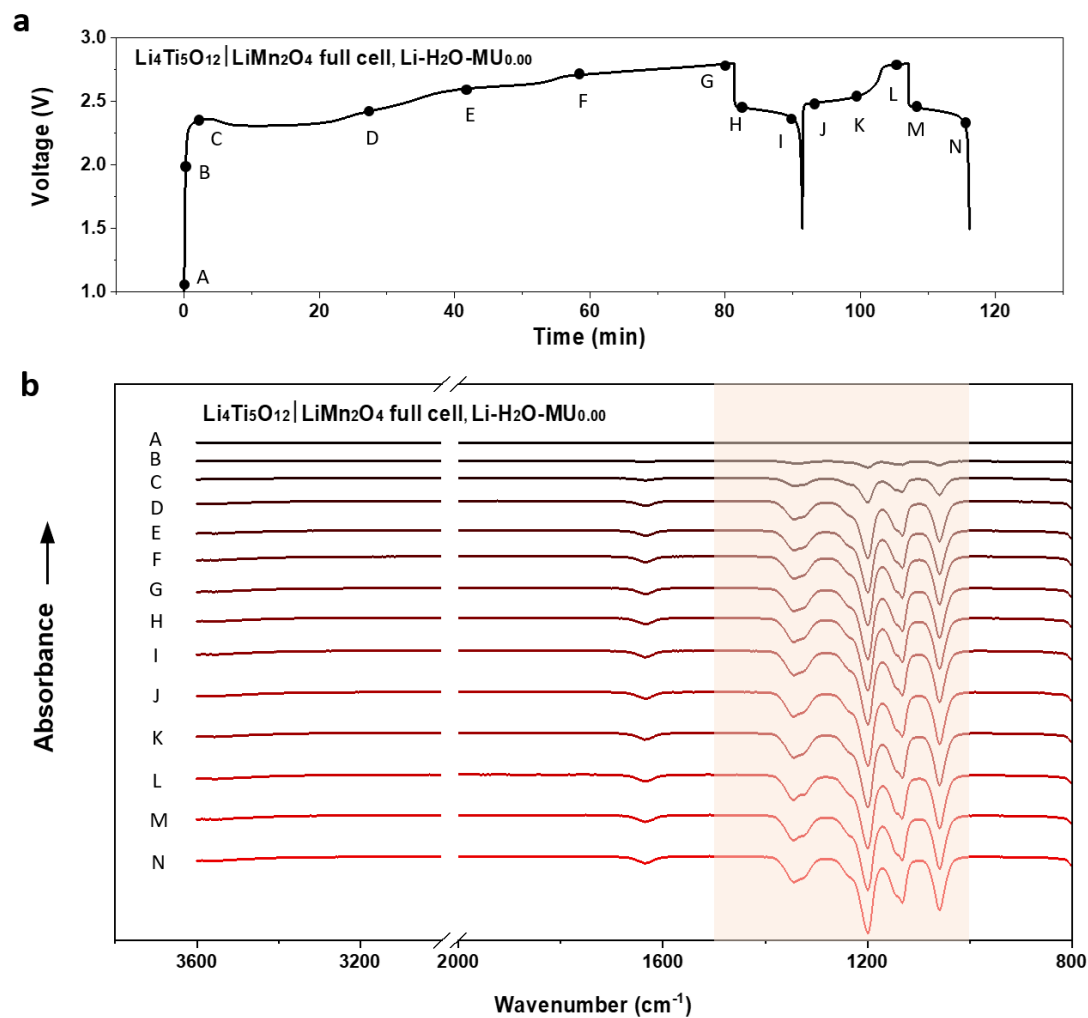


Figure S32 TEM image of the cycled NbO<sub>2</sub>.



**Figure S33. ATR-FTIR spectra of the Li-H<sub>2</sub>O-MU<sub>0.27</sub> electrolyte before and after cycling.** No significant difference can be found as compared to fresh Li-H<sub>2</sub>O-MU<sub>0.27</sub> electrolyte, suggesting a good SEI has formed on the electrodes in the first several cycles such that it did not consume significant electrolyte any more in the subsequent cycling.



**Figure S34. In-situ ATR-FTIR observation of SEI formation in a  $\text{Li}_4\text{Ti}_5\text{O}_{12}|\text{LiMn}_2\text{O}_4$  full cell using the  $\text{Li-H}_2\text{O-MU}_{0.00}$  during the initial two charge-discharge cycles.** When the battery was charged to 2.0 V, a counter-absorbance of IR signal at  $900\sim 1400\text{ cm}^{-1}$  can be observed, which is due to the compensation of electrolyte background caused by the formation of TFSI-derived inorganic SEI that adhered on the surface of ATR crystal. No other IR absorbance can be observed, which implies that the generated SEI on the  $\text{Li}_4\text{Ti}_5\text{O}_{12}$  anode is predominantly composed of inorganic substances with little organic components.

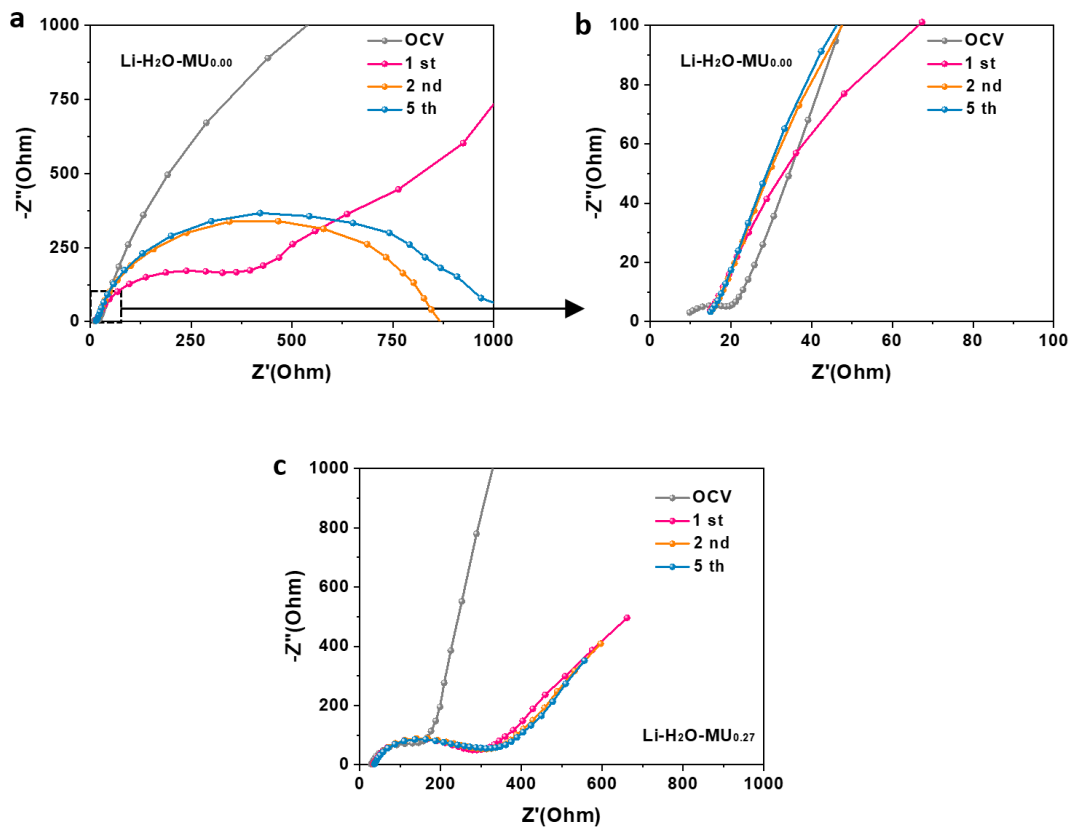


**Figure S35. Impedance spectra of the  $\text{NbO}_2|\text{LiMn}_2\text{O}_4$  full cells using the  $\text{Li-H}_2\text{O-MU}_{0.00}$  and  $\text{Li-H}_2\text{O-MU}_{0.27}$  electrolytes during the cycling. a) Impedance spectra of the  $\text{NbO}_2|\text{LiMn}_2\text{O}_4$  full cells using the  $\text{Li-H}_2\text{O-MU}_{0.00}$  electrolyte. b) Magnified view of the frame in a). c) Impedance spectra of the  $\text{NbO}_2|\text{LiMn}_2\text{O}_4$  full cells using the  $\text{Li-H}_2\text{O-MU}_{0.27}$  electrolyte.**

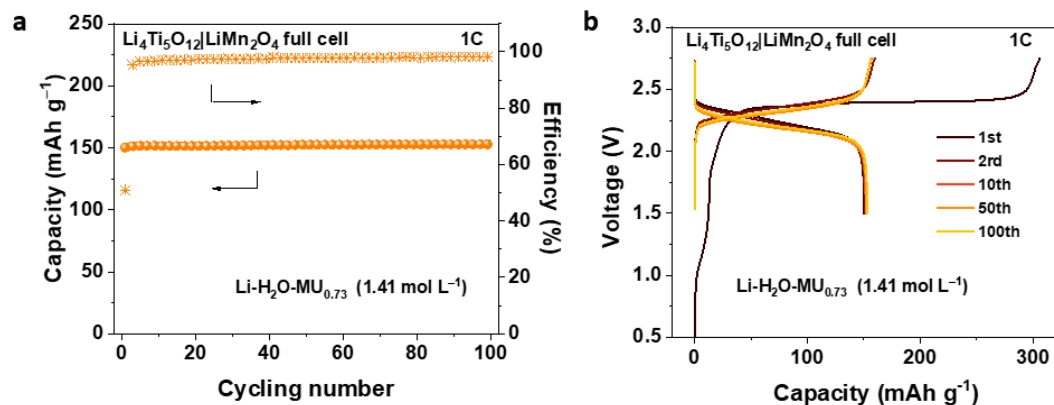


**Figure S36. A dilute  $\text{Li-H}_2\text{O-MU}_{0.73}$  electrolyte enables a stable operation of  $\text{Li}_4\text{Ti}_5\text{O}_{12}|\text{LiMn}_2\text{O}_4$  full cell. (a) Discharge capacity retention and coulombic efficiency at 1C rate. (b) Selected charge-discharge curves. The molar concentration of LiTFSI in the  $\text{Li-H}_2\text{O-MU}_{0.73}$  electrolyte is 1.41 mol L<sup>-1</sup>. Charge and discharge were conducted at 25 °C with a cutoff voltage of 1.5~2.75 V. A 1C rate corresponds to 170 mA g<sup>-1</sup> on the weight basis of the  $\text{Li}_4\text{Ti}_5\text{O}_{12}$  electrode.**

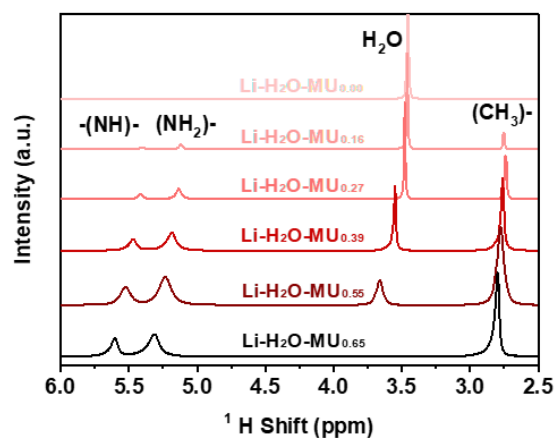


**Figure S37.**  $^1\text{H}$  NMR spectra of  $\text{Li-H}_2\text{O-MU}_x$ . The experiments were conducted on a Bruker Avance 500 MHz Solution NMR Spectrometer at room temperature.  $^1\text{H}$  signal of tetramethylsilane at 0 ppm was used as the reference.  $^1\text{H}$  signals of amide and methyl shift to low field with the increase of MU content, which is resulted from the deshielding effect owing to the increase content of electron-donating groups ( $-\text{NH}$ ,  $-\text{NH}_2$ ,  $-\text{CH}_3$ ).  $^1\text{H}$  signal of  $\text{H}_2\text{O}$  shifts to low field with reduced  $\text{H}_2\text{O}$  content, indicating an increase of their surrounding electronic density that is resulted from an overall interaction between  $\text{H}_2\text{O}$  with one or more species of  $\text{Li}^+$  cation,  $\text{TFSI}^-$  anion and MU molecules.

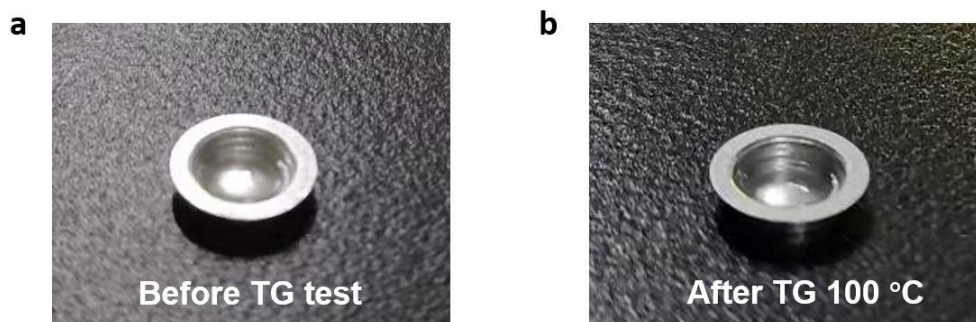


**Figure S38. Images of the  $\text{Li-H}_2\text{O-MU}_{0.27}$  sample in an Al pan. (a) Before TG measurement. (b) After TG measurements (heating to 100 °C and cooling down to room temperature). No precipitation of salt was found in the solution after the TG measurement.**

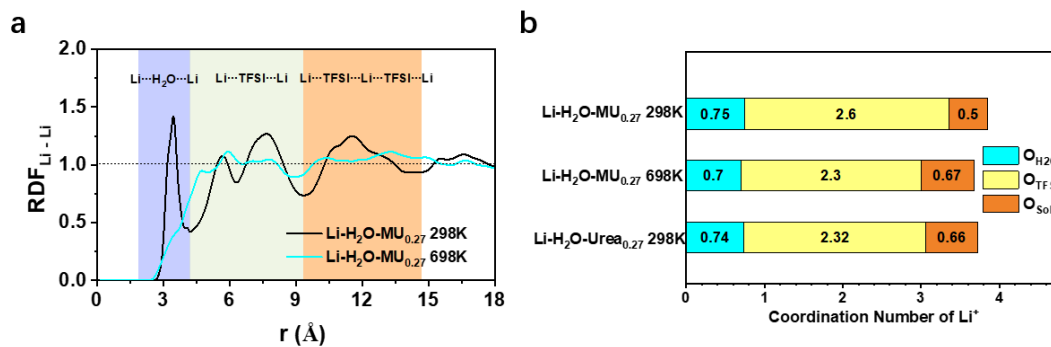


**Figure S39. Comparison of electrolyte structure of  $Li-H_2O-MU_{0.27}$  at 298 K and 698 K. (a)** Li-Li RDFs at 298 K and 698 K. The third peak of the Li-Li RDF at 298 K is an indicator of the Li-TFSI-Li-TFSI-Li network, while the RDF at 698 K does not have pronounced peaks. **(b)** Li-TFSI coordination number reduces from 2.6 at 298 K to 2.3 at 698 K. Interestingly, the Li-TFSI coordination number in  $Li-H_2O-U_{0.27}$  at 298 K is similar to that in  $Li-H_2O-MU_{0.27}$  698 K.



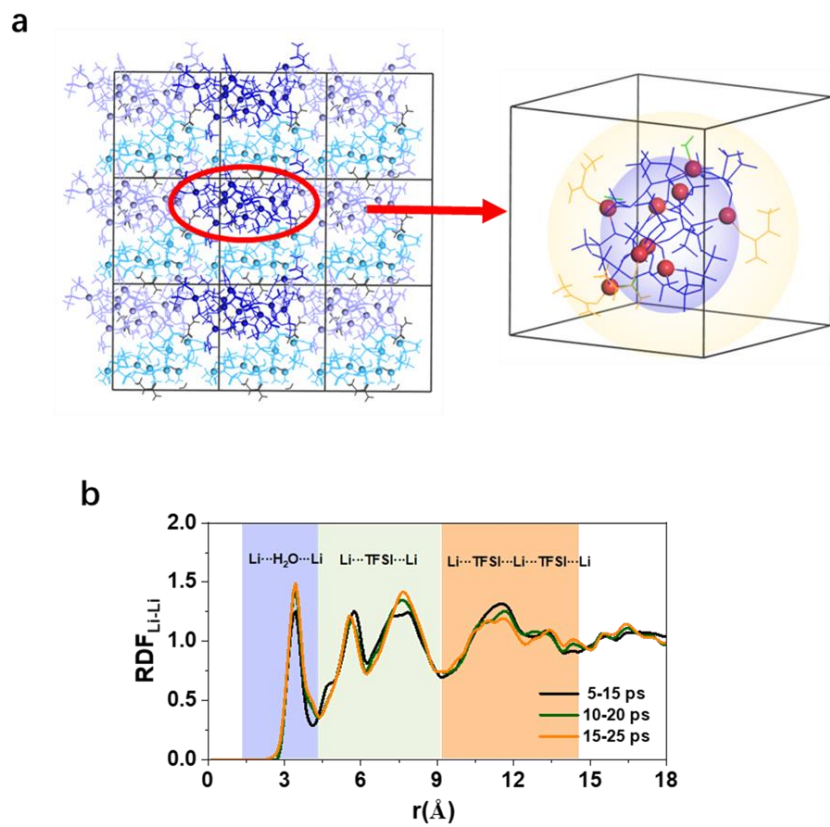


**Figure S40. The structural convergence of AIMD of Li-H<sub>2</sub>O-MU<sub>0.27</sub> in 25 ps. (a) The final configuration and its core-shell structure at 25 ps MD simulation. (b) The convergence of RDFs.**

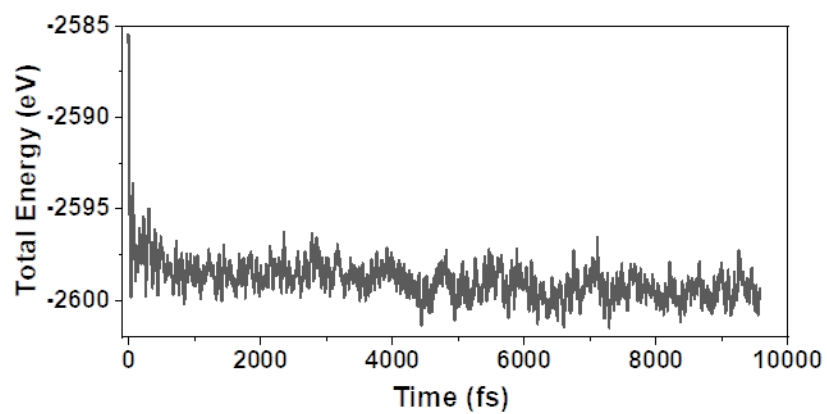


**Figure S41.** Total energy vs. time plot for a 10 ps AIMD starting with an initial configuration from 698 K AIMD.

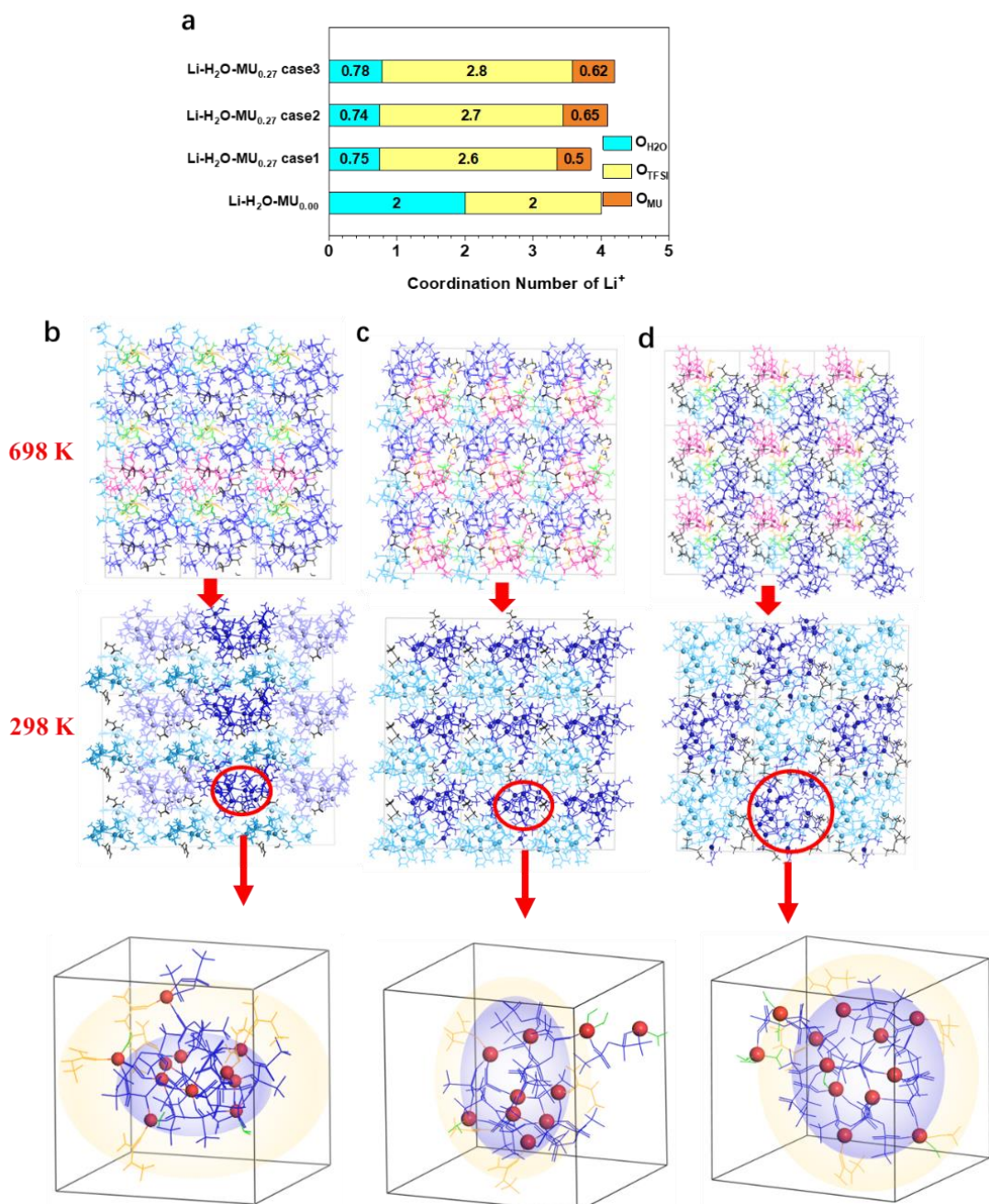
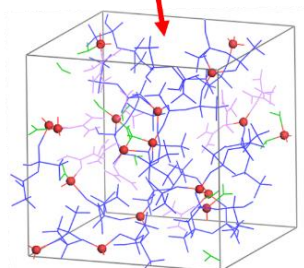
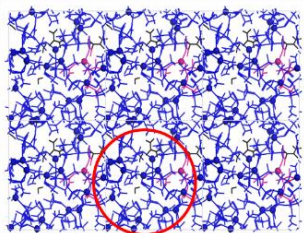
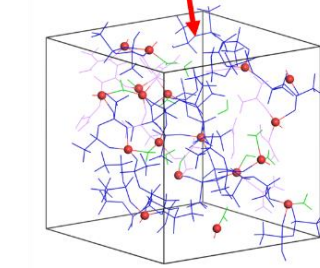
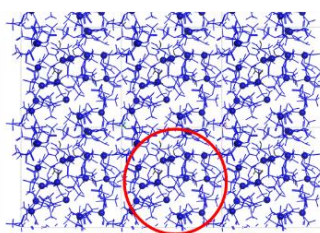


**Figure S42. Structural convergence of AIMD of Li-H<sub>2</sub>O-MU<sub>0.27</sub> at 298 K using different initial configurations.** (a) Coordination numbers of Li<sup>+</sup> obtained from the last 5 ps-trajectory of three different runs. (b), (c), and (d) showed three different initial configurations sampled from AIMD at 698 K (5 ps) all converged to similar configurations at 298 K (10 ps) with core-shell-like structures in the three runs.

Li-H<sub>2</sub>O-Urea<sub>0.27</sub> Case 1



Li-H<sub>2</sub>O-Urea<sub>0.27</sub> Case 2



Li-H<sub>2</sub>O-Urea<sub>0.27</sub> Case 3

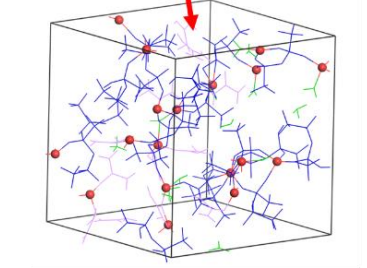
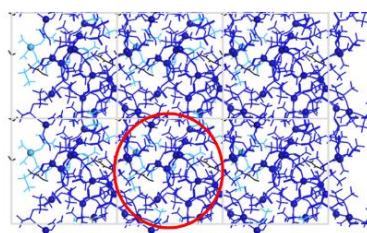


**Figure S43. Final configurations of Li-H<sub>2</sub>O-U<sub>0.27</sub> in the three AIMD simulations from different configurations.**

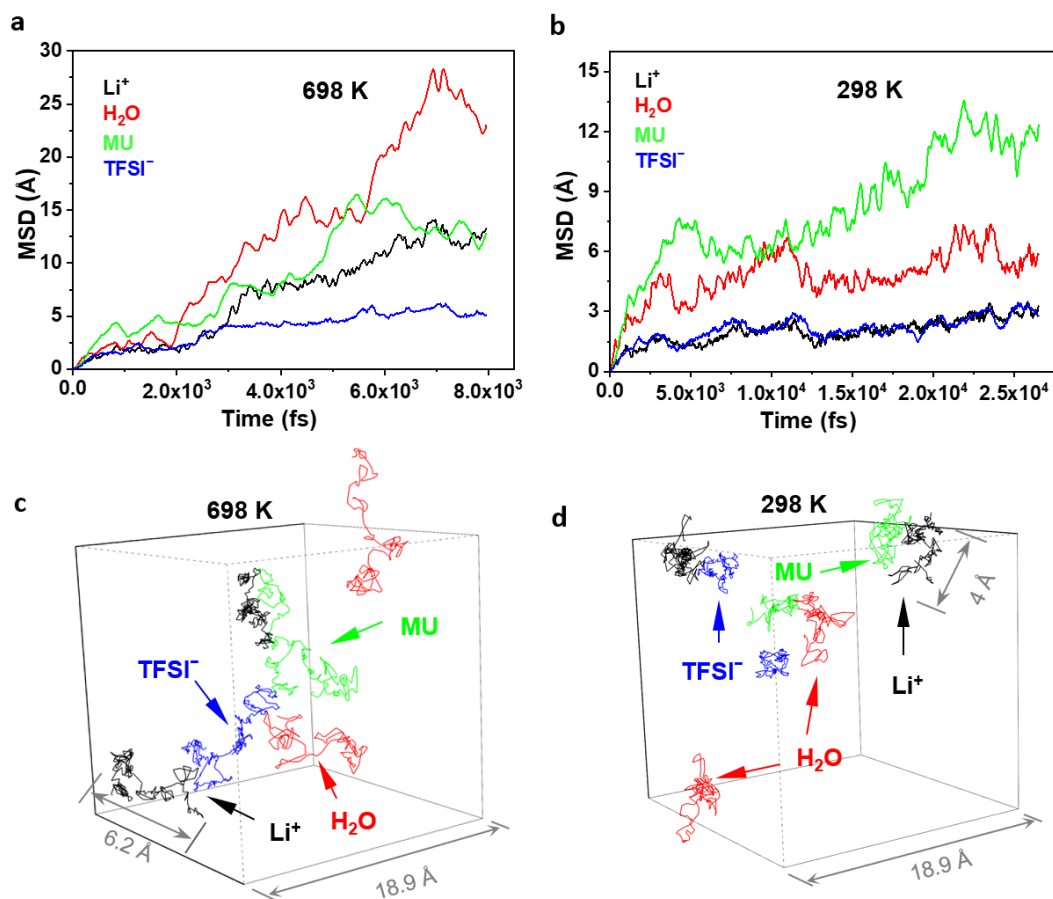


**Figure S44. Mass center displacements during AIMD simulations. (a, b)** Mean square displacement (MSD) of Li<sup>+</sup>, H<sub>2</sub>O, MU and TFSI<sup>-</sup> during a first 8 ps simulation at 698 K (a) and subsequent 25 ps simulation at 298 K (b). **(c, d)** Three-dimensional diffusion trajectories of Li<sup>+</sup>, H<sub>2</sub>O, MU and TFSI<sup>-</sup> during a first 8ps simulation at 698 K (c) and subsequent 25 ps simulation at 298 K (d). Clearly, there is a substantial displacement for Li<sup>+</sup>, H<sub>2</sub>O, MU and TFSI<sup>-</sup> during the AIMD simulation at 698 K. At 298 K, the molecules of MU and H<sub>2</sub>O also travel considerable distances. Comparatively, the displacements of Li<sup>+</sup> and TFSI<sup>-</sup> are smaller, which is due to the formation of three-dimensional network of Li<sup>+</sup> and TFSI<sup>-</sup> after the simulation at 698 K.

## 2 Tables

**Table S1. Comparison of aqueous Li-ion battery parameters of this work with those reported in literatures.**

Refs	Electrolyte		Negative electrode		Positive electrode		Cell		
	Formula ( <i>in short</i> )	Amount	Materials // Collector	Loading (mg cm <sup>-2</sup> )	Materials // Collector	Loading (mg cm <sup>-2</sup> )	Type	P/N	E/C ( $\mu\text{L mAh}^{-1}$ )
Ref. [1] Science 2015	21m LiTFSI-H <sub>2</sub> O ( <i>Li-H<sub>2</sub>O-MU<sub>0.00</sub></i> )	-	MoS <sub>2</sub> // SUS gird	10	LiMn <sub>2</sub> O <sub>4</sub> // SUS gird	10-20	Coin	2.2	-
Ref. [2] Angew. Chem. Int. Ed. 2016	21m LiTFSI-7m LiOTf-H <sub>2</sub> O ( <i>Li(TFSI)<sub>0.75</sub></i> ( <i>OTf</i> ) <sub>0.25</sub> (H <sub>2</sub> O) <sub>2</sub> )	-	Carbon-coated TiO <sub>2</sub> // SUS gird	3-4	LiMn <sub>2</sub> O <sub>4</sub> // SUS gird	6-8	Coin	1.6	-
Ref. [3] Nat. Energy 2016	LiTFSI-LiBETI- H <sub>2</sub> O ( <i>Li(TFSI)<sub>0.7</sub></i> ( <i>BETI</i> ) <sub>0.3</sub> (H <sub>2</sub> O) <sub>2</sub> )	-	Li <sub>4</sub> Ti <sub>5</sub> O <sub>12</sub> // Al	1	LiNi <sub>0.5</sub> Mn <sub>1.5</sub> O <sub>4</sub> // Ti	3	Coin	2.5	-
Ref. [4] Joule 2017	21m LiTFSI-7m LiOTf-H <sub>2</sub> O/PVA	-	HFE-PEO-gel- coated graphite // Cu	-	LiVPO <sub>4</sub> F // Al	-	Swagel ok	-	-
Ref. [5] Energy Environ. Sci. 2018	32 m KOAc-8 m LiOAc-H <sub>2</sub> O	-	Carbon-coated TiO <sub>2</sub> // Ti	3	LiMn <sub>2</sub> O <sub>4</sub> // Ti	4.5	Swagel ok	-	-
Ref. [6] Joule 2018	13.4m LiTFSI- H <sub>2</sub> O/DMC ( <i>Li-H<sub>2</sub>O-DMC<sub>0.16</sub></i> )	-	Li <sub>4</sub> Ti <sub>5</sub> O <sub>12</sub> // Al	4	LiNi <sub>0.5</sub> Mn <sub>1.5</sub> O <sub>4</sub> // Ti	8	Coin	1.6	-
Ref. [7] Electro. Commun. 2019	Li(PTFSI) <sub>0.6</sub> (TFSI) <sub>0.4</sub> (H <sub>2</sub> O) <sub>1.15</sub>	-	Li <sub>4</sub> Ti <sub>5</sub> O <sub>12</sub> // Al	-	LiCoO <sub>2</sub> // Ti	2	Coin	<1	-
Ref. [8] Nature 2019	21m LiTFSI-7m LiOTf-H <sub>2</sub> O/PVA	33-262 mg	HFE-PEO-gel- coated graphite // SUS grid	-	(LiBr) <sub>0.5</sub> (LiCl) <sub>0.5</sub> -graphite // Ti gird	38	Coin	1.38	-
Ref. [9] Energy Environ. Sci. 2020	8.9m LiTFSI- 3.1mLiOTf- H <sub>2</sub> O/Py <sub>13</sub> TFSI	~42 $\mu\text{m}$	PEO-LiTFSI- KOH-coated Li <sub>4</sub> Ti <sub>5</sub> O <sub>12</sub> // Al	2.8	LiMn <sub>2</sub> O <sub>4</sub> // Ti	4.6	Pouch	1.14	-
Ref. [10] Adv. Energy Mater. 2020	15.5m LiTFSI- H <sub>2</sub> O/AN ( <i>Li-H<sub>2</sub>O-AN<sub>0.34</sub></i> )	40 $\mu\text{L}$	Li <sub>4</sub> Ti <sub>5</sub> O <sub>12</sub> // Al	2	LiMn <sub>2</sub> O <sub>4</sub> // Ti	5	Coin	2	114
Ref. [11] Adv. Mater. 2020	15m LiTFSI- H <sub>2</sub> O/TEGDME	-	Li <sub>4</sub> Ti <sub>5</sub> O <sub>12</sub> // Al	1-2	LiMn <sub>2</sub> O <sub>4</sub> // Ti	2-3	Coin	1.5	-
Ref. [12] Adv. Mater. 2020	1 M CH <sub>3</sub> COOLi- H <sub>2</sub> O/maltose ( <i>Li-H<sub>2</sub>O-Sugar</i> )	-	Active carbon // Carbon paper	1-3	LiMn <sub>2</sub> O <sub>4</sub> // Carbon paper	1-3	Coin	-	-
Ref. [13] Nat. Mater. 2020	2 m LiTFSI- H <sub>2</sub> O/PEG ( <i>Li-H<sub>2</sub>O-PEG<sub>0.30</sub></i> )	-	LATP-coated Li <sub>4</sub> Ti <sub>5</sub> O <sub>12</sub> // Al	3.1	LiMn <sub>2</sub> O <sub>4</sub> // Al	3.8	Coin	1	-
<b>This work</b>	LiTFSI-H <sub>2</sub> O/MU ( <i>Li-H<sub>2</sub>O-MU<sub>0.27</sub></i> )	30 $\mu\text{L}$	NbO <sub>2</sub> // Al	4-5	LiMn <sub>2</sub> O <sub>4</sub> // Al	7-10	Coin	0.9-1	~30

**Note:** The mark “-” means the corresponding information was not provided in the literatures.

**Table S2. The density, molar concentration, mole and mass fractions of ingredients of the Li-H<sub>2</sub>O-MU<sub>x</sub> electrolytes**

Samples	Electrolyte	Molarity (mol L <sup>-1</sup> )	Density (g cm <sup>-3</sup> )	X <sub>LITFSI</sub> : Y <sub>H<sub>2</sub>O</sub> : Z <sub>MU</sub> (mole fraction)	X <sub>LITFSI</sub> ·Y <sub>H<sub>2</sub>O</sub> ·Z <sub>MU</sub> (mass fraction)
1	Li-H <sub>2</sub> O-MU <sub>0.00</sub>	5.16	1.7242	0.28: 0.72: 0.00	0.86:0.14:0.00
2	Li-H <sub>2</sub> O-MU <sub>0.09</sub>	5.13	1.7152	0.35: 0.56: 0.09	0.86:0.08:0.06
3	Li-H <sub>2</sub> O-MU <sub>0.16</sub>	4.99	1.7038	0.38: 0.46: 0.16	0.84:0.06:0.10
4	Li-H <sub>2</sub> O-MU <sub>0.21</sub>	4.82	1.6688	0.39: 0.40: 0.21	0.83:0.05:0.12
5	Li-H <sub>2</sub> O-MU <sub>0.27</sub>	4.70	1.6464	0.41: 0.32: 0.27	0.82:0.04:0.14
6	Li-H <sub>2</sub> O-MU <sub>0.33</sub>	4.54	1.6289	0.40: 0.27: 0.33	0.80:0.03:0.17
7	Li-H <sub>2</sub> O-MU <sub>0.39</sub>	4.32	1.6138	0.39: 0.22: 0.39	0.77:0.03:0.20
8	Li-H <sub>2</sub> O-MU <sub>0.46</sub>	4.14	1.6057	0.37: 0.17: 0.46	0.74:0.02:0.24
9	Li-H <sub>2</sub> O-MU <sub>0.55</sub>	3.94	1.5946	0.36: 0.09: 0.55	0.71:0.01:0.28
10	Li-H <sub>2</sub> O-MU <sub>0.65</sub>	3.67	1.5718	0.35: 0.00: 0.65	0.67:0.00:0.33
11	Li-H <sub>2</sub> O-MU <sub>0.73</sub>	1.41	1.3055	0.09: 0.18: 0.73	0.31:0.04:0.65

**Table S3. The mole ratios and mass percentages of ingredients of aqueous electrolytes hybridized with various flammable organic materials.**

Sample name	Composition	Salt :H <sub>2</sub> O :Organic	H <sub>2</sub> O wt%	Organic wt%
Li-H <sub>2</sub> O-DMC <sub>0.16</sub>	LiTFSI:H <sub>2</sub> O:DMC	0.36: 0.48: 0.16	6.8	11.4
Li-H <sub>2</sub> O-AN <sub>0.34</sub>	LiTFSI:H <sub>2</sub> O:AN	0.32: 0.34: 0.34	5.5	12.4
Li-H <sub>2</sub> O-PEG <sub>0.30</sub>	LiTFSI:H <sub>2</sub> O:PEG	0.26: 0.44: 0.30	3.8	59.7
Li-H <sub>2</sub> O-Sugar <sub>0.08</sub>	LiAc:H <sub>2</sub> O:Sugar	0.02: 0.90: 0.08	32.4	60.0
Li-H <sub>2</sub> O-U <sub>0.34</sub>	LiTFSI:H <sub>2</sub> O:U	0.26: 0.34: 0.40	7.0	20.0



### 3 References

1. Suo, L.M., Borodin, O., Gao, T., Olguin, M., Ho, J., Fan, X.L., Luo, C., Wang, C.S., and Xu, K. (2015). "Water-in-salt" electrolyte enables high-voltage aqueous lithium-ion chemistries. *Science* **350**, 938-943.
2. Suo, L., Borodin, O., Sun, W., Fan, X., Yang, C., Wang, F., Gao, T., Ma, Z., Schroeder, M., von Cresce, A., et al. (2016). Advanced High-Voltage Aqueous Lithium-Ion Battery Enabled by "Water-in-Bisalt" Electrolyte. *Angew. Chem. Int. Ed.* **55**, 7136-7141.
3. Yamada, Y., Usui, K., Sodeyama, K., Ko, S., Tateyama, Y., and Yamada, A. (2016). Hydrate-melt electrolytes for high-energy-density aqueous batteries. *Nat. Energy* **1**, 16129.
4. Lukatskaya, M.R., Feldblyum, J.I., Mackanic, D.G., Lissel, F., Michels, D.L., Cui, Y., and Bao, Z. (2018). Concentrated mixed cation acetate "water-in-salt" solutions as green and low-cost high voltage electrolytes for aqueous batteries. *Energy Environ. Sci.* **11**, 2876-2883.
5. Ko, S., Yamada, Y., Miyazaki, K., Shimada, T., Watanabe, E., Tateyama, Y., Kamiya, T., Honda, T., Akikusa, J., and Yamada, A. (2019). Lithium-salt monohydrate melt: A stable electrolyte for aqueous lithium-ion batteries. *Electrochem. Commun.* **104**, 1904961.
6. Yang, C.Y., Chen, J., Qing, T.T., Fan, X.L., Sun, W., von Cresce, A., Ding, M.S., Borodin, O., Vatamanu, J., Schroeder, M.A., et al. (2017). 4.0 V Aqueous Li-Ion Batteries. *Joule* **1**, 122-132.
7. Yang, C., Chen, J., Ji, X., Pollard, T.P., Lu, X., Sun, C.J., Hou, S., Liu, Q., Liu, C., Qing, T., et al. (2019). Aqueous Li-ion battery enabled by halogen conversion-intercalation chemistry in graphite. *Nature* **569**, 245-250.
8. Zhang, J., Cui, C., Wang, P.-F., Li, Q., Chen, L., Han, F., Jin, T., Liu, S., Choudhary, H., Raghavan, S.R., et al. (2020). "Water-in-salt" polymer electrolyte for Li-ion batteries. *Energy Environ. Sci.* **13**, 2878-2887.
9. Wang, F., Borodin, O., Ding, M.S., Gobet, M., Vatamanu, J., Fan, X., Gao, T., Eidson, N., Liang, Y., Sun, W., et al. (2018). Hybrid Aqueous/Non-aqueous Electrolyte for Safe and High-Energy Li-Ion Batteries. *Joule* **2**, 927-937.
10. Chen, J.W., Vatamanu, J., Xing, L.D., Borodin, O., Chen, H.Y., Guan, X.C., Liu, X., Xu, K., and Li, W.S. (2020). Improving Electrochemical Stability and Low-Temperature Performance with Water/Acetonitrile Hybrid Electrolytes. *Adv. Energy Mater.* **10**, 1902654.
11. Shang, Y., Chen, N., Li, Y., Chen, S., Lai, J., Huang, Y., Qu, W., Wu, F., and Chen, R. (2020). An "Ether-In-Water" Electrolyte Boosts Stable Interfacial Chemistry for Aqueous Lithium-Ion Batteries. *Adv. Mater.* **32**, 2004017.
12. Bi, H.B., Wang, X.S., Liu, H.L., He, Y.L., Wang, W.J., Deng, W.J., Ma, X.L., Wang, Y.S., Rao, W., Chai, Y.Q., et al. (2020). A Universal Approach to Aqueous Energy Storage via Ultralow-Cost Electrolyte with Super-Concentrated Sugar as Hydrogen-Bond-Regulated Solute. *Adv. Mater.* **32**, 2000074.
13. Xie, J., Liang, Z., and Lu, Y.C. (2020). Molecular crowding electrolytes for high-voltage aqueous batteries. *Nat. Mater.* **19**, 1006-1011.